A 1D model for the Pulmonary and Coronary Circulation Accounting for Time-Varying External Pressure

by

Jay Aodh Mackenzie

A thesis submitted to the

College of Science and Engineering

at the University of Glasgow

for the degree of

Doctor of Philosophy

August 2021

Abstract

Pulmonary and coronary hæmodynamics are strongly influenced by the rhythmic motion of heart and lungs – studies show that coronary arterial flow drops to near 0 during systole and pulmonary flow increases during normal respiration. Several previous studies have attempted to capture this motion, and the effect it has on arterial and venous blood flow. However, the method of inclusion of "external pressure" is often *ad hoc* or requires tuning parameters that lack a physical meaning. For the first time, we present a 1D model for blood flow in the pulmonary and the coronary arteries and veins that is implemented using only physiological measured data. To achieve this, we develop an existing 1D model for viscous blood flow in thin, elastic walled arteries and veins to include an explicit dependence on a prescribed time-varying external pressure. The arterial and venous sides are matched using a pair of grand admittance matrices of a structured tree that were derived using the 1D theory; one of the matrices encodes the effect of fluid pressure on venous flow and the other the impact of external pressure. We extend the boundary condition used to join arterial or venous segments to directly model vessel stenoses or trifurcations.

We use the model to simulate pulmonary blood flow during quiet respiration, pneumothorax, and mechanical ventilation of adults. We find good agreement between our model results and reports from the literature.

We develop a framework for building realistic coronary arterial and venous networks from a number of sources. We build several networks that have different branching patterns and levels of detail, and quantify the impact on arterial flow and pressure these have. The volume of the large vessel network in the reference configuration is an important determinant of coronary flow. Further, we compare networks with a simplified venous structure against a branching venous network in which the right and left coronary arteries ultimately drain into the right atrium via the coronary sinus, finding that the morphometry of the venous network is an important determinant of arterial flow. We show that the model can be used to model vascular rarefaction and microvascular stiffening, showing good agreement with reports from the literature.

Acknowledgements

First and foremost, I would like to thank my supervisors Prof. Nick Hill and Prof. Xiaoyu Luo. They have been unwaveringly supportive and encouraging over the years of this project, dedicating countless hours to my development as a mathematician and person.

I am also endebted to Megan Chambers, Mitchel Colebank, Mette Olufsen, and Umar Qureshi for their technical assistance, helpful suggestions, and encouragement.

Furdly, I would like to thank Groliff, for whom r-furcations are named. Additionally my parents, Alan and Alex, for their unconditional love and support. They have my unreserved and enduring thanks.

Finally, to my friends and many office mates over the years, I am grateful and glad to have known you. Thank you.

Frequently Used Symbols

$p(x,t)$: Fluid pressure, the pressure along the centreline of a cylindrical vessel

$\text{þ}(t)$: External pressure applied to a vessel

$\varphi(x,t)$: Transmural pressure the pressure across the wall between p and þ

$q(x,t)$: Volumetric flow rate

$A(x,t)$: Vessel lumen area in the current configuration

Frequently Used Abbreviations

LCA: left coronary artery, a large artery arising from the aorta,

LAD: left anterior descending, a large artery that supplies the anterior left ventricle,

LCx: left circumflex, a large artery that supplies the posterior left ventricle,

PLVA: posterolateral left ventricular artery, a large artery arising from the LCx that supplies the posterior left ventricle,

RCA: right coronary artery, a large artery arising from the aorta,

PIVA: posterior interventricular artery, a large artery that supplies the interventricular septum,

AVNA: atrioventricular nodal artery, supplies the atrioventricular node on the interatrial septum,

CS: coronary sinus, the largest vein; it drains into the right atrium,

GCV: great cardiac vein, a large vein that drains the LAD; the main tributary of the CS,

OVLA: oblique vein of the left atrium, a large vein that runs obliquely across the surface of the left atrium,

MPA: main pulmonary artery, the main pulmonary artery that gives rise to the right and left pulmonary arteries.

Contents

List of Figures

List of Tables

Chapter 1

Introduction

1.1 A Brief Overview of the Cardiovascular System

The human cardiovascular system consists of the heart and a closed system of blood vessels (arteries, arterioles, capillaries, venules, and veins). The heart, a hollow, muscular pump, consisting of four chambers, drives the motion of blood throughout the body. Deoxygenated blood arrives in the right atrium from the body, from which it is pumped into the right ventricle and to the lungs via the pulmonary arteries to be oxygenated and have carbon dioxide removed and expelled. The oxygenated blood arrives back at the heart via the pulmonary veins, and is driven from the left atrium into the left ventricle to the rest of the body via the systemic arterial system. All tissues in the body must be continually supplied with oxygenated blood and have deoxygenated blood removed. The heart muscle and the lungs must also be supplied with blood – the lungs via the pulmonary circulation and the heart via the coronary arteries and cardiac veins.

The lungs are attached to the ribcage and diaphragm by the pleural membrane,

a double walled structure that surrounds the fluid filled pleural cavity [9]. During normal respiration, the ribcage moves upwards and outwards, and the diaphragm out and down, causing pleural cavity pressure to fall below atmospheric pressure [10, 11]. This pressure drop causes the lungs to expand and air is drawn into them via the airway. From the mouth or nose, air passes into the larynx, then trachea and left and right bronchi which supply each lung. The bronchi divide to become bronchioles, alveolar ducts, and alveoli. The alveolar ducts and alveoli are the main site of gas exchange with the blood contained within pulmonary capillaries. This phase of respiration is called inspiration, and is followed by expiration. During expiration, the diaphragm and ribs move back to their resting position causing the pleural cavity pressure to increase, the lungs to deflate, and the air to be expelled. Almost all of the pulmonary circulatory system is buried within the lung tissues, so the majority of the blood vessels are subject to changes in external pressure during respiration.

Similarly, most of the blood vessels that supply the heart are buried within the heart wall [12]. During systole, when the heart wall is contracting, blood pressure and flow in the pulmonary and systemic increase. However, there is a paradoxical coronary arterial flow drop during systole as the micro-vasculature is compressed and blood flow into the small vessels is impeded [13, 14]. During diastole, as the heart muscle relaxes and pressure within the wall drops, coronary blood flow increases as the compression of the vascular beds eases [15].

1.2 Mathematical Models of the Cardiovascular System

Mathematical models allow us to gain a deeper understanding of a rich array of complex systems, from economies to swimming micro organisms [16]. The cardiovascular system is no exception. It is an immensely complicated system that is also vital to life [17]. This vitality and complexity make cardiovascular modelling an enticing challenge that has been growing area of scientific interest over the past half century [18]. Cardiovascular modelling is of particular current interest, as cardiovascular disease is one of the leading causes of death worldwide [19, 20]. Mathematical models can be used to test hypotheses, predict previously uncertain outcomes, and conduct experiments that would be otherwise unfeasible [16, 21].

Fluid dynamic models have a long history, stretching at least as far back as Archimedes' investigations of buoyancy some 2300 years ago [22]. Significant advancements have been made in the intervening years, by the likes of Castelli (fluid motion in rivers), Euler (inviscid flows), Newton (viscosity and friction), Pascal (hydostatics), Bernoulli (hydrodynamics), and Navier and Stokes (Navier–Stokes equations). Hæmodynamic modelling was pioneered in the 20th century by McDonald [23], Womersley [24], and Pedley [25]. McDonald's work was chiefly concerned with pulsatile blood flow and associated pulsatile pressure changes. McDonald and Womersley collaborated on the mathematical modelling of pulsatile flows. Womersley applied mathematical and computational techniques to the analysis of arterial blood flow, and described a dimensionless parameter that characterises the nature of unsteady flows [26, 27]. Pedley pioneered research on fluid-structure interactions in elastic walled tubes and the pressure drop within the lung [25]. Formaggia, Quar-

teroni & Veneziani [28] give a more comprehensive overview of the current state of the art.

Typically a cardiovascular modelling study focuses on a domain of interest, such as the systemic circulation [29–32], the pulmonary circulation [2,33], or the coronary circulation [34], modelling the regions outwith this domain via a lumped parameter approach. Domains of particular interest are modelled in 3D, with 1D and 0D models providing boundary conditions. Such models have been used to investigate aortic root flow [35–37], heart valves [38,39], and flow within the ventricles [40]. At present, 3D modelling of the entire cardiovascular system is not possible, due to the complexity and scale of the system [34]. However, it has long been known that cardiovascular flows can be considered quasi-1D, as the wavelengths of pressure pulses is much longer than the diameter of blood vessels [41,42].

The model presented in this thesis captures arterial and venous flow and pressure in vessels that are subject to some external pressure. It is designed to be implemented using only data that is either directly measurable or inferable from physiological measurements, so can be used to model any arterial and venous system given sufficient data. There are many predecessors to this model. Below, I describe some of the most notable.

Olufsen [30,43,44] developed an arterial 1D flow model that uses the impedance of a structured tree (a self similar binary tree that can be thought of as an average description of a vascular bed) as the outlet boundary condition. Her model shows a better pressure/flow phase relationship than models with a constant peripheral impedance. One of the other key advantages of the structured tree is that the impedance is calculated once at the beginning of a simulation, so several arterial outlets can be characterised by different impedances from the same scheme.

Mynard & Nithiarasu [34] present a 1D flow model for the coronary and systemic circulations that includes the compression of the coronary vasculature by the left ventricle, and an aortic valve that opens and closes based on local hæmodynamics. The external pressure applied to the coronary vasculature is encoded in their constitutive relation for vessel lumen area, as is done later in this thesis and by Müller [31]. They use a locally conservative Galerkin method to solve the 1D system of model equations. This Galerkin method is second-order accurate in time, and is the finite-element equivalent of the Lax–Wendroff scheme used by Qureshi [3], Vaughan [29], Olufsen [44] and ourselves.

Mynard & Nithiarasu also incorporate one-to-one and one-to-three vessel branching (mono- and trifurcations). Monofurcations enable the modelling of blood flow through vessels with discontinuities in, e.g., lumen area or vessel material properties. The junction matching conditions presented later in this thesis were developed independently from those of Mynard & Nithiarasu [34]. The left and right coronary arteries are modelled explicitly, with both bifurcating into two tapering vessels with the downstream boundary condition provided by a 0D lumped model of the remaining arterial vessels, vascular beds, and cardiac veins. The left ventricle pressure is time-varying and are scaled so that right coronary arterial vessels undergo less compression than left coronary arterial vessels, and vessels buried deeper within the myocardium are subject to larger external pressures than those near the surface.

Vaughan [29, 45] extended the work of Olufsen to develop a new model for the pulmonary circulation including arterial and venous flows and pressures, and to derive a new boundary condition used to connect the arterial and venous sides. This new boundary condition uses the grand admittance matrix related arterial to venous flow using a Fourier decomposition of the 1D flow. It is upon this arterial/venous

boundary condition that the one presented in this thesis is based. This boundary condition allowed him to capture venous pulse wave dynamics.

Clipp & Steele [33, 46, 47] modelled 1D pulmonary arterial blood flow using a flow-based inlet boundary condition, and a dynamic outlet boundary condition intended to simulate the changes in vascular bed resistance that arise due to respiration. The boundary condition they use is impedance based, and they achieve the respiration variation by modifying the steady component. This boundary condition is based on an electrical analogue, so the parameters have no direct physical meaning, and must be tuned to achieve good agreement with measured data. Using this model, they showed that pulmonary arterial flow is insensitive to respiration when using a pulsatile inflow to drive the simulation and that blood pressure does vary with respiration. They validated these results against experimental data, using isolated lamb lungs in airtight boxes in which negative pressures were applied to simulate respiration; constant blood flow in these experiments was provided using a pump. In these experiments they found that the constant blood flow does not vary with respiration, but that blood pressure does.

Qureshi [3] developed and extended Vaughan's [29] 1D flow model to improve its ability to predict pulmonary arterial and venous blood flow and pressure dynamics. He achieved this by improving the venous morphometry, physiological parameters, and boundary conditions, and by extending the model to predict pressure drop across vascular beds. He showed that this model can be used to simulated pulmonary blood flow under healthy conditions, and can be used to accurate pulmonary pressures and flow in, for example, pulmonary arterial hypertension by altering the model parameters.

Müller [31] developed a 1D flow model for the long veins that transport blood to and from the human brain [31]. The derivation of the 1D model equations presented by Müller are very similar to the ones seen here, as is their method of inclusion of external pressure which varies in space and time. External pressure arises from surrounding tissues, and is included in the 1D flow model via the relationship between blood pressure and vessel lumen area known as a constitutive relation. Lumped parameter models are used for the vascular beds, the heart and pulmonary circulation. No external pressure is explicitly included in the 0D description of the vascular beds. Although the 1D models presented by Müller and me are similar, our applications and boundary conditions differ greatly.

Zheng [48, 49] simulated arterial coronary flow in a patient-specific vasculature using a measured pressure profile to provide the inlet boundary condition and the vascular beds and coronary venous circulation were represented using a three-element Windkessel model, a specific choice of lumped parameter model. They approximated vascular bed compression by the myocardium by including an *ad hoc* pressure-drop term in the large vessels. The parameters of the three element Windkessel must be tuned to give a good fit to measured data.

All of the models discussed above are 1D flow models for which the authors have made rational assumptions and approximations in order to linearise the Navier–Stokes equations (as we will see shortly). These are linearised, not linear, models that can and do exhibit non-linear behaviours.

1.2.1 Outlet Boundary Conditions and Small Vessel Models

For the work in this thesis we adopt a structured tree approach to modelling the behaviour of blood in small vessels. A structured tree is self-similar binary tree, composed of small vessel segments that are joined in series and parallel with each other. A structured tree can be thought of as an average description of a vascular bed. One can use a structured tree as either an outflow condition for an arterial model, or as a boundary matching condition in a two-sided model (such as is presented here).

Structured trees are not the only possible choice of boundary condition. Another common choice is the three-element windkessel. This is a lumped parameter (0D) model that provides an outlet boundary condition to a 1D hæmodynamic model. Unlike the structured tree, it is not physiologically motivated so the parameters used are not physiologically meaningful, hence they must be tuned so that simulation results fit to measured data. One of the major drawbacks of a using a windkessel boundary condition is that it is inherently one-sided, that is they cannot be as a boundary matching condition between an arterial and venous tree, so are unsuitable if one wishes to study pressure wave propagation into a venous tree.

1.2.2 Arterial Wall Models

In this thesis, blood vessels are assumed to be axisymmetric tubes with thin, elastic walls. However, it is worth noting that there are more complex models for vessel walls such as that presented by Holzapfel, Gasser & Ogden [50], who developed a new constitutive law to describe the passive mechanical response of a thick-walled artery. We call this the HGO model. Artery walls are comprised of three distinct layers, the intima, media, and adventitia. The HGO model explicitly includes the mechanical contributions of the media and adventitia including the direction of collagen within

the layers.

There are two main kinds of arteries identified in the medical literature – elastic and muscular [12]. Elastic arteries are typically of larger diameter and are located close to the heart. They feature higher proportions of elastic components in the middle layer of the arterial wall than muscular arteries [51]. The aorta, and carotid and illiac arteries, for example, are considered to be elastic. Muscular arteries tend to be of smaller diameter and further away from the heart – the middle wall layer contains a higher proportion of smooth muscle cells. Such a distinction may motivate the use of different wall models in 3D arterial flow models, such as at the aortic root [52]. Arteries exist on a continuum from elastic-to-muscular based on the proportion of elastic and muscular components in the arterial wall [51].

1.3 Organisation of This Thesis

We present a mathematical and computational model for 1D blood flow and blood pressure in a two-sided arterial-venous tree. The sides of the tree are joined using a boundary condition derived using a structured tree description of a vascular bed. We are able to specify the lengths and radii of all large arteries and veins, as well as the flow or pressure at the inlet of the large arterial tree, the pressure at the outlet of the venous tree, and external pressures that may be applied to the tree by the movement of surrounding tissues. We apply this model to the coronary and pulmonary circulatory systems in health and disease.

This thesis is organised into six chapters. This, the first chapter, gives an overview of the cardiovascular system, motivates modelling attempts, and discusses some of the history of cardiovascular modelling. In Chapter 2, we derive the model equations for flow in large and small blood vessels. In Chapter 3, we adapt a two-step Lax–

Wendroff scheme for flow in a vessel, as well as establishing any boundary conditions needed in the model. These boundary conditions include a novel scheme that allows us to include branching from one-to-many vessels. Chapter 3 contains simulations with a toy model, and shows that the model behaves in self-consistent and intuitively reasonable ways. In this chapter we also model pulmonary flows during respiration, capturing the flow change during inspiration reported in the literature. The first half of Chapter 5 deals with coronary arterial networks, and how to implement a patient specific network in the model. We then simulate blood flow in a variety of networks to quantify the impact that network modelling choices have on simulated blood flow and and pressure, as well as in physiologically realistic scenarios of health, vessel stenosis, and microvascular stiffening. Chapter 6 summarises our findings, and suggests directions for future research.

1.4 Contributions of This Thesis

The main contributions of this thesis is the development of a 1D mathematical model for physiological flows in large arteries and veins that are subject to some periodic external pressure that need not have the same period as the pressure pulse. This model is implemented using only parameters and data that are directly measurable or inferable from measured data. We also develop novel boundary matching conditions that allow for the inclusion of one-to-many branching. The model presented here can be easily adapted to patient specific data, including many branches of the coronary or pulmonary arterial and venous network. Our simulation results show good qualitative agreement with reports from the medical literature, with other modelling studies, and are self-consistent.

Chapter 2

Hæmodynamics

In this chapter, we formulate a 1D mathematical model for blood flow and pressure in a two-sided network of large arteries and veins that have a time dependent external pressure imposed upon them. In vascular networks, large arteries are joined to large veins via many generations of small arteries, arterioles, capillaries, venules, and veins; this collection of small blood vessels is known as a vascular bed.

The computational domain of this model is comprised of large and small vessels. Large vessels are those in which we model blood flow explicitly on a per-vessel basis, and small vessels are modelled via a structured tree description. Large vessels comprise the first few generations of the arterial and venous sides, and small vessels comprise the remaining vessels. In large vessels, we solve the 1D governing equations numerically for all temporal points in a given interval, and for all spatial points in the computational domain.

Almost all of the pulmonary or coronary vasculature lies within the organs that they supply with blood. As the heart and lungs both move during the normal course of their function, the embedded blood vessels are subject to some spatio-temporally

varying external pressure. The model presented in this chapter encodes external pressure as a fundamental assumption.

The model presented here was developed independently of others presented in the literature. We explicitly include external pressure that is applied to all vessels in the small and large arterial trees using physiologically motivated modelling. Other models that include external pressure, for example, those of Clipp & Steele [33,46,47], Müller [31], Duanmu [48, 49]. These are discussed in more detail in Chapter 1. For now, it suffices to highlight that our model differs significantly from these. Clipp & Steele and Duanmu *et al.* include external pressure by altering a pressure component in the boundary condition in order to fit their simulation results to data; Müller [31] and Mynard & Nithiarasu [34] include an explicit external pressure term in their 1D equations for flow, but do not include such a term in their 0D boundary conditions. The main contributions of this chapter is the extension of 1D model equations to include time-varying external pressure and the derivation of the novel admittance matrix that encodes external pressure applied to the vascular beds.

2.1 Blood

Viscosity is a measure of a fluid's resistance to deformation at a given rate. Newtonian fluids are those with constant viscosity. Non-newtonian fluids are not Newtonian: their viscosities change at a non-constant rate with increasing deformation. Dynamic viscosity, μ, is the constant of proportionality that relates a force per unit area applied to a fluid to its local shear velocity. Kinematic viscosity, ν, relates dynamic viscosity and fluid density ρ, $\nu = \mu/\rho$. The bulk or volume viscosity of a suspension of particles in a fluid, e.g. cells in blood, is the dynamic viscosity of the whole suspension at length scales much greater than those of the fluid particles.

Blood is comprised of deformable particles (red blood cells, platelets, etc.) suspended in a viscous fluid (plasma). The largest blood cells (leucocytes) have an unstressed diameter of approximately 22 µm [25]. Blood is incompressible [53], as blood plasma and all blood cells are incompressible.

The contents of all blood cells are viscous and non-Newtonian, hence whole blood must be non-Newtonian, regardless of scale. At sufficiently large scales, blood can be considered to be Newtonian, however this doesn't hold for the radius scale of small vessels. Hence, we consider these scales separately.

Whole blood viscosity is impacted by many factors including hæmatocrit level, blood temperature, plasma viscosity, erythrocyte deformability and aggregation, and shear-rate [54–56]. Under normal physiological conditions, none of these — bar shear-rate — vary on the time-scales of a breath or heartbeat, so we hold these factors constant. According to Litwin & Chapman [54], shear-rate varies with vessel lumen size and shape, amongst other quantities.

Shear-rate is the rate of blood flow velocity of adjacent streaming layers

$$\gamma = \frac{4q}{\pi r^3},$$

in a cylindrical pipe of radius r and volumetric flow rate q for Poiseuille flows. Maximum shear-rate is found at the wall of a vessel [57]. As shear-rate varies with lumen radius and shape, blood viscosity must also vary with distance from a vessel's centreline. Including such variations is outwith the scope of this study. Under normal physiological conditions, the shear-rate at the vessel wall increases from about $10\,\mathrm{s}^{-1}$ in the largest veins to about $2000\,\mathrm{s}^{-1}$ in the smallest arteries.

Lee et al. [1] present a graph of the relationship between shear-rate and bulk viscosity; this is reproduced in Fig. 2.1[1]. The data shown are averaged from the

[1]Using WebPlotDigitizer, V.4.1, A. Rohatgi

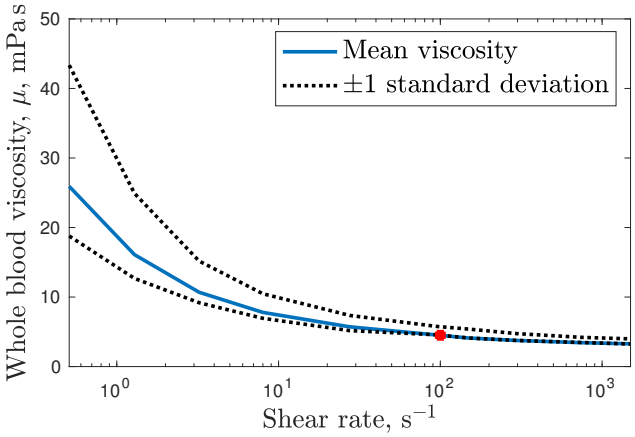

Figure 2.1: Reproduction of Fig. 2 from Lee *et al.* [1] illustrating the relationship between whole blood viscosity and increasing shear rate in healthy patients of body temperature 37.5°C and hæmatocrit corrected to 0.4. The red dot shows the chosen value for dynamic viscosity μ.

21 healthy control subjects with hæmatocrit normalised to 0.4. Hæmatocrit is the proportion of blood cells by volume in the total blood volume [58]. As can be seen from the figure, bulk viscosity decreases sharply as shear-rate increases from $1\,\mathrm{s}^{-1}$ to $100\,\mathrm{s}^{-1}$, and considerably more slowly from $100\,\mathrm{s}^{-1}$ onward. The physiologically realistic range of shear-rate in large vessels is above $10\,\mathrm{s}^{-1}$. The drop in bulk viscosity between $0.1\,\mathrm{s}^{-1}$and $10\,\mathrm{s}^{-1}$ is $20\,\mathrm{mPa\,s}$, where as the drop between $10\,\mathrm{s}^{-1}$ and $1000\,\mathrm{s}^{-1}$ is $4\,\mathrm{mPa\,s}$; the mean gradient of the curve between these points is -2.4 and -0.003, respectively. Since the change in bulk viscosity is so small across the expected physiological range $10\,\mathrm{s}^{-1}$ to $2000\,\mathrm{s}^{-1}$, we choose to assume that bulk viscosity is constant under normal physiological conditions regardless of the large vessel in which blood is flowing. In order to set a value for bulk viscosity, following Lee *et al.* [1], we fix the hæmatocrit at 0.4 and blood temperature at 37.5°C, which are both within physiological norms. We must also choose a value of shear-rate that defines the

bulk viscosity; for consistency with other models [2, 30, 43, 59], we choose 100 s^{-1}. The dynamic bulk viscosity of the blood we describe here is $\mu = 4.503\,\text{mPa}\,\text{s}$ (to 4 significant figures (s.f.)), as per the data from Lee *et al.* [1].

We assume that all blood is homogeneous, but blood in large vessels (radius $>$ 0.5 mm) is Newtonian and blood in smaller vessels is non-Newtonian (radius between 0.5 mm and 0.05 mm), i.e. the dynamic viscosity is allowed to vary with shear-rate. As shear-rate varies with lumen radius, we take lumen radius as a proxy for shear-rate. For model simplicity, we assume that the shear-rate (and hence viscosity) within a small vessel is constant, but it need not have the same as the shear-rate as its parent or daughter vessels. Intra-vessel variations in viscosity in very small vessels (the smallest arterioles and venules, and capillaries) are outwith the scope of this study as the 1D model that we will shortly derive lacks the necessary local details.

In large vessels, we assume that blood is homogenous and Newtonian. Fåhræus & Lindqvist [60] and Martini [61] observed that Poiseuille's law does not apply to blood flow in glass tubes below about 150 µm in radius — the apparent viscosity of blood shows a marked decrease as bore radius decreases from 150 µm to 5 µm. Pries *et al.* [62,63] used a network-based approach to study the rheological behaviour of blood flow in rat mesenterty micro-vessels; these results were compared with mathematical model predictions. According to Secomb & Preis [64], apparent blood viscosity decreases with decreasing radius down to 20 µm before beginning to increase precipitously. The apparent viscosity increases sharply with decreasing radius in the range 10 µm – 2.5 µm; this is the radius range of capillaries [5]. According to Secomb & Preis [64] "[a] substantial fraction of the flow resistance in microvascular networks resides in vessels with [radii] in this range", which is consistent with conclusions from other studies [65, 66]. All of the above radii are given in the reference configuration.

While arteries and veins feature strictly diverging or converging branches [4, 7], the same cannot be said of capillary beds [5]. Because of the divergence of arterial branches, and converging of venous branches, these can be represented using a structured tree. Capillaries within a bed converge and diverge without clear structure, so cannot be modelled via a structured tree. Because of this constraint, structured trees do not include any vessels with radius < 10 µm. The miniumum radius of vessels within the structured trees is controlled by setting r_{min}. The chosen values are discussed in Chapters 4 & 5. In general, decreasing r_{min} leads to an increase in computational time.

Pries *et al.* [62] presented a study to determine the dependence of effective viscosity on vessel diameter and hæmatocrit in living tissue. Effective viscosity is defined as the viscosity calculated from Poiseuille's equation for the observed pressure drop along the vessel, the average vessel diameter, and the vessel length. The study combines experimentally measured hæmatocrit and flow velocities, and mathematical models of blood flow. The deviations between measured and predicted hæmatocrit and velocity were used to refine the assumptions made in their simulations. The study yields a parametric description of effective *in vivo* viscosity as a function of vessel diameter and hæmatocrit:

$$\mu_v(r) = \left[1 + (\mu^*(r) - 1)\,\frac{(1-H)^{C(r)} - 1}{0.55^{C(r)} - 1}\left(\frac{r}{r - 0.55}\right)^2\right]\left(\frac{r}{r - 0.55}\right)^2$$

in which $\mu_v(r)$ is the *in vivo* viscosity, $H \in [0, 1]$ is hæmatocrit, r is vessel radius in µm,

$$C(r) = \left(0.8 + e^{-0.15r}\right)\left(\frac{1}{1 + 2 \cdot 5^{-11} \cdot r^{12}} - 1\right) + \frac{1}{1 + 2 \cdot 5^{-11} \cdot r^{12}},$$

and

$$\mu^*(r) = 6e^{-0.17r} - 2.44e^{-0.12r^{0.645}} + 3.2.$$

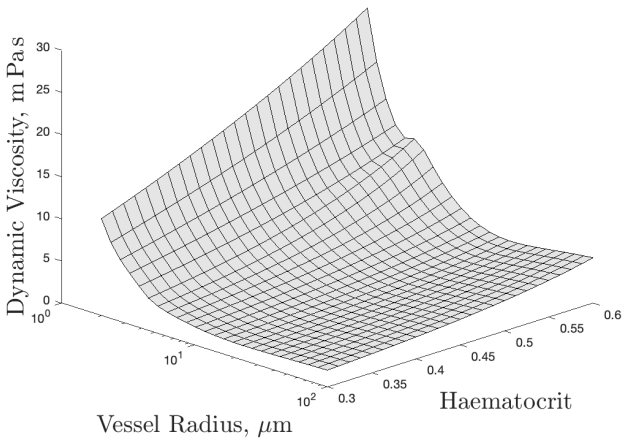

Figure 2.2: Surface of effective viscosity given independent variables hæmatocrit and vessel radius. The ranges of radius and hæmatocrit chosen given physiologically realistic values.

The diameter of all vessels in the network in which this viscosity law is applied are found during the computation, so it is straightforward to find C and μ^*. Fig. 2.2 shows a surface depicting the relationship between predicted effective viscosity, hæmatocrit, and vessel radius. The effective viscosity function $\mu_v(r)$ has a vertical asymptote at $r = 0.5$ µm. However, the minimum reference radius of a human blood vessel is approximately 4 µm, so this should not impact the computed viscosity in any vessel.

We have chosen the bulk viscosity to be $\mu = 4.503\,\mathrm{mPa\,s}$ in large vessels for $H = 0.4$, and a function with which to compute the viscosity in small vessels for given radius. The human aorta has a typical radius on the order of 10^4 µm; the largest vessels that we model is the left pulmonary vein with a typical radius of 5000 µm. The smallest vessels that we include in the large tree have radii on the

order of 500 µm. The function μ_v predicts viscosities of 2.818, 2.812, 2.811 mPa s (4 s.f.), respectively. However, the Newtonian bulk viscosity should be applied in all of these vessels, and there is an large discontinuity that is physiologically unrealistic. In order to deal with this discontinuity, scale the function μ_v so that the predicted viscosity in large vessels (for now, those with radius above 600 µm) is $\mu = 4.503$ mPa s and define the function

$$\mu(r) := \begin{cases} 4.503 \frac{\mu_v(r)}{\mu_v(600)}, & \text{within the structured tree,} \\ 4.503 & \text{outwith the structured tree.} \end{cases}$$

In summary, whole blood is a non-Newtonian fluid, but it is often appropriate to assume that it is Newtonian for physiological shear-rates, thus allowing the use of a simplified model. In order to reconcile these with each other, we use a scaled, radius dependent model for viscosity in small vessels and a constant value for viscosity in large vessels.

2.2 Fluid Dynamics of Large Vessels

In this section we derive the governing equations for fluid motion within a large vessel network. Large vessels are those in which we explicitly solve the governing equations for all spatial and temporal points in the computational domain.

Our approach follows that of Olufsen [67], Vaughan [29], and Qureshi [3]. Olufsen's work [30, 43, 44, 67] is based on that of Barnard *et al.* [68] and Peskin [69]. Vaughan [29] and Qureshi [2, 3, 59, 70] builds on Olufsen's. These approaches takes us from a 3D system in cylindrical polar coordinates to a 1D problem via a series of rational approximations. The contents and contributions of these are discussed in Chapter 1.

A large blood vessel is assumed to be an axisymmetric tube with infinitesimally

thin, compliant walls. Large vessels have fixed and finite arc length, L, as vessels are tethered to surrounding tissues. Large vessels are allowed to taper, i.e. the distal radius may be less than the proximal radius in the reference configuration. Each point within the vessel is described by (r, x, θ) with $r \in [0, R(x,t))$, $x \in [0, L]$, and $\theta \in [0, 2\pi)$. Here, $R(x, \theta, t)$ denotes the variable radius of the tapering vessel at a fixed x position along the tube for all time t; so the lumen area $A(x, \theta, t) = \pi R^2(x, \theta, t)$ follows. Let the velocity field of the fluid be

$$\boldsymbol{u} = [u_r(r, x, \theta, t), u_x(r, x, \theta, t), u_\theta(r, x, \theta, t)],$$

where the subscript r, x, or θ represent the radial, axial, and angular components of the velocity field in cylindrical polar coordinates. Let $p(r, x, \theta, t)$ be pressure within the blood vessel and p_0 be a constant reference pressure.

We assume that fluid flow is laminar and swirl-free; i.e. there is no motion in the circumferential direction. Further assume that flow is axisymmetric. Together, these render flow and fluid pressure to be independent of the angular component θ. The velocity field becomes $\boldsymbol{u} = [u_r(r, x, t), u_x(r, x, t)]$, subscripts r and x denote the radial and axial components of the velocity, respectively. Furthermore, blood pressure, radius, and area in the current configuration become $p(r, x, t)$, and $R(x, t)$ and $A(x, t)$, respectively.

A key difference between the work described in this thesis and its predecessors is that we include a dynamic external pressure that can be applied to any or all vessels in a vascular network. The transmural pressure is the pressure difference that acts across the wall, defined as

$$\varphi(R(x,t), x, t) \coloneqq p(R(x,t), x, t) - \text{þ}(t). \tag{2.1}$$

The transmural pressure is the difference between the fluid pressure at the inner surface of the vessel wall and the external pressure on the outer surface. The inner

surface of the vessel occurs at radius $R(x,t)$. There is a radial pressure gradient between the pressure at the centreline and the pressure at the innermost surface of the wall. The external pressure $\text{þ}(t)$ is given. We assume that external pressure is constant on the length scale of a single vessel segment, where a segment runs between two successive junctions. This is not a necessary assumption, and one can follow Müller [31], who derives similar governing equations but with an external pressure that varies in both space and time. Müller developed his model with an emphasis on modelling flow in the long veins that supply drain blood from the brain; it is reasonable to expect that these segments have much greater length-to-radius ratios than those for the coronary circulation, as their function is primarily to transport blood, rather than to supply an organ. Our model is intended to model blood flow and pressure in the coronary and pulmonary circulations, both of which are comprised almost exclusively of vessels that are far shorter than those seen in Müller's. Further, as we derive governing equations for a single vessel, and solve them for each vessel individually we are free to prescribe a different external pressure for each vessel present. The reference pressure is set as $p_0 \coloneqq \min(\text{þ}(t))$ and occurs at some time $t = \tau$. The reference radius and lumen area also set at time τ: $R(x,\tau) = r_0(x)$, $A(x,\tau) = A_0(x)$. Fig. 2.3 shows a typical vessel segment in the reference configuration with the vessel lumen marked, as well an illustration of the relationship between reference radius and length along the vessel. The $x = 0$ end of the vessel is typically referred to as the proximal end (hence $r_0(0)$ is the proximal reference radius), and the $x = L$ end as distal.

We define *blood pressure* as the fluid pressure along the centreline of each vessel, it is denoted $p(0,x,t)$.

As blood is viscous, we apply the no-slip boundary condition, i.e. the velocity of the fluid at the wall is the same as the velocity of the wall. We consider the axial and

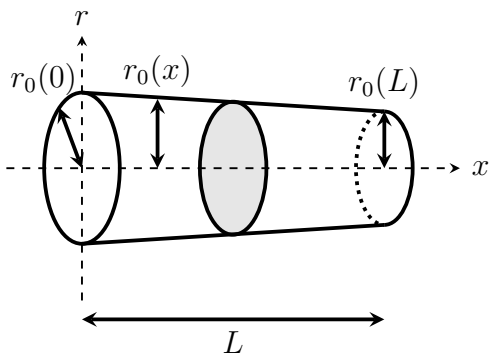

Figure 2.3: Cartoon of a single vessel segment with axial and radial directions shown in dotted lines. The length of the segment, L, is shown. Additionally, the relationship between reference radius and length along the vessel is indicated. The vessel lumen — cross-sectional area contained within the walls — is shown in grey.

radial components of the velocity separately. As vessels are longitudinally tethered, there is no axial movement of the wall, but the wall does experience motion in the radial direction. This gives the no-slip boundary condition

$$[u_x(r,x,t)]_{r=R(x,t)} = 0, \quad [u_r(r,x,t)]_{r=R(x,t)} = \left.\frac{\partial R}{\partial t}\right|_{(r,x)}. \tag{2.2}$$

2.2.1 Continuity Equation

We impose the incompressibility condition in cylindrical polar coordinates,

$$\nabla \cdot \boldsymbol{u} = \frac{1}{r}\frac{\partial}{\partial r}(ru_r) + \frac{1}{r}\frac{\partial u_\theta}{\partial \theta} + \frac{\partial u_x}{\partial x},$$

and given the above simplifying assumptions, we drop all θ-dependant terms to yield

$$\frac{\partial u_x}{\partial x} + \frac{1}{r}\frac{\partial}{\partial r}(ru_r) = 0, \tag{2.3}$$

a 2D equation. To obtain the 1D analogue, integrate over the cross-section to get

$$\begin{aligned} 0 &= \int_0^R \int_0^{2\pi} \left(\frac{\partial u_x}{\partial x} + \frac{1}{r}\frac{\partial}{\partial r}(r u_r) \right) r \, \mathrm{d}\theta \, \mathrm{d}r \\ &= 2\pi \left(\frac{\partial}{\partial x} \int_0^R r u_x \, \mathrm{d}r + \left[r u_r \right]_R - \int_0^R u_r \, \mathrm{d}r + \int_0^R u_r \, \mathrm{d}r \right) \\ &= \frac{\partial}{\partial x} \left(2\pi \int_0^R r u_x \, \mathrm{d}r \right) + 2\pi \left[r u_r \right]_R . \end{aligned} \tag{2.4}$$

Using the no-slip boundary condition to evaluate the second term of (2.4) yields

$$2\pi \left[r u_r \right]_R = 2\pi R \frac{\partial R}{\partial t} = \pi \frac{\partial R^2}{\partial t} = \frac{\partial A}{\partial t}, \tag{2.5}$$

and defining volumetric flux as

$$q(x,t) = 2\pi \int_0^R u_x r \, \mathrm{d}r \tag{2.6}$$

allows us to write (2.4) as

$$\frac{\partial q}{\partial x} + \frac{\partial A}{\partial t} = 0 \tag{2.7}$$

the 1D continuity equation.

We non-dimensionalise this by defining characteristic flow, length, and radius scales Q_0, L_0, R_0, respectively, so $q = Q_0 \bar{q}$, $x = L_0 \bar{x}$, $r = R_0 \bar{r}$, where the overbar denotes a dimensionless quantity. Further, note that area is non-dimensionalised so that $A = R_0^2 \bar{A}$.

Upon substitution into (2.7) and dropping the overbars for notational simplicity, we have the non-dimensional 1D continuity equation

$$\frac{\partial q}{\partial x} + \frac{\partial A}{\partial t} = 0. \tag{2.8}$$

2.2.2 The x-momentum Equation

Using the above swirl-free and axisymmetric assumptions, the Navier–Stokes equations in cylindrical polar coordinates become

$$\frac{\partial u_r}{\partial t} + u_r\frac{\partial u_r}{\partial r} + u_x\frac{\partial u_r}{\partial x} = -\frac{1}{\rho}\frac{\partial p}{\partial r} + \nu\left(\frac{\partial^2 u_r}{\partial r^2} + \frac{1}{r}\frac{\partial u_r}{\partial r} - \frac{u_r}{r^2} + \frac{\partial^2 u_r}{\partial x^2}\right) \tag{2.9a}$$

and

$$\frac{\partial u_x}{\partial t} + u_r\frac{\partial u_x}{\partial r} + u_x\frac{\partial u_x}{\partial x} = -\frac{1}{\rho}\frac{\partial p}{\partial x} + \nu\left(\frac{\partial^2 u_x}{\partial r^2} + \frac{1}{r}\frac{\partial u_x}{\partial r} + \frac{\partial^2 u_x}{\partial x^2}\right), \tag{2.9b}$$

as there is no dependence on an angular component.

Blood vessels are naturally much greater in length than in radius, i.e. $R_0 \ll L_0$ and so we define $\epsilon \coloneqq R_0/L_0 \ll 1$.

Further, the maximum velocity of the compliant vessel wall in the radial direction is u_r as the walls undergo little transverse motion. Hence, we may assume that typical radial fluid velocity is much less than typical axial velocity ($u_r \ll u_x$) in large blood vessels. Following Barnard [68], let U_0, V_0 be characteristic fluid velocities in the axial (x) and radial (r) directions, respectively. We may write $V_0 \ll U_0$, so $\epsilon = V_0/U_0 \ll 1$. Then we write $L_0 = R_0U_0/V_0$.

We define the scalings

$$u_x = U_0\bar{u}_x,\ u_r = V_0\bar{u}_r,\ t = \frac{L_0}{U_0}\bar{t},\ p = \rho U_0^2\bar{p}$$

in which non-dimensional quantities are denoted by an overbar. Using these, we non-dimensionalise Eqs. 2.9, and upon dropping overbars we obtain

$$\frac{\partial p}{\partial r} = -\epsilon^2\left\{\frac{\partial u_r}{\partial t} + u_r\frac{\partial u_r}{\partial r} + u_x\frac{\partial u_r}{\partial x} - \frac{1}{\mathcal{R}}\left(\frac{\partial^2 u_r}{\partial r^2} + \frac{1}{r}\frac{\partial u_r}{\partial r} - \frac{u_r}{r^2} + \epsilon^2\frac{\partial^2 u_r}{\partial x^2}\right)\right\}, \tag{2.10a}$$

$$\frac{\partial u_x}{\partial t} + u_r\frac{\partial u_x}{\partial r} + u_x\frac{\partial u_x}{\partial x} = -\frac{\partial p}{\partial x} + \frac{1}{\mathcal{R}}\left(\frac{\partial^2 u_x}{\partial r^2} + \frac{1}{r}\frac{\partial u_x}{\partial r} + \epsilon^2\frac{\partial^2 u_x}{\partial x^2}\right) \tag{2.10b}$$

where $\mathcal{R} = R_0 V_0/\nu$, and $\mathcal{R}$ is Reynolds number.

As $\epsilon \ll 1$, (2.10a) implies that $\partial p/\partial r = \mathcal{O}(\epsilon^2) \ll 1$. This result is similarly found by Barnard [68]. This result along with the axisymmetry assumption imply that fluid pressure only varies axially and temporally, i.e. $p = p(x,t)$. As the radial dependence has dropped from p, it must drop from φ, too. Henceforth, $\varphi = \varphi(x,t) = p(x,t) - \text{Þ}(t)$.

External pressure, $\text{Þ}(t)$, depends on time alone as we assume spatial variation on the length-scale of a single vessel is negligible. The current analysis is valid for a single vessel segment, not a network. The theory that is being developed allows for a different external pressure to be applied to every vessel in the network, so that the external pressure can be made to vary on the whole organ scale.

Furthermore, the final term of (2.10b) is negligible and the equation becomes

$$\frac{\partial u_x}{\partial t} + u_r \frac{\partial u_x}{\partial r} + u_x \frac{\partial u_x}{\partial x} = -\frac{\partial p}{\partial x} + \frac{1}{\mathcal{R}} \left(\frac{\partial^2 u_x}{\partial r^2} + \frac{1}{r} \frac{\partial u_x}{\partial r} \right). \tag{2.11}$$

We seek a 1D version of the above and achieve this by integrating over the cross-section

$$\begin{aligned} &\int_0^{2\pi} \int_0^R \left(\frac{\partial u_x}{\partial t} + u_r \frac{\partial u_x}{\partial r} + u_x \frac{\partial u_x}{\partial x} \right) r \ \mathrm{d}r \ \mathrm{d}\theta \\ &= \int_0^{2\pi} \int_0^R \left(-\frac{\partial p}{\partial x} + \frac{1}{\mathcal{R}} \left(\frac{\partial^2 u_x}{\partial r^2} + \frac{1}{r} \frac{\partial u_x}{\partial r} \right) \right) r \ \mathrm{d}r \ \mathrm{d}\theta. \end{aligned}$$

Evaluating the integrals in θ gives

$$\begin{aligned} &2\pi \int_0^R \frac{\partial u_x}{\partial t} r \ \mathrm{d}r + 2\pi \int_0^R \left(u_r \frac{\partial u_x}{\partial r} + u_x \frac{\partial u_x}{\partial x} \right) r \ \mathrm{d}r \\ &= -2\pi \int_0^R \frac{\partial p}{\partial x} r \ \mathrm{d}r + 2\pi \frac{1}{\mathcal{R}} \int_0^R \left(\frac{\partial^2 u_x}{\partial r^2} + \frac{1}{r} \frac{\partial u_x}{\partial r} \right) r \ \mathrm{d}r. \end{aligned} \tag{2.12}$$

For simplicity, we deal with this term-by-term. We evaluate the leftmost term using the product rule and integration by parts, and applying the definition of volumetric

flow and the no-slip boundary condition:

$$\begin{aligned} 2\pi \int_0^R \frac{\partial u_x}{\partial t} r \ \mathrm{d}r &= 2\pi \left(\frac{\partial}{\partial t} \left(\int_0^R u_x r \ \mathrm{d}r \right) - \int_0^R u_x \frac{\partial r}{\partial t} \ \mathrm{d}r \right) \\ &= 2\pi \left[u_x r \right]_0^R - 2\pi \int_0^R u_x \frac{\partial r}{\partial t} \ \mathrm{d}r = \frac{\partial q}{\partial t} - 2\pi \frac{\partial R}{\partial t} \left[r u_x \right]_0^R = \frac{\partial q}{\partial t}. \end{aligned} \tag{2.13}$$

The second term of the left hand side is

$$\begin{aligned} & 2\pi \int_0^R \left(u_r \frac{\partial u_x}{\partial r} + u_x \frac{\partial u_x}{\partial x} \right) r \ \mathrm{d}r \\ &= 2\pi \left(\left[u_x u_r r \right]_0^R - \int_0^R u_x \frac{\partial}{\partial r} (r u_r) \ \mathrm{d}r \right) + 2\pi \int_0^R u_x \frac{\partial u_x}{\partial x} r \ \mathrm{d}r \\ &= 4\pi \int_0^R u_x r \frac{\partial u_x}{\partial x} \ \mathrm{d}r \\ &= 2\pi \int_0^R \frac{\partial u_x^2}{\partial x} r \ \mathrm{d}r \end{aligned} \tag{2.14}$$

by integration by parts, application of the no-slip boundary condition (2.2), and the incompressibility condition (2.3).

The first term on the right hand side of (2.12) is easily integrated, as fluid pressure p is independent of radius,

$$2\pi \int_0^R \frac{\partial p}{\partial x} r \ \mathrm{d}r = 2\pi \frac{\partial p}{\partial x} \int_0^R r \ \mathrm{d}r = \pi R^2 \frac{\partial p}{\partial x} = A \frac{\partial p}{\partial x}. \tag{2.15}$$

The final terms on the right hand side evaluate as follows

$$\begin{aligned} \int_0^R \left(\frac{\partial^2 u_x}{\partial r^2} r + \frac{\partial u_x}{\partial r} \right) \ \mathrm{d}r &= \int_0^R \left(\frac{\partial^2 (u_x r)}{\partial r^2} - \frac{\partial u_x}{\partial r} \right) \ \mathrm{d}r \\ &= R \left[\frac{\partial u_x}{\partial r} \right]_{r=R}. \end{aligned} \tag{2.16}$$

This term encodes the frictional force in the axial direction at the wall.

Equation (2.12) is simplified to

$$\frac{\partial q}{\partial t} + 2\pi \int_0^R \frac{\partial u_x^2}{\partial x} r \, \mathrm{d}r = -A\frac{\partial p}{\partial x} + \frac{2\pi}{\mathcal{R}} \left[R \frac{\partial u_x}{\partial r} \right]_{r=R}. \tag{2.17}$$

In order to evaluate the u_x^2 term in (2.14) and the frictional force term $\partial u_x/\partial r$ in (2.16), we require a velocity profile. Studies show that the shape of velocity profiles develop from a flat profile at the aortic inlet to a parabolic profile at the resistance arteries [71, 72].

Maier *et al.* [72] acquired velocity profiles in the abdominal aorta of healthy volunteers using MRI and multigated doppler studies. They present fifteen meshes representing velocity profiles in a single individual over the course of 435 ms, clearly showing that velocity profiles evolve throughout the cardiac cycle. The change of velocity profile in time was also noted by Zhong *et al.* [73] in the retinal vessels of healthy volunteers; they also found that velocity profiles are typically flatter than the assumed parabolic shape which was not found even in the largest veins studied with radii > 80 µm, and that profile flatness increased with decreasing vessel size. Further, Tangelder *et al.* [74] determined *in vivo* velocity profiles in rabbit mesenteric arterioles of radius 17 — 32 µm; profiles for red blood cells and platelets were found to be flattened compared to a parabola in both systole and diastole.

The change in profile over the cardiac cycle is captured by the model as fluid velocity changes, but given the findings of Zhong *et al.* , I choose to assume a Stokes-layer velocity profile introduced by Olufsen *et al.* [30] for the systemic circulation, and subsequently used by Qureshi [3] for the pulmonary circulation and Chen [40] for a coupled model of the systemic circulation and the left ventricle. The velocity profile is

$$u_x(r,x,t) = \begin{cases} \bar{u}_x(x,t), & \text{for } r \leq R-\delta, \\ \bar{u}_x(x,t)\frac{(R-r)}{\delta} & \text{for } R-\delta < r \leq R \end{cases}, \tag{2.18}$$

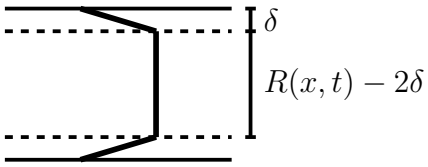

Figure 2.4: An illustration of an entry type flow profile such as that given in (2.18). Boundary layers of width δ are shown between the dotted and solid lines.

where $\bar{u}_x(x,t)$ is the constant axial velocity outside of the boundary layer which we define as a region of thickness $\delta \ll R$ along the walls. A cartoon of this profile is shown in Fig. 2.4. In this layer, the viscous effects are strong and the transition to the no-slip boundary takes place. We can estimate this thickness as per Lighthill [75]; this estimate is from the viscous penetration depth based upon the first harmonic

$$\delta = \sqrt{\left(\frac{\nu T}{2\pi}\right)}.$$

Alastruey *et al.* [76], Sherwin *et al.* [77] and Matthys *et al.* [78] use a constant, axisymmetric velocity profile. Sherwin *et al.* extend their analysis to more a generic, undefined profile that is not flat but is still axisymmetric. Matthys *et al.* obtain their velocity profile by assuming axisymmetry and fitting to experimental data measured at different points in the cardiac cycle. Cousins & Gremaud [79] use a parabolic profile when modelling flow in the circle of Willis.

We can now evaluate (2.14), (2.16) using (2.18). The former becomes

$$\begin{aligned}
2\pi\frac{\partial}{\partial x}\int_0^R u_x^2 r \,\mathrm{d}r &= 2\pi\frac{\partial}{\partial x}\left(\int_0^{R-\delta} \bar{u}_x^2 r \,\mathrm{d}r + \int_{R-\delta}^{R}\left(\frac{\bar{u}_x(R-r)}{\delta}\right)^2 r \,\mathrm{d}r\right) \\
&= 2\pi\frac{\partial}{\partial x}\left[\left(\bar{u}_x^2\right)\left\{\frac{(R-\delta)^2}{2} + \frac{\delta}{12}\left(4R-3\delta\right)\right\}\right] \\
&= \frac{\partial}{\partial x}\left[\left(\bar{u}_x^2\right)\left\{A - \frac{4}{3}\delta\frac{A}{R} + \mathcal{O}(\delta^2)\right\}\right]
\end{aligned}$$

N. B. $\delta^2 \ll 1$, $\delta/R \ll 1$. Given that

$$q = 2\pi \int_0^R u_x r \, \mathrm{d}r = A\bar{u}_x - A\bar{u}_x \frac{\delta}{R} + \mathcal{O}\left(\delta^2\right), \tag{2.19}$$

we have

$$2\pi \frac{\partial}{\partial x} \int_0^R u_x^2 r \, \mathrm{d}r = \frac{\partial}{\partial x}\left(\frac{q^2}{A}\right) + \mathcal{O}(\delta). \tag{2.20}$$

Revisiting (2.16) now with an explicit expression for the velocity profile, we have

$$\int_0^R \left(\frac{\partial^2 u_x}{\partial r^2} r + \frac{\partial u_x}{\partial r}\right) \mathrm{d}r = R\left[\frac{\partial u_x}{\partial r}\right]_{r=R} = R\left[\frac{\partial}{\partial r}\left(\bar{u}_x \frac{R-r}{\delta}\right)\right]_R \tag{2.21}$$

by the expression for q in (2.19)

$$\frac{q}{A - A\frac{\delta}{R}} = \bar{u}_x + \mathcal{O}\left(\delta^2\right)$$

Substituting (2.13), (2.15), (2.20) and (2.21) back into 2.12 yields the dimensionless 1D x-momentum equation

$$\frac{\partial q}{\partial t} + \frac{\partial}{\partial x}\left(\frac{q^2}{A}\right) + A\frac{\partial p}{\partial x} = -\frac{2\pi R}{\delta \mathcal{R}} \frac{q}{A}. \tag{2.22}$$

2.2.3 Constitutive Tube Law

Between them (2.8), (2.22) have three unknowns, so the system is under-determined. We require a third equation that relates at least two of A, p, q. The third equation is a tube law, that allows us to write φ as a function of A. The other parameters upon which φ depends can be, for example wall stiffness and reference radius. Empirically measured tube laws are determined under specific ranges of, for example, pressure, so are only valid in the pressure range in which they were determined [80]. There are many choices of tube law that one can make, that are discussed in more detail in, e.g. [81], which is concerned with the derivation of a tube law for bronchial airways based on experimental data, and [82] an experimental study of elastic walled tubes,

and a comparison between these results and existing theoretical descriptions. There also exist studies, e.g. [83], that derive tube laws from a theoretical, rather than experimental stand point.

We choose to use the tube law

$$\varphi(x,t) \ = p(x,t) - \text{Þ}(t) = \frac{4}{3}\frac{Eh}{r_0(x)}\left(\sqrt{\frac{A(x,t)}{A_0(x)}} - 1\right) \equiv \hat{\varphi}(A(x,t), r_0(x,t)), \quad (2.23)$$

where E is the Young's modulus, and h is the wall thickness. Both E and h are constant in a single section of tube; $r_0(x)$ is a decreasing function depending on the vessel in question. This tube law is also used by Qureshi and colleagues [70, 84], and appears to have been originally proposed by Lighthill [85]. For notational convenience, let

$$f(r_0(x)) = \frac{4}{3}\frac{Eh}{r_0(x)}.$$

This functional encodes the elastic properties of the vessel wall for a given reference radius. Coronary arteries and veins, and pulmonary arteries and veins all have very different characteristic stiffnesses. See Chapter 4 and Chapter 5 for discussions of pulmonary and coronary vessel stiffness. So

$$\hat{\varphi}(A(x,t), r_0(x,t)) = f(r_0(x))\left(\sqrt{\frac{A(x,t)}{A_0(r_0(x))}} - 1\right).$$

Above and henceforth I use a hat ($\hat{}$) to indicate that the expression is a functional – it depends on quantities that depend on x and/or t.

We may write A as a function of φ and r_0 as follows

$$\hat{A}(\varphi(t), r_0(x,t)) = A_0\left(\frac{\varphi}{f(r_0)} + 1\right)^2. \quad (2.24)$$

Further, given $\hat{\varphi}$, we can write

$$\hat{p}(A(x,t), r_0(x,t)) = f(r_0)\left(\sqrt{\frac{A}{A_0}} - 1\right) + \text{Þ}.$$

We should non-dimensionalise the tube law as we did the x-momentum and conservation of mass equations (2.11), (2.8). Using the scalings

$$A = R_0^2 \bar{A},\ \varphi = \rho U_0^2 \bar{\varphi},\ f = \rho U_0^2 \bar{f},$$

we see that the dimensionless tube law is

$$\varphi(A) = \hat{f}\left(\sqrt{\frac{\hat{A}}{A_0}} - 1\right) \tag{2.25}$$

after dropping over-bars for ease of notation.

We now have three one-dimensional, dimensionless governing equations (2.8), (2.22) and (2.23). Between them, they have three unknowns A, p and q. Hence, the system is well determined.

2.3 Fluid Dynamics of Small Vessels

Large vessels are defined as those in which we explicitly model blood flow and pressure. Small blood vessels are modelled using a structured tree approach. We use a structured tree to provide the arterial/venous boundary matching condition as this approach captures pulse wave propagation into the venous side [29], and they can be implemented using only physically meaningful parameters. Lumped parameter models such as three- or four- element Windkessel models have parameters that have no direct physical analogue, so must be set using data from the literature [86].

The vessels of a structured tree arise from the terminus of a large artery with known radius. They bifurcate from the root vessel with prescribed ratios that govern the length and radius of each daughter vessel.The arterial side of the tree truncates when some minimum prescribed radius has been reached. The venous branching structure is taken to be identical to that of the arteries, but the venous length and

ratio governing parameters need not be the same as those for arteries. There is one structured tree per large arterial/venous pair to be joined.

In order to build a network, we must start with a single vessel derive its governing equations. Much of the theory for the fluid dynamics of large vessels applies to small vessels. Indeed, everything in the section for large vessel fluid dynamics until (2.11) is also true for small vessels. We use the same constitutive relation for small and large vessels, but this need not be the case. All of the below theory is applicable when a generic tube law is used.

From our universal assumptions above, recall the dependencies of blood flow $q(r, x, t)$, fluid velocity $u_x(r, x, t)$, blood pressure $p(x, t)$, transmural pressure $\varphi(x, t)$, and external pressure $\text{þ}(t)$ on the radial, longitudinal, and temporal components, respectively.

Blood flow is driven by the beating of the heart so we assume blood pressure, fluid velocity, and flow rate are periodic in time and write them as Fourier series:

$$\begin{aligned} p(x,t) &= \sum_{n=-\infty}^{\infty} P_n(x) e^{in\omega t}, \\ u_x(x,r,t) &= \sum_{n=-\infty}^{\infty} U_n(r,x) e^{in\omega t}, \\ q(x,r,t) &= \sum_{n=-\infty}^{\infty} Q_n(r,x) e^{in\omega t}, \end{aligned} \tag{2.26}$$

with Fourier coefficients given by

$$\begin{aligned} P_n(x) &= \frac{1}{T} \int_{-T/2}^{T/2} p(x,t) e^{(in\omega t)} \, \mathrm{d}t, \\ U_n(r,x) &= \frac{1}{T} \int_{-T/2}^{T/2} u_x(r,x,t) e^{(in\omega t)} \, \mathrm{d}t, \\ Q_n(r,x) &= \frac{1}{T} \int_{-T/2}^{T/2} q(r,x,t) e^{(in\omega t)} \, \mathrm{d}t, \end{aligned}$$

respectively. These all have the same period, T. The Fourier mode is the integer n.

External pressure is assumed to be periodic with period T'. External pressure arises from breathing or the beating of the heart that compress small vessels; we acknowledge that the period and amplitude of both change overtime, but assume that such changes do not happens on time scales less than T' (about 1 s for the coronary model and 10 s for the pulmonary model). Note that for the coronary model $T' = T$. It is written as a complex Fourier series

$$\text{Þ}(t) = \sum_{n=-\infty}^{\infty} \text{Þ}_n e^{in\omega t}, \tag{2.27}$$

with Fourier coefficients

$$\text{Þ}_n = \frac{1}{T'} \int_{-T'/2}^{T'/2} \text{Þ}(t) e^{in\omega t} \, \mathrm{d}t.$$

External pressure need not have the same period as blood pressure. However, we require that there exist integers r, s such that

$$rT = sT', \text{ or } \frac{T}{T'} \in \mathbb{R}.$$

By construction, the transmural pressure φ, it is periodic with period rT and has Fourier series

$$\varphi(x,t) = \sum_{n=-\infty}^{\infty} \Phi_n(x) e^{in\omega t} = \sum_{n=-\infty}^{\infty} \left(P_n(x) - \text{Þ}\right) e^{in\omega t} \tag{2.28}$$

and Fourier coefficient

$$\Phi_n(x) = \frac{1}{sT} \int_{-sT/2}^{sT/2} \varphi(x,t) e^{in\omega t} \, \mathrm{d}t.$$

It is important to note that the above Fourier series and coefficients are dimensional quantities.

The pulse wave wavelength is the product of its velocity and period. As typical pulse wave velocities in healthy humans are on the scale of ms^{-1} [87] and the period on the scale of s, the typical wavelength of a pressure pulse is on the order of 5 m. The wavelength of a pressure pulse is significantly longer than any vessel segment in the network. It follows that the velocity profile is flat and velocities in the radial direction can be neglected. With this assumption, it follows that

$$u_r \frac{\partial u_x}{\partial r}, \quad u_x \frac{\partial u_x}{\partial x} \ll 1.$$

Hence, at leading order (2.11) becomes

$$\frac{\partial u_x}{\partial t} + \frac{\partial p}{\partial x} = \frac{1}{r\mathcal{R}} \frac{\partial}{\partial r} \left(r \frac{\partial u_x}{\partial r} \right) \tag{2.29}$$

which is the dimensionless, scaled x-momentum equation for small vessels. Into this, we substitute the Fourier series (2.26) which yields

$$in\omega U_n + \frac{\mathrm{d}P_n}{\mathrm{d}x} = \frac{1}{r\mathcal{R}} \frac{\partial}{\partial r} \left(r \frac{\partial U_n}{\partial r} \right), \tag{2.30}$$

upon cancelling $e^{in\omega t}$ throughout.

Henceforth, we consider the non-zero frequencies separately from the steady case.

2.3.1 Non-Zero Frequencies

Non-zero frequency solutions are valid when $n \neq 0$.

Equation (2.30) has a Womersley's solution as discussed by Womersley [26] for each non-zero Fourier mode

$$U_n = \frac{1}{in\omega} \frac{\mathrm{d}P_n}{\mathrm{d}x} \left(1 - \frac{J_0(rw_n/r_0)}{J_0(w_n)} \right),$$

where $\omega = 2\pi/T$ is the angular frequency with period T, $w_n^2 = i^3\alpha_n$, and $\alpha_n^2 = r_0\omega n\mathcal{R}/\rho$. Now, $\alpha_1 \equiv \alpha$ is Womersley's parameter. The function J_0 is a zeroth order Bessel's function of the first kind; see, for example, Dattoli & Torre [88].

We can find the amplitude Q_n of the flow q by integrating over the cross sectional area,

$$Q_n(x) = 2\pi \int_0^{r_0} U_n r \, \mathrm{d}r = -\frac{A_0}{in\omega}\frac{\mathrm{d}P_n}{\mathrm{d}x}(1 - F_J) \tag{2.31}$$

where $F_J := 2J_1(w_n)/w_n J_0(w_n)$; J_1 is the first order Bessel's function of the first kind.

Using equation (2.24), we write

$$\begin{aligned} \frac{\partial A}{\partial t} &= \frac{\partial A}{\partial \varphi}\frac{\partial \varphi}{\partial t} \\ &= C\frac{\partial}{\partial t}(p - \text{Þ}) \end{aligned} \tag{2.32}$$

where the compliance $C = (\mathrm{d}A/\mathrm{d}\varphi) \approx 3r_0A_0/2Eh$ using the linearising assumption $r_0\varphi \ll Eh$ [3]. Substituting $\partial A/\partial t$ into (2.32) and comparing the coefficients of the Fourier expansions yields

$$iCn\omega(P_n - \text{Þ}_n) + \frac{\mathrm{d}Q_n}{\mathrm{d}x} = 0. \tag{2.33}$$

Differentiating (2.33) with respect to x, and rearranging gives

$$\frac{\mathrm{d}P_n}{\mathrm{d}x} = -\frac{1}{iCn\omega}\frac{\mathrm{d}^2Q_n}{\mathrm{d}x^2}, \tag{2.34}$$

which we substitute into (2.31) to obtain

$$\frac{\mathrm{d}^2Q_n}{\mathrm{d}x^2} + \left(\frac{\omega n}{c}\right)^2 Q_n = 0 \tag{2.35}$$

where $c^2 = A_0(1 - F_J)/C$, and c is the dimensionless wavespeed. Equation (2.35) is the equation of simple harmonic motion and has a well known solution,

$$Q_n(r, x) = a_n \cos\left(\frac{n\omega}{c}x\right) + b_n \sin\left(\frac{n\omega}{c}x\right), \tag{2.36}$$

where a_n and b_n are constant coefficients that depend on the Fourier mode n, and $n \in [1, \infty)$. Substituting (2.36) into (2.33) yields the expression for the transmural pressure

$$\Phi_n = P_n - \text{Þ}_n = \frac{i}{Cc}\left(-a_n \sin\left(\frac{n\omega}{c}x\right) + b_n \cos\left(\frac{n\omega}{c}x\right)\right). \tag{2.37}$$

2.3.2 Steady Case

Now consider the steady case, $n = 0$. From (2.30)

$$\frac{\mathrm{d}P_0}{\mathrm{d}x} = \frac{1}{r\mathcal{R}}\frac{\partial}{\partial r}\left(r\frac{\partial U_0}{\partial r}\right)$$

integrating twice with respect to r gives

$$U_0 = \frac{\partial P_0}{\partial x}\frac{r^2\mathcal{R}}{4} + \Lambda\mathcal{R}\ln r + \Xi$$

where Λ and Ξ are constants of integration. Determine Λ by assuming that $\partial U_0/\partial r$ is finite at $r = 0$, implying that $\Lambda = 0$, and Ξ by applying the no-slip boundary condition, $U_0(r_0) = 0$, which implies that $\Xi = -(r_0^2\mathcal{R}/4)\,(\mathrm{d}P_0/\mathrm{d}x)$. We hence have the velocity profile

$$U_0(r, x) = \frac{(r^2 - r_0^2)\,\mathcal{R}}{4}\frac{\mathrm{d}P_0}{\mathrm{d}x}. \tag{2.38}$$

This is a Poiseuille flow profile, which satisfies the incompressibility condition (2.7), as the fluid pressure gradient is constant in x.

As in the non-zero frequency case, we integrate the fluid velocity over the cross sectional area to find the flow Q_0

$$Q_0(r, x) = 2\pi\int_0^{r_0} Ur\ \mathrm{d}r = -\frac{\pi\mathcal{R}}{8}\frac{\mathrm{d}P_0}{\mathrm{d}x}r_0^4 \tag{2.39}$$

which we solve for P_0 and find

$$P_0 = -\frac{8\Psi}{\pi r_0^4\mathcal{R}}x + \Gamma \tag{2.40}$$

where Ψ and Γ are constants of integration.

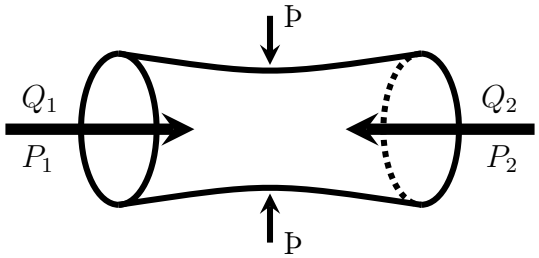

Figure 2.5: A cartoon showing a single vessel segment with inlet flow and pressure Fourier coefficients Q_1, P_1, and outflow flow and pressure Fourier coefficients Q_2, P_2. Inward orientation by convention. There is an external pressure of Þ applied uniformly along the length of the tube. The bowing of the walls in the centre of the tube is intended to imply that the walls are compliant.

2.3.3 Admittance for a Single Vessel

A structured tree is a collection of segments of tube joined together in series or in parallel with other tube segments. A cartoon of such a tube segment is shown in Fig. 2.5. An admittance matrix allows us to relate, for example, flow at the inlet and outlet to pressure at the inlet and outlet. We seek a relationship between flow and pressure at the inlet and outlet of a structured tree. The admittance matrix for the whole structured tree is called the grand admittance. As a structured tree is composed of single tube segments joined together, the grand admittance must be a function of the admittances for each vessel segment. In this section we discuss the admittance for a single vessel, before moving onto admittances for vessels in series and in parallel, and an algorithm that allows us to compute the grand admittance.

With the exception of the first vessel within the tree (which arises from a large artery) every vessel arises from a bifurcation. Each vessel bifurcates into two additional vessels until the segments achieve some prescribed minimum radius. The

admittance matrices that we seek relate the flows at either end of the tube, to the pressures. So in order to find the admittance matrices we first need expressions for the flows and pressures at $x = 0$ and $x = L$ in a vessel of finite length L.

Equations (2.36, 2.37, 2.39, 2.40) are already non-dimensional, so we simply collect the governing equations for flow and pressure in steady and unsteady cases for the convenience of the writer. For the unsteady components ($n = 1, 2, ...$) we have

$$\begin{aligned} \Phi_n &= P_n - \text{Þ}_n = \frac{i}{Cc}\left(-a_n \sin\left(\frac{n\omega}{c}x\right) + b_n \cos\left(\frac{n\omega}{c}x\right)\right), \\ Q_n &= a_n \cos\left(\frac{n\omega x}{c}\right) + b_n \sin\left(\frac{n\omega x}{c}\right), \end{aligned} \tag{2.41}$$

and

$$\begin{aligned} P_0(x) &= -\frac{8\Psi}{\pi r_0^4 \mathcal{R}}x + \Gamma, \\ Q_0(r, x) &= \Psi \end{aligned} \tag{2.42}$$

for the steady part of the flow.

Unsteady Component

To find the flows and pressures at the inlet and outlet of a tube of finite length L, we first define the inlet of the tube to be at $x = 0$, hence the outlet at $x = L$. We then evaluate Eqs. (2.41) at $x = 0, L$. A notational simplification can be made be defining $Q_n(0) \equiv Q_1$ and $Q_n(L) \equiv -Q_2$ (sign by convention), and $\Phi_n(0) \equiv \Phi_1$, $\Phi_n(L) \equiv \Phi_2$ where we neglect to write the suffixes n, as the following analysis is valid for all $n \neq 0$. Let $\boldsymbol{Q} = (Q_1, Q_2)^{\mathrm{T}}$, $\boldsymbol{\Phi} = (\Phi_1, \Phi_2)^{\mathrm{T}}$. We seek an admittance matrix Y that

satisfies $\boldsymbol{Q} = Y\boldsymbol{\Phi}$. For ease of notation, let $C_L := \cos(n\omega L/c)$ and $S_L := \sin(n\omega L/c)$

$$\Phi_1 = \frac{i}{cC} b_n, \tag{2.43}$$

$$\Phi_2 = \frac{i}{cC}(-a_n S_L + b_n C_L), \tag{2.44}$$

$$Q_1 = a_n = Y_{11}\Phi_1 + Y_{12}\Phi_2, \tag{2.45}$$

$$Q_2 = -(a_n C_L + b_n S_L) = Y_{21}\Phi_1 + Y_{22}\Phi_2 \tag{2.46}$$

Taking all of this together and comparing the coefficients a_n, b_n we find the admittance matrix

$$Y = \frac{icC}{S_L}\begin{bmatrix} -C_L & 1 \\ 1 & -C_L \end{bmatrix}. \tag{2.47}$$

That is,

$$\begin{aligned} \begin{pmatrix} Q_n(0) \\ Q_n(L) \end{pmatrix} &= \frac{icC}{S_L}\begin{bmatrix} -C_L & 1 \\ 1 & -C_L \end{bmatrix}\begin{pmatrix} \Phi_n(0) \\ \Phi_n(L) \end{pmatrix} \\ &= Y\left[\begin{pmatrix} P_n(0) \\ P_n(L) \end{pmatrix} - Þ_n \begin{pmatrix} 1 \\ 1 \end{pmatrix}\right]. \end{aligned} \tag{2.48}$$

Steady Component

We must also find an admittance matrix for a single tube in the zero frequency domain. This is done in a very similar manner to the non-zero frequency case. That is, evaluate Eqs. (2.42) at $x = 0,\ L$:

$$\begin{aligned} P_0(0) &= \Gamma \equiv P_1 \\ Q_0(0) &= \Psi \equiv Q_1 \\ P_0(L) &= -\frac{8\mu\Psi L}{\pi r_0^4} + \Gamma \equiv P_2 \\ Q_0(L) &= \Psi \equiv -Q_2 \end{aligned}$$

Note that the pressures given here are fluid pressures, not transmural pressures, and that there is no dependence on the external pressure. Again, we seek a matrix Y such that $\boldsymbol{Q} = Y\boldsymbol{P}$ where $\boldsymbol{Q} = [Q_1, Q_2]^{\mathrm{T}}$, $\boldsymbol{P} = [P_1, P_2]^{\mathrm{T}}$, hence $Q_1 = Y_{11}P_1 + Y_{12}P_2$ and $Q_2 = Y_{21}P_1 + Y_{22}P_2$. Explicitly, this is

$$\Psi = Y_{11}\Gamma + Y_{12}\left(-\frac{8\Psi L}{\pi r_0^4 \mathcal{R}} + \Gamma\right) \tag{2.49}$$

$$-\Psi = Y_{21}\Gamma + Y_{22}\left(-\frac{8\Psi L}{\pi r_0^4 \mathcal{R}} + \Gamma\right) \tag{2.50}$$

which we solve for Y_{ij}, $i, j = 1, 2$. This yields the admittance matrix Y for the steady case

$$Y = \frac{\pi r_0^4}{8\mu L}\begin{bmatrix} 1 & -1 \\ -1 & 1 \end{bmatrix}. \tag{2.51}$$

Which is identical to the admittance matrix found by Qureshi [2, 3].

2.3.4 Admittance for Vessels in Parallel

Consider two vessels, S and T in parallel with each other, as in Fig. 2.6. Denote the admittance matrix, flow, and fluid pressure of these as in the case for the single pipe, but with an S or T appended to denote the tube to which the quantity belongs, e.g. for vessel S, Q_1^S denotes the flow at the inlet and, Q_2^S the flow at the outlet, etc.

We must also define the matching conditions for the two pipes. These are $Q_j = Q_j^S + Q_j^T$, $j = 1, 2$, and $P_k = P_k^S = P_k^T$, $k = 1, 2$, as per Qureshi [2].

For each vessel we must have flows and pressures at the inlet and outlet such that they are related by admittance matrices:

$$\boldsymbol{Q}^S = Y^S\boldsymbol{\Phi}^S, \quad \boldsymbol{Q}^T = Y^T\boldsymbol{\Phi}^T.$$

Using the matching conditions from [3] that are illustrated in and noting that $\Phi_2^S \neq \Phi_1^T$ as $\Phi_1^j = P_1^j - \text{Þ}^j$, $j = S, T$ and $\text{Þ}^S \neq \text{Þ}^T$ (that is, the imposed external pressure

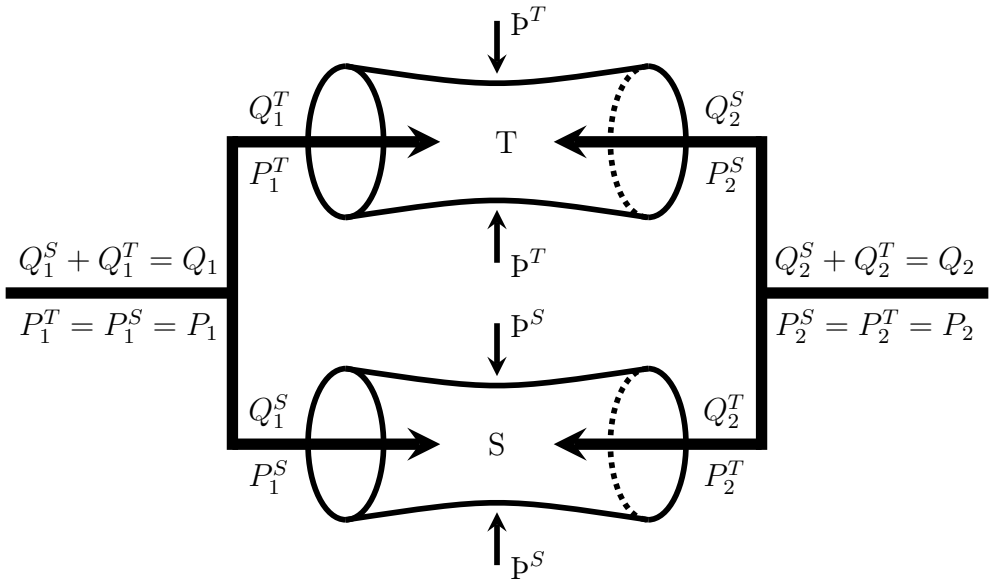

Figure 2.6: A cartoon of joining two vessels in parallel. As with the single vessel segment (Fig. 2.5), inlet and outlet flow and pressure Fourier coefficients are shown. Subscripts indicate an inlet/outlet quantity. Superscripts denote the tube to which the quantity belongs. Quantities without superscripts exist for ease of notation, and are given by segment matching conditions. External pressures Þ^S, Þ^T are applied uniformly along the length of their respective tubes.

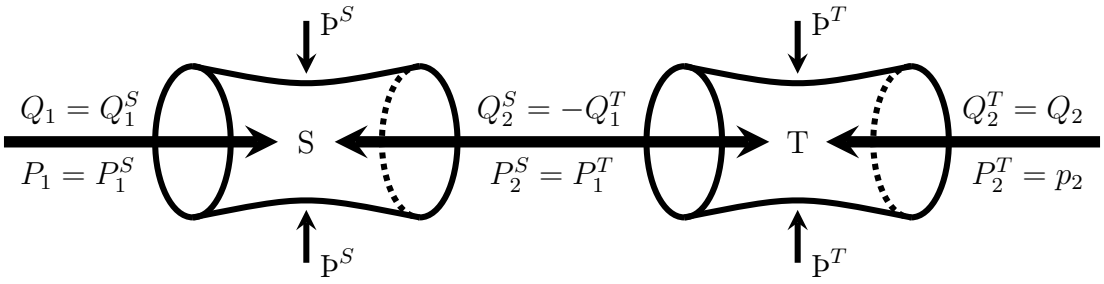

Figure 2.7: Cartoon of joining vessel segments S and T in series with inlet, outlet, and matching conditions shown. Each vessel is subject to some external pressure that is exerted uniformly along its length.

need not be the same for each vessel). Using the notation for a single vessel segment, we can write

$$\boldsymbol{Q}^S = Y^S \boldsymbol{P} - Y^S \boldsymbol{\mathfrak{P}}^S, \quad \boldsymbol{Q}^T = Y^T \boldsymbol{P} - Y^T \boldsymbol{\mathfrak{P}}^T$$
$$\boldsymbol{Q} = \boldsymbol{Q}^S + \boldsymbol{Q}^T = Y^{||} \boldsymbol{P} - Y^S \boldsymbol{\mathfrak{P}}^S - Y^T \boldsymbol{\mathfrak{P}}^T$$

where $\boldsymbol{\mathfrak{P}}^T = \mathfrak{P}^T \begin{pmatrix} 1 \\ 1 \end{pmatrix}$, similarly for $\boldsymbol{\mathfrak{P}}^S$, so

$$Y^{||} = Y^S + Y^T \tag{2.52}$$

is the admittance matrix for two vessels joined in parallel.

2.3.5 Admittance for Vessels in Series

We now consider two vessels, S and T, that are in series with each other, as is pictured above. As before we seek an admittance matrix for this set up. That is we wish to express Q_1^S and Q_2^T in terms of P_1^S and P_2^T via a (2×2) admittance matrix $Y^{\Leftrightarrow}$. The flows and pressures at the inlets and outlets of both S and T may

be related to each other as before, i.e.

$$\boldsymbol{Q}^S = Y^S \tilde{\boldsymbol{P}}^S = Y^S \boldsymbol{P}^S - Y^S \boldsymbol{\text{Þ}}^S$$

$$\begin{pmatrix} Q_1^S \\ Q_2^S \end{pmatrix} = \begin{bmatrix} Y_{11}^S & Y_{12}^S \\ Y_{21}^S & Y_{22}^S \end{bmatrix} \begin{bmatrix} \Phi_1^S \\ \Phi_2^S \end{bmatrix} = Y^S \begin{bmatrix} P_1^S \\ P_2^S \end{bmatrix} - Y^S \begin{bmatrix} \text{Þ}^S \\ \text{Þ}^S \end{bmatrix}$$

and similarly,

$$\boldsymbol{Q}^T = Y^T \boldsymbol{P}^T - Y^T \boldsymbol{\text{Þ}}^T.$$

Where, as before $Q_1 = Q_n(0)$, $Q_2 = -Q_n(L)$ for any Fourier mode n is the fluid flow (sign choice by convention), and similarly Φ_1, Φ_2 are transmural pressures at the proximal and distal ends of the tube, P_1, P_2 are fluid pressures, and Þ is an external pressure. The pressures are related to each other:

$$\Phi_i = P_i - \text{Þ}, \quad i = 1, 2.$$

Transmural and fluid pressure vary in space — hence the distinction between the inlet and out let of the tube — but we have assumed that external pressure is constant in space on the length scale of a single vessel. The superscript S or T simply indicates the vessels to which the given quantity refers. In general, we are interested in the admittance matrix when external pressure is allowed to vary between tubes, that is $\text{Þ}^S \neq \text{Þ}^T$. By allowing external pressure to vary between vessels within a structured tree, we can develop a theory for external pressures that need not be constant on a whole-organ scale.

We have the matching condition $P_2^S = P_1^T$, we simplify notation by dropping their suffixes, i.e. $P_2^S = P_1^T = P$. Further, we have $Q_2^S = -Q_1^T$.

Using the above systems of linear equations, we may write

$$Q_i^k = \left(\sum_{j=1}^{2} Y_{ij}^k P_j^k \right) - \text{Þ}^k \sum_{j=1}^{2} Y_{ij}^k \qquad i = 1, 2, \quad k = S, T. \tag{2.53}$$

Using the matching condition on the flows, we have

$$\begin{aligned} Q_2^S + Q_1^T &= 0 \\ &= Y_{21}^S P_1^S + Y_{22}^S P_2^S - \left(Y_{21}^S + Y_{22}^S\right) \text{Þ}^S \\ &\quad + Y_{11}^T P_1^T + Y_{12}^T P_2^T - \left(Y_{11}^T + Y_{12}^T\right) \text{Þ}^T, \\ P &= \frac{-\left(Y_{21} P_1^S + Y_{12}^T P_2^T\right) + \left(Y_{21}^S + Y_{22}^S\right) \text{Þ}^S + \left(Y_{11}^T + Y_{12}^T\right) \text{Þ}^T}{Y_{11}^T + Y_{22}^S} \\ &\equiv P_2^S = P_1^T. \end{aligned}$$

We then substitute this into the expressions the above expressions for Q_1^S and Q_2^T, and simplify the notation by dropping the suffixes S and T. We drop these suffixes from P_1^S and P_2^T as well.

$$\begin{aligned} Q_1 &= Y_{11}^S P_1 + Y_{12}^S P - \left(Y_{11}^S + Y_{12}^S\right) \text{Þ}^S \qquad (2.54) \\ &= \left(Y_{11}^S - \frac{Y_{21}^S Y_{12}^S}{Y_{11}^T + Y_{22}^S}\right) P_1 - \frac{Y_{12}^T Y_{12}^S}{Y_{11}^T + Y_{22}^S} P_2 + \left(\frac{\left(Y_{21}^S + Y_{22}^S\right)}{Y_{11}^T + Y_{22}^S} - \left(Y_{11}^S + Y_{12}^S\right)\right) \text{Þ}^S \\ &\quad + \frac{\left(Y_{11}^T + Y_{12}^T\right) Y_{12}^S}{Y_{11}^T + Y_{22}^S} \text{Þ}^T \end{aligned}$$

$$\begin{aligned} Q_2 &= Y_{21}^T P + Y_{22}^T P_2 - \left(Y_{21}^T + Y_{22}^T\right) \text{Þ}^T \qquad (2.55) \\ &= -\frac{Y_{21} Y_{21}^T}{Y_{11}^T + Y_{22}^S} P_1 + \left(Y_{22}^T - \frac{Y_{12}^T Y_{21}^T}{Y_{11}^T + Y_{22}^S}\right) P_2 + \frac{\left(Y_{21}^S + Y_{22}^S\right) Y_{21}^T}{Y_{11}^T + Y_{22}^S} \text{Þ}^S \\ &\quad + \left(\frac{\left(Y_{11}^T + Y_{12}^T\right) Y_{21}^T}{Y_{11}^T + Y_{22}^S} - \left(Y_{21}^T + Y_{22}^T\right)\right) \text{Þ}^T \end{aligned}$$

Taking these together gives

$$\boldsymbol{Q} = \frac{1}{Y_{11}^T + Y_{22}^S} \begin{bmatrix} Y_{11}^T Y_{11}^S + \det(Y^S) & -Y_{12}^T Y_{12}^S \\ -Y_{21} Y_{21}^T & Y_{22}^S Y_{22}^T + \det(Y^T) \end{bmatrix} \boldsymbol{P} + \begin{bmatrix} \frac{\left(Y_{21}^S + Y_{22}^S\right) Y_{21}^T}{Y_{11}^T + Y_{22}^S} - \left(Y_{11}^S + Y_{12}^S\right) & \frac{\left(Y_{11}^T + Y_{12}^T\right) Y_{12}^S}{Y_{11}^T + Y_{22}^S} \\ \frac{\left(Y_{21}^S + Y_{22}^S\right) Y_{21}^T}{Y_{11}^T + Y_{22}^S} & \frac{\left(Y_{11}^T + Y_{12}^T\right) Y_{21}^T}{Y_{11}^T + Y_{22}^S} - \left(Y_{21}^T + Y_{22}^T\right) \end{bmatrix} \begin{pmatrix} \text{Þ}^S \\ \text{Þ}^T \end{pmatrix},$$

$$\iff \boldsymbol{Q} = Y^{\Leftrightarrow} \boldsymbol{P} + Y^e \begin{pmatrix} \text{Þ}^S \\ \text{Þ}^T \end{pmatrix}, \tag{2.56}$$

where

$$Y^{\Leftrightarrow} = \frac{1}{Y_{11}^T + Y_{22}^S} \begin{bmatrix} Y_{11}^T Y_{11}^S + \det(Y^S) & -Y_{12}^T Y_{12}^S \\ -Y_{21} Y_{21}^T & Y_{22}^S Y_{22}^T + \det(Y^T) \end{bmatrix}, \tag{2.57}$$

$$Y^e = \begin{bmatrix} \frac{\left(Y_{21}^S + Y_{22}^S\right) Y_{21}^T}{Y_{11}^T + Y_{22}^S} - \left(Y_{11}^S + Y_{12}^S\right) & \frac{\left(Y_{11}^T + Y_{12}^T\right) Y_{12}^S}{Y_{11}^T + Y_{22}^S} \\ \frac{\left(Y_{21}^S + Y_{22}^S\right) Y_{21}^T}{Y_{11}^T + Y_{22}^S} & \frac{\left(Y_{11}^T + Y_{12}^T\right) Y_{21}^T}{Y_{11}^T + Y_{22}^S} - \left(Y_{21}^T + Y_{22}^T\right) \end{bmatrix}. \tag{2.58}$$

2.3.6 Recursive Algorithm and the Construction of a Structured Tree

The grand admittance is the admittance matrix for the whole structured tree — one matrix encodes the fluid pressure relation, and the second the external pressure relation. The grand admittance is the matching condition that joins a large artery-vein pair for a known external pressure. The outlet conditions of the large artery are the inlet conditions of the structured tree; the outlet conditions of the structured tree are the inlet conditions for the large vein.

Given that a structured tree model of an arterial or venous tree can be comprised of many hundreds of vessels segments, we must find a way to efficiently compute the grand admittance. We use a recursive algorithm that computes the fluid pressure and

external pressure admittance matrices in Fourier space, and employs a convolution integral to find the boundary condition in real space that is used to match the large artery-vein pair.

A structured tree is comprised of vessel segments joined together in series and parallel. A structured tree begins with a single vessel segment that arises from a terminal large artery. Suppose that a given parent vessel segment has unstressed radius r_p and length l_p, then its daughter vessels have radii r_{d_1} and r_{d_2}. The tree is self-similar – daughter vessels have lengths and radii that are constant fractions of those of the parent vessel. This fraction is a product of the dimensionless parameters α, β. Daughters in the α branch have radius αr_p, similarly for the β branch. We can label each vessel within the structured tree using powers of α, β. This is illustrated in Fig. 2.8. The vessel that has made i bifurcations in the α-branch and j bifurcations in the β-branch is (non-uniquely) labelled (i, j); the vessel (i, j) belongs to the $(i + j)$-th generation. The vessel (i, j) has unstressed radius $r_{(i,j)} = \alpha^i \beta^j r_p$ and length $l_{(i,j)} = \alpha^i \beta^j l_p$. The length of a vessel segment is a function of the length-to-radius ratio (l_{rr}) and the radius of the vessel; the l_{rr} varies between organ organ systems; establishing a value for l_{rr} is discussed in Chapter 4 and Chapter 5 for the pulmonary and coronary systems, respectively. The parameters α, β are determined using the branching and asymmetry parameters that will be seen in Chapter 4.

Qureshi [2, 3, 59] developed an efficient algorithm to find the grand admittance matrix in the absence of external pressure. I have modified this algorithm to compute the admittance including a time dependent external pressure. For simplicity, the same external pressure is applied to all vessels so is spatially homogenous. Details of the algorithm can be found in Appendix B. Essentially, it computes the admittance matrices (one each for the fluid and external pressure parts) for all vessels in the structured tree in Fourier space. For a tree with $n \in \mathbb{Z}_{>0}$ generations, the smallest

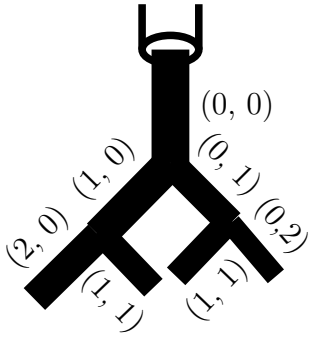

Figure 2.8: Cartoon showing the arterial side of a structured tree that has been truncated after the 2nd generation. The structured tree arises from a large artery. Here, bifurcations to the right are α bifurcations; left branches are β branches. In this example $\alpha = 0.9$, $\beta = 0.75$. The index pair (i, j) are given for each vessel in this tree.

vessels will have indices (i, j) such that $i + j = n$. Starting with the smallest vessels, pair-wise in series, join an artery with the vein that arises from it. Next, join arterial-venous pairs in parallel with those of the same generation; this forms a connection from the $(n - 1)$-th arterial and venous generation. In series, join the arteries in generation $(n - 1)$ with the downstream bed formed in the previous step and the analogous vein. Continue until there are no more vessels.

While an arterial tree is modelled by bifurcating branches of a structured tree, a venous one is modelled with coalescing branches. These two structured trees are joined in series with each other. As per the theory described in subsection 2.3.5, the arterial and venous trees both have associated admittance matrices. The grand admittance $\boldsymbol{Y}$ of a tree consisting of a arterial and venous tree joined in series is

given by

$$\begin{aligned}\boldsymbol{Y} = \boldsymbol{Y}^A(0,0) \iff \Big[&\left\{\boldsymbol{Y}^A(1,0)||\boldsymbol{Y}^A(0,1)\right\} \\ &\iff \left\{\boldsymbol{Y}^V(1,0)||\boldsymbol{Y}^V(0,1)\right\}\Big] \iff \boldsymbol{Y}^V(0,0).\end{aligned}$$

where $\iff$ indicates a join in series and $||$ a join in parallel; Y^A are admittance matrices for the arterial side, and Y^V are admittances for the venous side. The algorithm used to compute the grand admittance is given in App. B.

Once a grand admittance matrix has been obtained, we can use it to relate the fluid pressure and flow at the inlet $P^A(L)$, $Q^A(L)$ to the pressure and flow at the outlet $P^V(0)$, $Q^V(0)$ together with the external pressure at these points, denoted $\mathfrak{P}^A$, $\mathfrak{P}^V$ for the imposed arterial and venous pressure respectively, i.e.

$$\begin{pmatrix} Q^A(L) \\ Q^V(0) \end{pmatrix} = Y \begin{pmatrix} P^A(L) \\ P^V(0) \end{pmatrix} - Y^e \begin{pmatrix} \mathfrak{P}^A(L) \\ \mathfrak{P}^V(0) \end{pmatrix}. \tag{2.59}$$

This gives us the flows in terms of the pressures in Fourier space, which we relate to the real pressures and flows using the convolution product, convolution integral, and Fourier coefficients given in Sec. 2.3, specifically

$$\begin{aligned}q^A(L,t) = \frac{1}{T}\int_{-T/2}^{T/2} \Big[&\Big(p^A(L,t-\tau)y_{11}(\tau) + p^V(0,t-\tau)y_{12}(\tau)\Big) \\ &- \Big(\mathfrak{p}^A(t-\tau)y^e_{11}(\tau) + \mathfrak{p}^V(t-\tau)y^e_{12}(\tau)\Big)\Big]\,\mathrm{d}\tau,\end{aligned} \tag{2.60a}$$

$$\begin{aligned}q^V(0,t) = \frac{1}{T}\int_{-T/2}^{T/2} \Big[&\Big(p^A(L,t-\tau)y_{21}(\tau) + p^V(0,t-\tau)y_{22}(\tau)\Big) \\ &- \Big(\mathfrak{p}^A(t-\tau)y^e_{21}(\tau) + \mathfrak{p}^V(t-\tau)y^e_{22}(\tau)\Big)\Big]\,\mathrm{d}\tau.\end{aligned} \tag{2.60b}$$

In Section 3.2.4 we derive explicit boundary matching conditions that can be implemented numerically.

2.4 Chapter Summary

In this chapter we have specified the function for blood viscosity in small and large vessels. Viscosity in large vessels is constant, whereas in structured trees viscosity in any single vessel is constant but it is radius, so changes throughout the tree. There is a discontinuity between the published values for viscosity in large and small vessels. To reconcile this discrepancy, we scaled the function that gives small vessel with respect to the large vessel bulk viscosity value.

Then, beginning from the Navier–Stokes equations in cylindrical polar coordinates, and an incompressibility condition, we make a series of rational approximations to arrive at 1D equations for x-momentum balance and conservation of volume in large vessels. These two equations have three unknowns (A, q, ϕ), so we add a constitutive relation.

The derivation for flow in small vessels begins identically to that in large vessels. From a system of governing equations for small vessels, we to derive a boundary matching condition that allows us to link the flow and pressure at the terminus of an artery to the initus of a vein. The boundary matching conditions are expressed as a grand admittance matrix that relate in/out flow to in/out blood pressure and external pressure. Grand admittance matrices are computed via a recursion algorithm that takes matrices for single vessels, vessels joined in parallel, and vessels joined in series, together with constitutive and geometric parameters. The algorithm to find grand admittances works in Fourier space, so we use a convolution integral to find the real-space analogue for each structured tree.

The key contribution of this chapter is the novel and systematic inclusion of external pressure that is applied to both small and large vessels along their entire lengths. We are aware that Müller [31] and Mynard & Nithiarasu [34] derive similar large vessel models to ours and that the external pressure varies longitudinally in vessels in Müller's construction. We are, however, unaware of any 1D vascular bed model that includes external pressure. There are 0D lumped parameter models that include an *ad hoc* external pressure such as that of Clipp [33, 46, 47]. A fuller discussion of mathematical models for blood flow that include external pressure can be found in Chapter 1.

It is worth noting that, in practice, we use the radius-dependent viscosity in simulations of pulmonary flows but not for coronary flows. We do not use the radius dependent viscosity in coronary flows, as doing so leads to a convergence failure in the Newton-Raphson scheme used to find solutions to the model equations. The discussion of radius dependent viscosity is included here for completeness.

Chapter 3

Numerical Methods

In this chapter, I discuss the numerical methods, boundary conditions, and junction matching techniques that we use to simulate blood flow through a two-sided vascular network. This chapter begins with an overview of the computational scheme, before discussing specific numerical schemes, algorithms, and derivations. This chapter largely follows the work of Peskin, Olufsen, and Qureshi [3, 44, 69], but with key differences arising due to the inclusion of external pressure. The generalisation of large vessel junctions was done in collaboration with Dr. Mitchel Colebank (University of California, Irvine) and Prof. Mette Olufsen (North Carolina State University).

3.1 An Overview of the Computational Scheme

We have written down equations for blood flow and pressure in terms of vessel area in a large blood vessel that is subject to some external pressure. Further, we have developed an average description of fluid dynamic behaviour within a vascular bed via a structured tree approach. Now, I discuss the development and implementation

of the computational scheme. I begin with the computational scheme for blood flow in a single vessel of finite length, then moving onto the initial and boundary conditions that are applied in the model.

When working with the scheme, one specifies a network comprised of large arteries and veins. Each vessel has a unique index, length and radius, as well as vessels that are joined to it's distal end. The vessels are also all sorted into one of the four following types:

- inlet arteries,
- arteries or veins arising from a bifurcation,
- terminal arteries to be match to veins,
- terminal veins.

We supply initial conditions of either a fluid pressure or fluid flow profile and external pressure profile(s). The initial conditions are applied at the proximal end ($x = 0$) of the inlet arteries. If flow is supplied as the initial condition, we compute vessel area for all time $t \in [0, T]$ and pressure; if pressure is supplied, we compute flow then area. Once q, p, A are known for all time t at $x = 0$, we move onto the next spatial point in the inlet arteries. Continue like this until the end(s) of the inlet arteries are reached.

The inlet arteries then branch to form further arteries; the distal flow and pressure of the inlet artery are used to compute the proximal flow and pressure for the daughter arteries, and the scheme finds flow, pressure, and area at all grid points in the daughters. Daughter vessels can then either branch to form more arteries, or they can be joined to a vein via a structured tree.

As discussed previously, a structured tree can be thought of as an average description of a vascular bed, and we have written down equations that relate the proximal flow and pressure to the distal flow and pressure. The distal flow and pressure in a structured tree are supplied by the terminal artery from whence it arises, and the grand admittance relates this to flow and pressure at the distal end of a vein. Computation of flow and pressure in each vein proceeds exactly as it does in arteries.

Veins arising from the structured tree can either coalesce to form larger veins, or can be treated as an outlet vessel. Coalescing vessels are treated like bifurcating vessels. In outlet veins, we apply the outlet boundary condition in the end furthest from the structured tree. The outlet boundary condition is usually a static pressure, but could easily be modified to be a time dependent pressure or flow profile.

3.2 Methods for Large Vessels

The system (2.8, 2.22, 2.23) cannot be solved analytically in the computational domain representing a vascular network, so we must solve it numerically. To do this, we use a two-step Lax–Wendroff method. We use a Lax–Wendroff method as this is a standard tool for solving hyperbolic systems, is relatively straight forward to implement, is second-order accurate in time and space, and is computationally efficient. In order to apply this method, we write the model equations in conservative form.

We begin by considering $A(x,t) \equiv \hat{A}(\varphi(x,t), r_0(x))$, where A, $\hat{A}$ are vessel lumen area, φ is transmural pressure, r_0 is the reference lumen radius, x denotes the longitudinal direction, and t is time. Unless otherwise specified, a hat $\hat{}$ indicates a dependence on one or more of φ, r_0, and its absence indicates dependence on one or

more of x, t. In order to write (2.22) in conservation form, we define

$$\begin{aligned}\hat{B}(\varphi, r_0) &= \int_{p_0}^{\varphi} \hat{A}(p^*, r_0)|_{r_0}\, \mathrm{d}p^* = \frac{\hat{f}}{3\sqrt{A_0}}\left([\hat{A}]^{3/2} - A_0^{3/2}\right) \\ &\equiv \frac{f}{3\sqrt{A_0}}\left([A]^{3/2} - A_0^{3/2}\right) = B(x,t)\end{aligned} \tag{3.1}$$

Details of this integration can be found in App. A.

In the following, the notation $\left.\dfrac{\partial\gamma}{\partial\xi}\right|_{\zeta}$ means a partial derivative of γ with respect to ξ that we evaluate at a fixed value of ζ.

Using the definition of B, we can rewrite (2.22) as

$$\frac{\partial q}{\partial t} + \frac{\partial}{\partial x}\left(\frac{q^2}{A} + B\right) = -\frac{2\pi R}{\delta\mathcal{R}}\frac{q}{A} - \left.\frac{\partial\hat{B}}{\partial r_0}\right|_{\varphi}\frac{\mathrm{d}r_0}{\mathrm{d}x} \tag{3.2}$$

where $\mathcal{R}$ is the Reynolds' number as defined in Subsection 2.2.2. Further,

$$\begin{aligned}\left.\frac{\partial B}{\partial x}\right|_t &= \left.\frac{\partial\hat{B}}{\partial r_0}\right|_{\varphi}\frac{\mathrm{d}r_0}{\mathrm{d}x} + \left.\frac{\partial\hat{B}}{\partial\varphi}\right|_{r_0}\left.\frac{\partial\varphi}{\partial x}\right|_t \\ &= \left.\frac{\partial\hat{B}}{\partial r_0}\right|_{\varphi}\frac{\mathrm{d}r_0}{\mathrm{d}x} + \left.\frac{\partial\hat{B}}{\partial\varphi}\right|_{r_0}\left.\frac{\partial p}{\partial x}\right|_t,\end{aligned} \tag{3.3}$$

further details of which can be found in Appendix A.

We can express the system (2.8, 3.2) in conservation form

$$\frac{\partial}{\partial t}\boldsymbol{U} + \frac{\partial}{\partial x}\boldsymbol{W} = \boldsymbol{S}, \tag{3.4}$$

where

$$\boldsymbol{U} = \begin{pmatrix} A \\ q \end{pmatrix} = \begin{pmatrix} U_1 \\ U_2 \end{pmatrix}, \tag{3.5a}$$

$$\boldsymbol{W} = \begin{pmatrix} q \\ \frac{q^2}{A} + B \end{pmatrix} = \begin{pmatrix} W_1 \\ W_2 \end{pmatrix}, \tag{3.5b}$$

$$\boldsymbol{S} = \begin{pmatrix} 0 \\ -\dfrac{2\pi R}{\delta \mathcal{R}} \dfrac{q}{A} - \left.\dfrac{\partial \hat{B}}{\partial r_0}\right|_{\varphi} \dfrac{\mathrm{d}r_0}{\mathrm{d}x} \end{pmatrix} = \begin{pmatrix} S_1 \\ S_2 \end{pmatrix}. \tag{3.5c}$$

3.2.1 Richtmeyer's two-step Lax–Wendroff scheme

We wish to derive a system of difference equations which are satisfied by smooth solutions of (3.4) up to terms of second order in spatial and temporal steps, Δx and Δt. There is no possibility of shock formation as the wavelength of the pressure pulse from the heart is much greater than the length scale of a vessel. These constitute Richtmeyer's two-stop Lax–Wendroff scheme. To do this, we follow Peskin [69].

Let $\mathbf{U}_m^n = \mathbf{U}(m\Delta x, n\Delta t)$, similarly for $\mathbf{W}$ and $\mathbf{S}$, where $m \in [0, M],\ n \in [0, N]$. Here, M is number of distinct spatial points, and N is the number of time points. We require expressions for derivatives of $\mathbf{U}$, $\mathbf{W}$, $\mathbf{S}$ with respect to x, t. These come from an application of Taylor's Theorem as follows:

$$\boldsymbol{U}_{m\pm1}^n = \boldsymbol{U}_m^n \pm \Delta x (\boldsymbol{U}_x)_m^n + \frac{\Delta x^2}{2}(\boldsymbol{U}_{xx})_m^n \pm \frac{\Delta x^3}{6}(\boldsymbol{U}_{xxx})_m^n + \mathcal{O}(\Delta x^4). \tag{3.6}$$

Here, the subscript x indicates partial differentiation with respect to x. A similar result holds for a Taylor's series in t, and for $\mathbf{W}$ and $\mathbf{S}$. Adding and subtracting these we obtain

$$\begin{aligned} \boldsymbol{U}_{m+1}^n + \boldsymbol{U}_{m-1}^n &= 2\boldsymbol{U}_m^n + \Delta x^2 (\boldsymbol{U}_{xx})_m^n + \mathcal{O}(\Delta x^4), \\ \boldsymbol{U}_{m+1}^n - \boldsymbol{U}_{m-1}^n &= 2\Delta x (\boldsymbol{U}_x)_m^n + \mathcal{O}(\Delta x^3). \end{aligned} \tag{3.7}$$

Consequences of this include

$$\begin{aligned}
\boldsymbol{U}_m^n &= \frac{1}{2}\left(\boldsymbol{U}_{m-1}^n + \boldsymbol{U}_{m+1}^n\right) + \mathcal{O}(\Delta x^2), \\
\frac{\boldsymbol{U}_{m+1}^n - \boldsymbol{U}_{m-1}^n}{2\Delta x} &= (\boldsymbol{U}_x)_m^n + \mathcal{O}(\Delta x^2) \\
\frac{\boldsymbol{U}_{m+1}^n + \boldsymbol{U}_{m-1}^n - 2\boldsymbol{U}_m^n}{\Delta x^2} &= (\boldsymbol{U}_{xx})_m^n + \mathcal{O}(\Delta x^2)
\end{aligned} \tag{3.8}$$

which are all second order accurate due to symmetry. It is straightforward to write down equivalent results for derivates of $\mathbf{V}$ and $\mathbf{W}$ with respect to x and t.

Consider

$$\frac{\boldsymbol{U}_m^{n+1} - \boldsymbol{U}_m^n}{\Delta t} = \boldsymbol{S}_m^{n+1/2} - (\boldsymbol{W}_x)_m^{n+1/2} + \mathcal{O}(\Delta t^2)$$

which is the difference equation analogue of (3.4). We must approximate the right hand side, but for this approximation to be useful, it should be constructed from the values of $\boldsymbol{U}$ at time level n.

Before we do this, it is useful to note that

$$\boldsymbol{U}_{m+1/2}^{n+1/2} = \boldsymbol{U}_{m+1/2}^n + \frac{\Delta t}{2}(\boldsymbol{U}_t)_{m+1/2}^n + \mathcal{O}(\Delta t^2), \tag{3.9a}$$

$$\boldsymbol{U}_{m+1/2}^n = \frac{1}{2}\left(\boldsymbol{U}_{m+1/2}^n + \boldsymbol{U}_m^n\right) + \mathcal{O}(\Delta x^2), \tag{3.9b}$$

and by (3.4)

$$(\boldsymbol{U}_t)_{m+1/2}^n = (-\boldsymbol{W}_x)_{m+1/2}^n + \boldsymbol{S}_{m+1/2}^n + \mathcal{O}(\Delta x^2). \tag{3.10}$$

Using (3.9b), (3.10), (3.9a) becomes

$$\boldsymbol{U}_{m+1/2}^{n+1/2} = \frac{1}{2}\left(\boldsymbol{U}_{m+1}^n + \boldsymbol{U}_m^n\right) + \frac{\Delta t}{2}\left[\frac{\boldsymbol{S}_{m+1}^n + \boldsymbol{S}_m^n}{2} - \frac{\boldsymbol{W}_{m+1}^n - \boldsymbol{W}_m^n}{\Delta x}\right] + \mathcal{O}(\Delta x^2 + \Delta t^2). \tag{3.11}$$

Now, define a function $\tilde{\boldsymbol{U}}$ such that

$$\boldsymbol{U}_{m+1/2}^{n+1/2} = \tilde{\boldsymbol{U}}_{m+1/2}^{n+1/2} + \mathcal{O}(\Delta x^2 + \Delta t^2)$$

for theoretical purposes, $\tilde{\boldsymbol{U}}$ is required to hold for all values of m, n, not just integeral values. This is a smooth function over the whole (x,t)-plane. It is easy to show that a corresponding relationship holds for $\boldsymbol{U}_x$ & $\tilde{\boldsymbol{U}}_x$, $\boldsymbol{W}$ & $\tilde{\boldsymbol{W}}$, $\boldsymbol{W}_x$ & $\tilde{\boldsymbol{W}}_x$, and $\boldsymbol{S}$ & $\tilde{\boldsymbol{S}}$ bearing in mind that $\boldsymbol{S}$ & $\boldsymbol{W}$ are functions of $\boldsymbol{U}$, so $\tilde{\boldsymbol{S}}$ & $\tilde{\boldsymbol{W}}$ are functions of $\tilde{\boldsymbol{U}}$.

Richtmeyer's two-step version of the Lax–Wendroff method comes from dropping the higher order terms encoded in $\mathcal{O}(\Delta x^2 + \Delta t^2)$. That is, we work with only $\tilde{\boldsymbol{S}}$, $\tilde{\boldsymbol{W}}$, and $\tilde{\boldsymbol{U}}$. For ease of notation, we drop the tildes. Until now, the scheme has represented an exact solution of (3.4); this is no longer the case.

From (3.11), we can see that

$$2\boldsymbol{U}_m^{n+1} = \left(\boldsymbol{U}_{m+1/2}^{n+1/2} + \boldsymbol{U}_{m-1/2}^{n+1/2}\right) + \Delta t \left[\frac{\boldsymbol{S}_{m+1/2}^{n+1/2} + \boldsymbol{S}_{m-1/2}^{n+1/2}}{2} - \frac{\boldsymbol{W}_{m+1/2}^{n+1/2} - \boldsymbol{W}_{m-1/2}^{n+1/2}}{\Delta x}\right]. \quad (3.12)$$

By construction

$$\boldsymbol{U}_m^{n+1/2} = \frac{\boldsymbol{U}_{m+1/2}^{n+1/2} + \boldsymbol{U}_{m-1/2}^{n+1/2}}{2} = \frac{\boldsymbol{U}_m^{n+1} + \boldsymbol{U}_m^n}{2},$$

so we can rewrite (3.12) as

$$\boldsymbol{U}_m^{n+1} = \boldsymbol{U}_m^n + \frac{\Delta t}{2}\left[\boldsymbol{S}_{m+1/2}^{n+1/2} + \boldsymbol{S}_{m-1/2}^{n+1/2}\right] - \frac{\Delta t}{\Delta x}\left[\boldsymbol{W}_{m+1/2}^{n+1/2} - \boldsymbol{W}_{m-1/2}^{n+1/2}\right] \quad (3.13)$$

a four point formula that predicts flow at the next time level $n+1$, given flow at all space levels in time level n. It is suitable for recursively finding the second-order accurate solution for $\boldsymbol{U}$ given initial data.

Further, we need to be able to determine

$$\boldsymbol{W}_{m\pm1/2}^{n+1/2}, \boldsymbol{S}_{m\pm1/2}^{n+1/2}$$

given their original definitions and the following consequence of (3.11)

$$\boldsymbol{U}_j^{n+1/2} = \frac{1}{2}\left(\boldsymbol{U}_{j+1/2}^n + \boldsymbol{U}_{j-1/2}^n\right) + \frac{\Delta t}{2}\left[\frac{\boldsymbol{S}_{j+1/2}^n + \boldsymbol{S}_{j-1/2}^n}{2} - \frac{\boldsymbol{W}_{j+1/2}^n - \boldsymbol{W}_{j-1/2}^n}{\Delta x}\right] \quad (3.14)$$

in which $j = m \pm 1/2$.

As $\boldsymbol{W}$ and $\boldsymbol{S}$ are functions of $\boldsymbol{U}$, if we can determine $\boldsymbol{U}$ at any point spatial or temporal point in the computational domain, then we can find $\boldsymbol{W}$ and $\boldsymbol{S}$ at all of those points.

3.2.2 Pressure as an Inlet Boundary Condition

Using a two-step Lax–Wendroff scheme it is possible to use any of flow, fluid pressure, or vessel area as the inlet condition. Vessel area in the current configuration can be written as a function of transmural pressure. Fluid pressure $p(0,t)$ and external pressure $\text{þ}(t)$ are prescribed for all time t, so it is straightforward to find the transmural pressure $\varphi(0,t)$ and hence area $A(\varphi(0,t))$ at the inlet. We determine flow $q(0,t)$ using (3.13), (3.5c), and (3.5b). For completeness, mathematical details can be found in App. A.2

3.2.3 Vessel-Junction Matching Conditions

There are a number of variations on typical vascular anatomy that cannot be captured by a bifurcating tree, such as stenoses due to coronary artery disease [89] or in the pulmonary circulatory system [90], and tri- [91] and quadfurcations [92]. In all these cases, it would be useful to be able to capture different branching patterns with this model. To do this, I examine the existing boundary condition and extend it to any number of daughter vessels. A vessel stenosis could be modelled using two subsequent junctions with a one parent and daughter each as pictured in Fig. 3.1a.

To deal with vessel stenoses, tri-, and quadfurcations, we examine the bifurcation matching condition presented by Olufsen [44] and generalise to give a matching condition between a single parent and $r \in \mathbb{Z}_{\geq 1}$ daughter vessels. Such a junction is

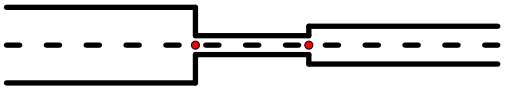

(a) Two subsequent junctions of $r = 1$ can be used to model vessel stenosis. The red circles represent the points at which the matching condition is applied.

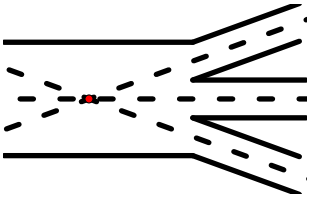

(b) A cartoon of an even trifurcation with trifurcation point (on the intersection of the dashed mid-lines of the vessels) marked with a filled red circle.

Figure 3.1: Cartoon vessel junctions for $r = 1$ and $r = 3$.

called an "r-furcation". This can also be extended to join converging vessels.

As with bifurcations, we need to match fluid pressure and flow at the boundary between the parent and daughter vessels. This amounts to imposing

$$p_p(L,t) = p_{d_i}(0,t),\ \forall i = 1,2,...,r, \tag{3.15}$$

$$q_p(L,t) = \sum_{i=1}^{r} q_{d_i}(0,t) \tag{3.16}$$

at the outlet of a parent vessel of length L (at $x = L = M\Delta x$) with fluid pressure p_p and flow q_p and inlet ($x = 0$) of daughter vessels with fluid pressure p_{d_i} for the i-th daughter and flow q_{d_i}. In discretised time and space, we write this matching condition as

$$(f_p)_M \left(\sqrt{\frac{(A_p)_M^j}{\left((A_0)_p\right)_M}} - 1 \right) + \text{Þ}_p{}^j = (f_{d_i})_0 \left(\sqrt{\frac{(A_{d_i})_0^j}{\left((A_0)_{d_i}\right)_0}} - 1 \right) + \text{Þ}_{d_1}{}^j, \tag{3.17a}$$

$$(q_p)_M^j = \sum_{i=1}^{r} (q_{d_i})_0^j \,. \tag{3.17b}$$

for some time $j\Delta t$ s and for all $i = 1,2,...,r$ using the constitutive relation (2.23). The external pressure applied to the parent vessel is Þ_p and Þ_{d_i} is the external pressure

applied to the i-th daughter vessel.

The flow and pressure boundary conditions at the next time step are given by evaluating (3.17) at $j = n + 1$. This yields a system of $r + 1$ equations and $2(r + 1)$ unknowns $(A_p)_M^{n+1}$, $(q_p)_M^{n+1}$, $(A_{d_i})_M^{n+1}$, $(q_{d_i})_M^{n+1}$.

Using the four-point formula (3.13) and the definitions (3.5a, 3.5b, 3.5c), we predict flow and current area at time $n + 1$

$$A_M^{n+1} = A_M^n - \frac{\Delta x}{\Delta t}\left(\left((W_1)_{d_i}\right)_{\mathcal{M}+1/2}^{n+1/2} - \left((W_1)_{d_i}\right)_{\mathcal{M}-1/2}^{n+1/2}\right) \tag{3.18a}$$

$$\begin{aligned} q_M^{n+1} = q_M^n &- \frac{\Delta x}{\Delta t}\left(\left((W_2)_{d_i}\right)_{\mathcal{M}+1/2}^{n+1/2} - \left((W_2)_{d_i}\right)_{\mathcal{M}-1/2}^{n+1/2}\right) \\ &+ \frac{\Delta t}{2}\left(\left((S_2)_p\right)_{\mathcal{M}+1/2}^{n+1/2} + \left((S_2)_p\right)_{\mathcal{M}-1/2}^{n+1/2}\right) \end{aligned} \tag{3.18b}$$

$i = 0, ..., r$, in which $i = 0$ indicates a parent vessel, and $i \neq 0$ the i-th daughter. When $i = 0$, $\mathcal{M} = M$ and $\mathcal{M} = 0$ otherwise. Doing so adds $2(r + 1)$ equations to the system and $3(r + 1)$ unknowns $((W_1)_{d_i})_{\mathcal{M}+1/2}^{n+1/2}$, $((W_2)_{d_i})_{\mathcal{M}+1/2}^{n+1/2}$, $((S_2)_{d_i})_{\mathcal{M}+1/2}^{n+1/2}$ for $i = 0, ..., r$.

To find these unknowns, we introduce ghost-points a full spatial-step behind the point at which we wish to evaluate (see Fig. 3.2)

$$(A_{d_i})_{\mathcal{M}}^{n+1/2} = \frac{1}{2}\left((A_{d_i})_{\mathcal{M}-1/2}^{n+1/2} + (A_{d_i})_{\mathcal{M}+1/2}^{n+1/2}\right), \tag{3.19a}$$

$$(q_{d_i})_{\mathcal{M}}^{n+1/2} = \frac{1}{2}\left((q_{d_i})_{\mathcal{M}-1/2}^{n+1/2} + (q_{d_i})_{\mathcal{M}+1/2}^{n+1/2}\right), \tag{3.19b}$$

as $\boldsymbol{W}$, $\boldsymbol{S}$ are functions of A, q. Introducing the ghost-points has added $2(r + 1)$ equations and $2(r + 1)$ unknowns $(A_{d_i})_{\mathcal{M}}^{n+1/2}$, $(A_{d_i})_{\mathcal{M}}^{n+1/2}$, $i = 0, ..., r$. All of the unknowns $\boldsymbol{W}_{\mathcal{M}+1/2}^{n+1/2}$, $\boldsymbol{S}_{\mathcal{M}+1/2}^{n+1/2}$ are now known.

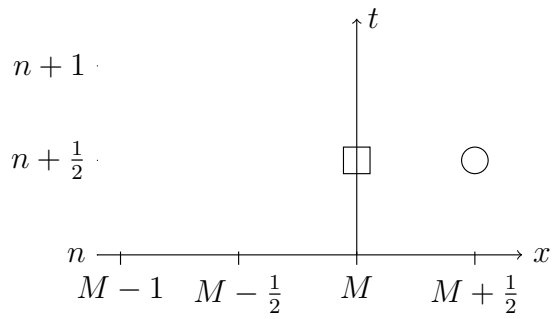

Figure 3.2: The ghost point marked with a circle (∘) is a *half step after* the outlet of a vessel. Points marked with a cross (×) are known. The point marked with a box (□) is found by averaging between adjacent time steps.

There are $6(r+1)$ unknowns

$$\begin{aligned} &x_{3i+1} = (q_{d_i})^{n+1}_{\mathcal{M}}\,, && x_{3i+2} = (q_{d_i})^{n+1/2}_{\mathcal{M}}\,, && x_{3i+3} = (q_{d_i})^{n+1/2}_{\mathcal{M}-1/2}\,, \\ &x_{3(i+r+1)+1} = (A_{d_i})^{n+1}_{\mathcal{M}}\,, && x_{3(i+r+1)+2} = (A_{d_i})^{n+1/2}_{\mathcal{M}}\,, && x_{3(i+r+2)} = (A_{d_i})^{n+1/2}_{\mathcal{M}-1/2}\,, \end{aligned} \tag{3.20}$$

for $i = 0, 1, ..., r$. However, the system (3.17) at $j = n+1$, (3.18) and (3.19) for $i = 0, ..., r$ is comprised of only $5(r+1)$ equations. Evaluating the discretised boundary condition (3.17) at $n + 1/2$ adds a further $r+1$ equations without introducing any additional unknowns. The system of equations is now well-determined.

At the grid points $(L, n+1)$, $(L, n+\frac{1}{2})$, $(L+\frac{1}{2}, n+\frac{1}{2})$, and $(0, n+1)$, $(0, n+\frac{1}{2})$, $(\frac{1}{2}, n+\frac{1}{2})$, each of (3.17), (3.18), (3.19) can be expressed as a residual $g_i(\boldsymbol{x}) = 0$, $i = 1, ..., 6(r+1)$. These are listed App. A.3.1. The functions g_i form the rows of a vector of residuals $\boldsymbol{g}(\boldsymbol{x})$.

At each time step, n, the system can be solved to estimate $\boldsymbol{x} = \big(x_1, x_2, ..., x_{6(r+1)}\big)$ by using Newton's method which solves $\boldsymbol{g}(\boldsymbol{x}_i) = \boldsymbol{0}$ by extending the tangent line at the i-th guess for the root $\boldsymbol{x}_i$ until it crosses zero. The next guess $\boldsymbol{x}_{i+1}$ is set to be

the abscissa of that zero-crossing, i.e. $|\boldsymbol{x}_i|$. Algebraically, based on the first order expansion of Taylor's series in the neighbourhood of a point x_i, the method gives

$$(x_i)_j = (x_i)_{j-1} - \left(\frac{\mathrm{d}g\left((x_i)_{j-1}\right)}{\mathrm{d}\,(x_i)_{j-1}} \right)^{-1} g\left((x_i)_{j-1}\right)$$

where the index $i \in [1, 2, ..., 6(r+1)]$ tracks the unknown being estimated, and $j = 1, 2, ...$ represents the number of iterations. Continue iterating until the error meets a tolerance condition

$$\left| g\left((x_i)_j\right) - g\left((x_i)_{j-1}\right) \right| < \epsilon,$$

or some maximum number of iterations is surpassed, in which case the computational scheme returns an error. This method only works for non-zero gradients with appropriate initial guesses $(x_i)_0$ for each x_i, $i = 1, 2, ..., r$. Thus, we have

$$\boldsymbol{x}_j = \boldsymbol{x}_{j-1} \left(D\boldsymbol{g}(\boldsymbol{x}_{j-1}) \right)^{-1} \boldsymbol{g}(\boldsymbol{x}_{j-1}) \tag{3.21}$$

from which we define the Jacobian $J := D\boldsymbol{g}(\boldsymbol{x})$. We seek analytic expressions for J, its determinant $\det J$ and its inverse J^{-1} for a given number of daughter vessels r.

The Jacobian

The Jacobian J has a predictable structure, regardless of the number of daughter vessels. I devised Alg. 1 to produce the Jacobian $J \in \mathbb{R}^{6(r+1)\times 6(r+1)}$ used to match the boundary between a single parent vessel and r daughters. The algorithm to produce J is given in terms of the elements of the vector $\boldsymbol{\chi} = [\chi_1, ..., \chi_{4+4r}]$, the rows of this vector are functions. By definition, the elements of J are derivatives of $\boldsymbol{g}$ with respect to $\boldsymbol{x}$, and hence so are the elements of $\boldsymbol{\chi}$. Implementing the algorithm to produce the Jacobian is straightforward using a modern computer algebra system,

as is finding the unknowns and residuals for given r, and hence finding the functions $\boldsymbol{\chi}$.

In order to match vessels together over a junction, we require J^{-1} once per time step per junction. Numerically inverting J can be computationally expensive and give rise to numerical rounding errors. Instead of finding J^{-1} numerically, we use a computer algebra package to invert J before including it in the computational scheme, skipping the matrix inversion step and increasing the robustness of the scheme.

3.2.4 Arterial-Venous Boundary Matching Condition

Matching the boundary between an arterial-venous pair using the structured tree is very similar the junction matching for a single daughter. However, instead of requiring continuity of fluid pressure, we use the structured tree boundary condition seen in Chapter 2.

The boundary matching scheme presented in this section is adapted from that of Vaughan [29] to include the impact of external pressure. In general, we join an artery of length L^A to a vein of length L^V. By convention, the arterial and venous trees are built from the outside in: from the inlet (arteries) or outlet (veins) towards the structured tree. Because of this convention, we join the $x = L^A$ end of an artery to the $x = L^V$ end of a vein.

To use it in the computational scheme, we must discretise the convolution integral (2.60) that links flow flow and transmural pressure as

$$\begin{aligned}\left(q^A\right)^n_{M^A} = \Bigg(&\left(p^A\right)^n_{M^A}\left(y_{11}\right)^0 + \left(p^V\right)^n_{M^V}\left(y_{12}\right)^0 - \left[\left(\mathfrak{p}^A\right)^n\left(y^e{}_{11}\right)^0 + \left(\mathfrak{p}^V\right)^n\left(y^e{}_{12}\right)^0\right] \\ &+ \sum_{k=1}^{N-1}\left[\left(p^A\right)^{\langle n-k\rangle_N}_{M^A}\left(y_{11}\right)^k + \left(p^V\right)^{\langle n-k\rangle_N}_{M^V}\left(y_{12}\right)^k - \left[\left(\mathfrak{p}^A\right)^{\langle n-k\rangle_N}\left(y^e{}_{11}\right)^k + \left(\mathfrak{p}^V\right)^{\langle n-k\rangle_N}\left(y^e{}_{12}\right)^k\right]\right]\Bigg)\Delta t,\end{aligned} \tag{3.22a}$$

Algorithm 1: An algorithm to produce the junction-matching Jacobian for a given number of daughter vessels r.

Result: The Jacobian, $J \in \mathbb{R}^{6(r+1)\times 6(r+1)}$;

Input: Integer r;

Let $k = 1$;

for ($\boldsymbol{i}$ from **1 to** $\boldsymbol{r+1}$ in steps of 1)
- $J(i, 3i-2) = -1$;
- $J(i, 3i) = \chi_k; k = k+1$;
- $J(i, 3(i+r+1)) = \chi_k$; $k = k+1$;

$J(r+2, 3(r+1)+1) = -1$;

$J(r+2, 3) = -\frac{\Delta t}{\Delta x}$;

for ($\boldsymbol{i}$ from **1 to** $\boldsymbol{r}$ in steps of 1)
- $J(r+2+i, 3(i+1)) = \frac{\Delta t}{\Delta x}$;
- $J(r+2+i, 3(i+r)+4) = -1$;
- $J(4(r+1)+1, 3i+2) = 1$;
- $J(4(r+1)+2, 3i+1) = 1$;
- $J(4(r+1)+2+i, 3(r+1)+2) = \chi_k$;
- $J(5(r+1)+1+i, 3(r+1)+1) = \chi_{k+r+1}$;

$k = k+1$;

for ($\boldsymbol{i}$ from **1 to** $\boldsymbol{2(r+1)}$ in steps of 1)
- $J(i+2(r+1), 3i-1) = -1$;
- $J(i+2(r+1), 3i) = \frac{1}{2}$;

$J(4(r+1)+1, 2) = -1$;

$J(4(r+1)+2, 1) = -1$;

for ($\boldsymbol{i}$ from **1 to** $\boldsymbol{r}$ in steps of 1)
- $J(4(r+1)+2+i, 3(i+r+1)+2) = \chi_k$;
- $J(5(r+1)+1+i, 3(i+r+1)+1) = \chi_{k+r+1}$;
- $k = k+1$;

$$\left(q^V\right)^n_{M^V} = \Bigg(\left(p^A\right)^n_{M^A} \left(y_{21}\right)^0 + \left(p^V\right)^n_{M^V} \left(y_{22}\right)^0 - \left(\text{Þ}^A\right)^n \left(y^e{}_{21}\right)^0 - \left(\text{Þ}^V\right)^n \left(y^e{}_{22}\right)^0 \quad (3.22b)$$
$$+ \sum_{k=1}^{N-1} \left[(p^A)^{\langle n-k\rangle_N}_{M^A} (y_{11})^k + (p^V)^{\langle n-k\rangle_N}_{M^V} (y_{12})^k - (\text{Þ}^A)^{\langle n-k\rangle_N} (y^e{}_{11})^k - (\text{Þ}^V)^{\langle n-k\rangle_N} (y^e{}_{12})^k \right] \Bigg) \Delta t.$$

Here, $n \in [0, N]$ is the current time step, and $\langle\cdot\rangle_N$ is the modulo operator whose output is integers in the range $[0, N-1]$.

Full details of the system of equations to solve, the unknowns, the residual equations, and the Jacobian J can be found in App. A.4. The analysis proceeds similarly to that for the junction matching.

3.2.5 Outlet Pressure Based Boundary Condition

Similarly to the inlet boundary condition, this does not differ from the version presented by Qureshi [3]. For completeness, details can be found in A.6.

3.3 Summary

In this chapter, I give an overview of the model code before discussing the derivation and implementation of the numerical methods required to simulate blood flow and pressure in a two-sided network that is subject to some external pressure.

Much of the contents of this chapter builds upon the work of others: the Lax–Wendroff scheme used here was originally presented by Peskin [69], Peskin also originally suggested the extension of Olufsen's [44] structured tree matching condition that allows us to join the arterial and venous sides together, this extension was derived and implemented by Vaughan [29]. The pressure-based inlet boundary condition was derived and implemented by Qureshi [3].

I extended the Lax–Wendroff scheme and boundary matching conditions to include a time-dependent external pressure applied to small and large vessels. I implemented the relevant changes in the model code, then generalising the vessel branching condition that allows us include vessel stenosis and one-to-many junctions (such as tri- and quadfurcations). To the best of our knowledge, there is little literature that deals with such branching in 1D flow models, and none that generalise the junction matching condition in the same way as is done in this chapter. Finally, I discuss matching the large arterial and venous sides via a structured tree in which all vessels are subject to some external pressure.

The generalisation from a bifurcation matching condition to a junction matching condition represents an important step toward patient specific flow modelling, as many vessel networks exhibit trifurcations or stenosis. To the best of our knowledge, there are no other studies that generalise vessel branching to allow an arbitrary number of daughter vessels. To the best of our knowledge, the only study that includes 1D arterial or venous trifurcations is that of Mynard and Nithiarasu [34], who do not discuss their boundary matching scheme in detail. In their studies of 1D coronary flow Zheng and colleagues [49, 93] model trifurcations via two bifurcations in quick succession. Choi *et al.* [94] model 1D airflow in the human lung using incompressible isothermal energy balance equations which they solve using a GMRES; they do include bifurcations and trifurcations in their networks, but with significantly different model equations and boundary conditions to those found here.

The key shortcomings of the work presented in this chapter arise from the assumption of spatially homogeneous external pressure. We are able to specify different external pressures to adjacent vessels which may lead to high-gradient jumps in fluid or transmural pressure which is non-physical; a potential area of future research is the "smoothing" of these external pressure discontinuities, where there is a grad-

ual change along the length of a vessel to eliminate sudden jumps over junctions or the structured tree. The pressure applied to the structured tree is also spatially homogenous; it may be straight-forward to introduce radius-dependence to the pressure applied to structured trees, perhaps better capturing the dynamics of an organ in which greater pressure are applied deep within the tissue, and vessels get smaller with depth.

Chapter 4

Model Validation and Pulmonary Simulations

In this chapter, I demonstrate the impact made by applying an external pressure on vessels in the two-sided network. To do so, I present a number of simulations within toy networks under a few different scenarios. The simulation results are self consistent and give intuitively reasonable results. Following this, I simulate blood flow in a physiologically realistic pulmonary network, and show that the changes in blood flow predicted by the model are in line with those seen in the literature.

4.1 Parameter choices

Minimum radius The minimum lumen radius permissible in a structured tree. This should be set between approximately 10 µm and 100 µm. The smallest capillaries have radius 4 µm [5], so r_{min} must be greater than the radius of the smallest capillaries. Olufsen [44] notes that r_{min} determines the overall resistance to flow of

the structured tree and should be chosen for each organ or tissue in which we are modelling. Further, it must be chosen carefully as simulations are highly sensitive to changes in r_{min} [44, 79]. Vaughan showed that the choice of r_{min} is an important determinant of mean arterial pressure; increasing r_{min} can be simulate microvascular rarefaction and is an important predictor of hypertension. In his model for the pulmonary circulation, Qureshi sets 50µm [3]. In toy simulations, I use $r_{min} = 100\,\mu\text{m}$ in order to reduce computational time. For physiologically realistic simulations, I use $r_{min} = 25\,\mu\text{m}$.

Constitutive parameters Constitutive parameters for the wall k_1, k_2, k_3 which define the wall stiffness,

$$\frac{Eh}{r_0} = k_1 \exp(k_2 r_0) + k_3,$$

where E is Young's modulus, h the wall thickness, and r_0 the unstressed lumen radius. For the pulmonary veins, we set $k_1 = 0\,\text{Pa}$ and $k_3 = 26000\,\text{Pa}$, and $k_1 = 0\,\text{Pa}$ $k_3 = 5000\,\text{Pa}$ for arteries[1]. When $k_1 = 0$, k_2 is arbitrary.

Scaling factors The scaling factors α and β control the radius of daughter vessels within the structured tree. They are not set directly, but are controlled by the parameters ξ, γ, η in the relationships

$$r_p^\xi = r_{d_1}^\xi + r_{d_2}^\xi, \qquad \xi \in [2.33, 3], \tag{4.1}$$

$$\gamma = \frac{r_{d_2}^2}{r_{d_1}^2}, \tag{4.2}$$

$$\eta = \frac{r_{d_1}^2 + r_{d_2}^2}{r_p^2} = \frac{1+\gamma}{\left(1+\gamma^{\xi/2}\right)^{2/\xi}}, \qquad \eta > 1. \tag{4.3}$$

[1] 1 Pa = 75×10^{-3} mm Hg.

in which the subscript p denotes the parent vessel, and d_i, $i = 1, 2$ indicated the first or second daughter vessel. Only two of ξ, η, γ are independent. In the structured tree, all junctions are bifurcations. The scaling factors are given by

$$\alpha = (1 + \gamma^{\xi/2})^{-1/\xi},$$
$$\beta = \alpha\sqrt{\gamma}.$$

The first of these was originally suggested by Murray [95] and is derived from the principle of minimum work where $\xi = 3$. Later Uylings [96] derived a more general power law with $\xi \in [2.33, 3.0]$. Murray's law is applicable to laminar flows ($\xi = 3.0$), and $\xi = 2.33$ corresponds to a turbulent flow. The equations for γ and η comes from network analysis by Zamir [97] and are used to quantify the branching asymmetry and the lumen area change over a vessel bifurcation. These are applicable at all bifurcations given the self-similarity of the junctions and the fractal nature of a structured tree.

For the pulmonary circulation, Qureshi sets $\eta = 1.16$, $\xi = 2.76$, $\gamma = 0.41$, so $\alpha = 0.91$ and $\beta = 0.58$. As the scaling factors control the radii of vessels in the tree, and we set a minimum radius of vessels in the tree, we can alter them to model capillary rarefaction. Capillary rarefaction is characterised by reduction in density of microvascular networks, and is a hallmark of primary and secondary hypertension [98, 99] and fibrotic disease [100]. According to Cameron, Lang & Toyuz, in primary hypertension it is unclear whether vascular rarefaction arises due to increased blood pressure or causes it [98], while Kerkhove, Paciolla & Arpino note that rarefaction has been described in some individuals who are genetically predisposed to hypertension prior to its onset [99].

Length-to-Radius Ratio The length-to-radius ratio(l_{rr}) ratio governs the length of vessel segments with in the structured tree. The length l is a function of the radius r, since $l = r \cdot l_{rr}$. If the scaling parameters control the density of a vessel network, then l_{rr} controls how far that network can spread from the root. The l_{rr} varies throughout the body, and depends on the function of the perfused tissue. Arteries and veins need not have the same l_{rr}. Based on analyses from Fung [101] and experiments by Singhal *et al.* [102] and Huang *et al.* [103]. For pulmonary veins Qureshi sets $l_{rr} = 15.75$ and $l_{rr} = 14.54$ for veins.

Characteristic Radius Scale The characteristic radius scale is used to compute the Froude number $\mathcal{F} = u/\sqrt{gL_R{}^2}$, where u is local fluid velocity, g is acceleration due to gravity, and L_R the characteristic radius scale. Large pulmonary vessels have radius of about 10 mm, so we set $L_R = 10\,\text{mm}$. The value to which the characteristic radius is set depends on the tissue in which we are simulating blood flow. Typically, $\mathcal{F} < 1$ in coronary and pulmonary simulations.

Period The period T is the length of a single computational cycle, and should be set to the period of the (periodic) data imposed at the inlet. The period of a heart beat is 0.64 – 0.93 s [104]. We choose the period of a heart beat to be 0.7 s

Number of cycles We are free to choose the number of cycles (nominally heart beats) for which the simulation runs. During the first cycle, the model equations are solved at all spatial points in the computational domain and all time points in the period using an initial condition. In subsequent cycles, the equations are solved using the pressure, flow, and area values found in the previous cycle at the same spatial-step, and for the corresponding time-step. After some number of cycles, the

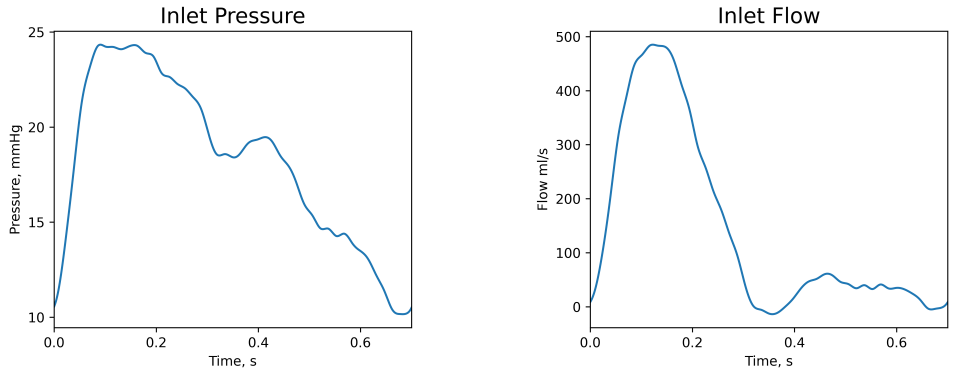

Figure 4.1: Measured flow and computed pressure at the inlet of the main pulmonary artery from Qureshi *et al.* [2]. Reproduced with data provided by the authors.

simulation converges to a periodic solution. We define convergence as a pressure and flow change less than 1% between a two consecutive periods.

Inlet Pressure Profile For toy simulations, I use a constant inlet pressure of 20 mm Hg. This is to reduce computational time, and to help highlight any changes made by the introduction of external pressures.

For the physiologically realistic simulations, we use the inlet profile Fig. 4.1. This comes from Qureshi *et al.* [2] and is the computed pressure at the main pulmonary artery inlet taken from simulations driven by a measured flow profile.

4.2 Toy Simulations

Here, we show that the computational model behaviour is intuitively sensible. In particular, it is volume conserving, there is a pressure drop between the arterial inlet and the venous outlet, and applying external pressures to vessels in the tree alters the flow and pressure profiles. Volume conservation over a cycle is an important check

for solution periodicity, i.e. that transients have decayed, and of adequate spatial resolution.

4.2.1 A Monofurcation

Due to constraints in the computational scheme, the large vessel tree needs to be comprised of at least 2 arteries and 1 vein. The constraint is that we are able to impose only one in/outlet boundary condition on each large vessel, so an artery may be either an inlet or give rise to a structured tree, but not both. This is a stenotic artery tree, and drains into a single vein via the structured tree. The morphometric data specifying an example of such a tree is given in Table 4.1. There is a monofurcation between the arteries.

The morphometric details of all the trees in which we simulate fluid flow are given in summary tables, such as in Table 4.1. The summary table for a network of n vessels contains n rows. Each row gives a unique index to a vessel, together with its length L, proximal radius in the reference configuration $r_0(0)$ and distal radius $r_0(L)$, as well as the index numbers of the vessels to which it is distally joined. Arteries can give rise to 1, 2, or 3 arteries, or are joined to a vein via a structured tree. The *type* column indicated which boundary conditions are applied to each vessel; the available types are

- Arteries:
  - Inlet: the inlet boundary condition is applied at the proximal end, and a junction matching condition at the other end.
  - Terminal: Vessels joined to the structured tree
- Veins:

Index	Daughter(s)	Length (mm)	Proximal Radius (mm)	Distal Radius (mm)	Type
0	1	40	11.5	11.5	Inlet artery
1	2	40	11.0	11.0	Outlet artery
2		40	11.0	11.0	Outlet and Terminal Vein

Table 4.1: Morphometric table for a toy tree of three vessels with a stenotic artery.

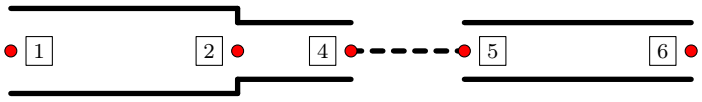

Figure 4.2: A cartoon of the simple, stenotic tree described in Subsection 4.2.1 and Table 4.1. The red circles indicate the points at which boundary conditions are imposed, and the points between which I check for conservation of flow. The dashed line represents the structured tree that joins the arterial and venous sides.

- Outlet: this vein drains the system and the outflow boundary condition is applied
- Terminal: these veins are joined to the structured tree
- Outlet and terminal: the vein is joined to the structured tree and also drains the system. There is only one generation of veins.

The model code is capable of returning fluid flow, fluid pressure, transmural pressure, fluid velocity, and lumen area at regularly spaced intervals (with a default of 2.5 mm) in each vessel at a given temporal resolution (128 points per period).

Impact of Number of Cycles

To illustrate the impact of the number of computational cycles on simulated flow and pressure, consider Fig. 4.3. The simulations shown here use a constant inlet pressure of 20 mm Hg and were run for 1, 4, and 16 cycles. The pressure and flow solution curves shown are from the inlet artery and the vein. As the number of cycles increases, the noise in the simulation decreases.

To determine if the simulation has converged, we compare the fluid pressure and flow at each spatial point in the computational domain in one period against the values for the previous period.

The maximal percentage difference in flow and pressure between cycles 1 & 2 is 956.6%, so the simulation has not converged after 1 cycle. However, the difference between cycles 5 & 6 is 0.85%, so cycle 5 is considered to be convergent, as all other subsequent cycles. Figure 4.4 shows plots of the percentage difference between flow and pressure in subsequent cycles at some of the spatial points with the vein.

Volume Conservation

Ensuring fluid volume is conserved is an important check for periodicity and adequate spatial resolution. If periodicity is achieved, fluid volume over a single period is spatially uniform.

From Fig. 4.3c, it is clear that volume is conserved along the length of the first artery. However, it is important to check that volume is conserved over the monofurcation and structured tree. For 16 cycles, there is no volume change over the monofurcation or the structured tree. There is a change of 0.2 ml (0.06%) over the length of the daughter artery and 0.14 ml (0.04%) over the length of the vein. The total change over the tree is 0.06 ml.

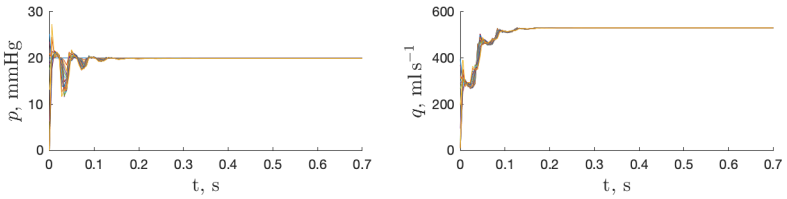

(a) Simulated pressure and flow for 1 cycles.

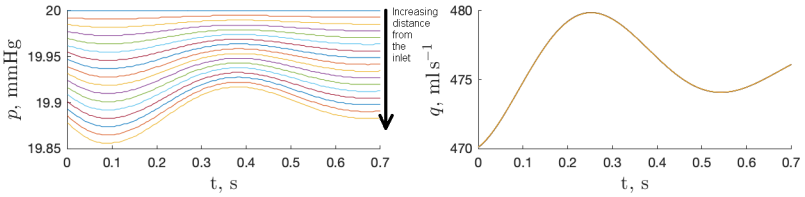

(b) Simulated pressure and flow for 4 cycles.

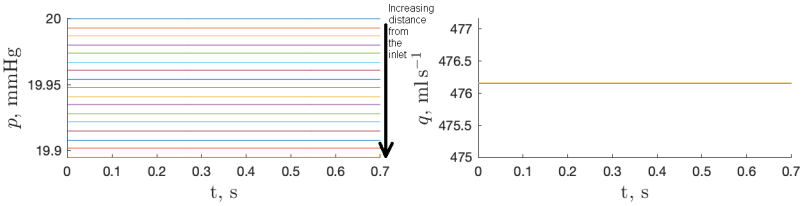

(c) Simulated pressure and flow for 16 cycles.

Figure 4.3: Simulated flow and pressure in the inlet artery of the simple stenotic tree for (a) 1, (b) 4, and (c) 16 cycles. Simulations run for insufficient time have high pressure and flow changes which decay in subsequent runs. The curves within each panel show the pressure and flow at different spatial positions within the artery. In each case, the final cycle starts at $t = 0$ and runs to $t = 0.7$.

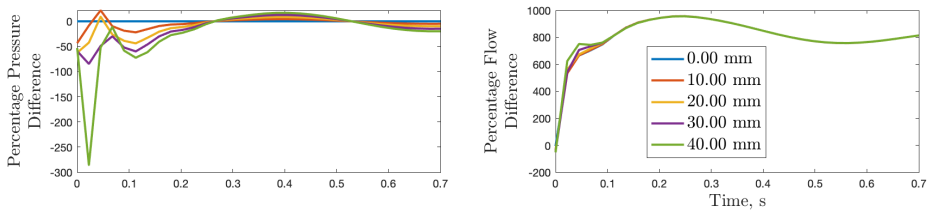

(a) Comparison of flow and pressure in 1 & 2 cycles.

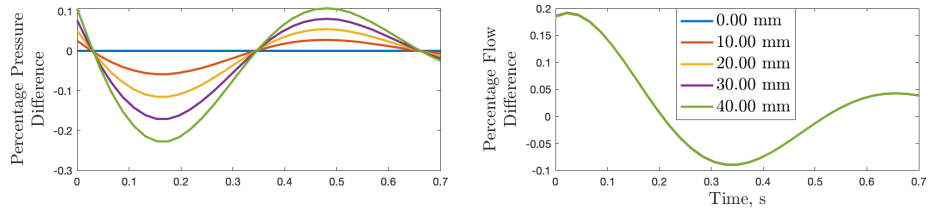

(b) Comparison of flow and pressure in 4 & 16 cycles.

Figure 4.4: Convergence tests: Percentage differences between simulated pressures for 1 & 2 and 4 & 16 computational cycles at the several points with the vein.

Volume conservation is not an artefact of constant inlet pressure. Table 4.2 shows volume differences between points marked in Fig. 4.2 in a simulation using the physiologically realistic pressure profile and 4 computational cycles.

From table 4.2, we can see that in the 4 cycle simulation, the change in fluid volume between the ends of all vessels, over each junction, and over the whole tree is very small. There is a total volume gain of 0.571 ml across the between the arterial inlet and venous outlet, which is a volume increase of 0.28% from the initial fluid volume. Since the volume change is so small, we conclude that in the absence of external pressure, the stenotic vessel junctions and the structured tree are volume preserving.

Volume conservation failure can occur because of an inappropriately large spatial step size. Figure 4.5 shows how total volume difference over the tree depends on step-

Position	Volume (ml)	Volume change (ml)	Cumulative change (ml)
1	203.777		
Parent 2	203.788	0.011	0.011
Daughter 2	203.795	0.007	0.018
4	203.890	0.095	0.113
5	204.285	0.395	0.508
6	204.348	0.063	0.571

Table 4.2: For each position shown in Fig. 4.2, we find the fluid volume that passes that point over the course of one period. Point 2 is the junction point between the parent and daughter vessel, so appears twice in the computational domain, so is included twice in the table. This is recorded in the *Volume* column. The *Volume change* gives the difference between the fluid volumes at subsequent points; *Cumulative change* is the sum of these.

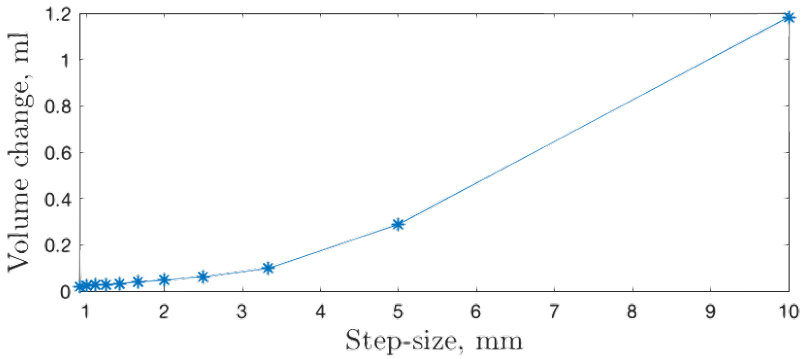

Figure 4.5: Decreasing spatial step-size increases volume conservation for a fixed number of cycles and temporal resolution.

size for a fixed number of cycles and temporal resolution in a simulation driven by constant pressure. In general, volume conservation improves as step-size decreases.

Volume changes across a single period between two points in the computational domain of less than 3% of the inlet volume are considered negligible, as these have likely arisen due to insufficient resolution or computational cycles. As such, they can be straightforwardly resolved but at the cost of increasing over all computation time.

Steady External Pressure

In this sub-section, I aim to show how the application of steady external pressure impacts the simulated blood flow and pressure. To do this, I consider four cases with steady external pressure:

(i) an external pressure of 0 mm Hg is applied to small and large vessels

(ii) 10 mm Hg on the large vessels only

(iii) 10 mm Hg on the structured tree only

(iv) 10 mm Hg on large vessels, and 10 mm Hg on small vessels.

A steady inlet pressure of 20 mm Hg drives the flow and with the exception of external pressure, all parameters are fixed between simulations. The simulations are set to run for 12 cycles of 0.7 s each. Figure 4.6 shows the simulated pressure and flow at the distal ends of all three vessels (positions 2, 4 & 5 in Fig. 4.2). Fluid volume change between the arterial inlet and venous outlet is $< 1\%$ in all simulations.

In arteries, the application of external pressure to large vessels in (ii) & (iv) causes slight changes in fluid pressure and flow ($< 1\%$) and a decrease in lumen area by 7.5%. Lumen area decreases when large vessels are compressed, as transmural pressure decreases, and lumen area depends on transmural pressure. Steady external pressures applied to small vessels appear to have little effect on fluid pressure, flow, or lumen area.

We expect a pressure drop along the length of a vessel. In all cases seen in Figures 4.6, we can see that the pressure at distal end of parent artery is higher than that in its daughter. These are both higher than the pressures seen in the vein. This is an expected behaviour. The pressure drop over the structured tree is high, as it is composed of many vessels.

Computationally Viable Domain

We wish to find the computationally viable domain of external pressures. By this, we mean the combinations of external pressures amplitudes for which simulations run to completion given a certain set of parameters, data, and initial conditions. Knowledge of this domain is useful, as it can help to inform later choices of external pressure values. The size and shape of the region will depend on many factors, including the all parameter choices made for a particular set of simulations, the inlet and outlet

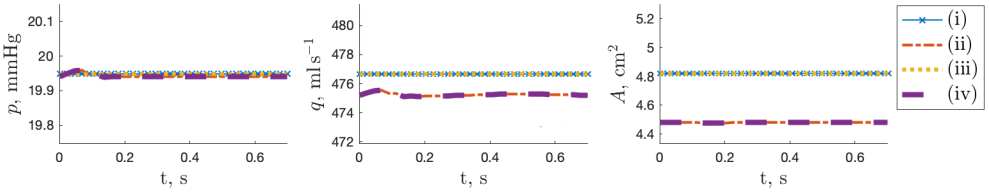

(a) Fluid pressure, flow, and lumen area at the distal end of the inlet artery.

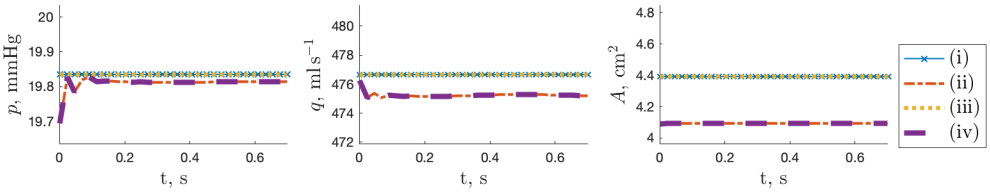

(b) Fluid pressure, flow, and lumen area at the structured tree end of the terminal artery.

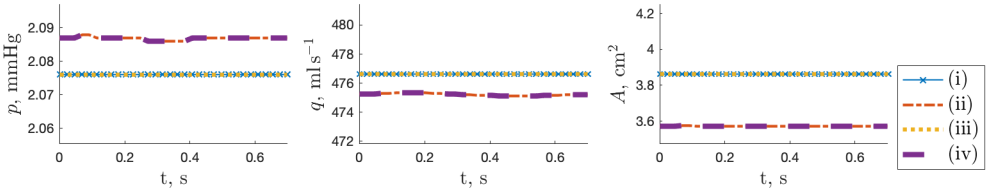

(c) Fluid pressure, flow, and lumen area at the structured tree end of the vein.

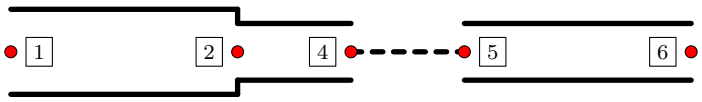

Figure 4.6: Simulated pressure p, flow q, and lumen area A at the distal ends of the (a) inlet artery (point 2), (b) terminal artery (point 4), and (c) vein in the monofurcating tree (point 6). Items in the legends refer to the simulations in which (i) external pressures of 0 mm Hg are applied to small and large vessels, (ii) external pressure is applied to large vessels only, (iii) external pressure is applied to small vessels only, and (iv) external pressure is applied to small and large vessels. The final panel is Fig. 4.2 for convenience.

boundary conditions, and modelling assumptions and choices (such as for the velocity profile and tube law).

By construction, transmural pressure $\varphi = p - \text{Þ}$ where p is fluid pressure, and Þ is external pressure. External pressures can be compressive (Þ > 0) or expansive (Þ < 0).

To find the computationally viable domain, fix all parameters including spatial and temporal steps, and data in the model except for the pressure amplitude applied to small and large vessels. Next, define ranges of small and large vessel pressure to search and discretise this into a grid covering the space. For each grid point, run one simulation with the appropriate small and large vessel external pressure and record the outcome (success or failure) and any error messages that arise. With this data, we can visualise the computationally viable domain such as in Fig. 4.7

I choose to use $-100, -95, ..., 95, 100$ mm Hg as the small and large steady external pressures. There are 41 values in the list, so 1681 simulations to run. Decreasing pressure step-size increases the resolution of the viable domain, but also increases computational time. Fluid flow is driven with a steady inlet pressure of 20 mm Hg.

The faults that occur in this test are the violation of the Courant–Friedrichs–Lewy (CFL) condition, and a convergence failure of solutions when matching the arterial and venous sides over the structured tree. From Olufsen, [44] the CFL condition requires

$$\frac{\Delta t}{\Delta x} < \left| \frac{q(x,t)}{A(x,t)} \pm c(x,t) \right|^{-1}$$

to be satisfied at all (x, t), where q, A, & c are flow, lumen area, and wave speed. The CFL condition is checked at each temporal and spatial step in the computational domain.

If the CFL condition is violated for a particular run, it is possible to increase

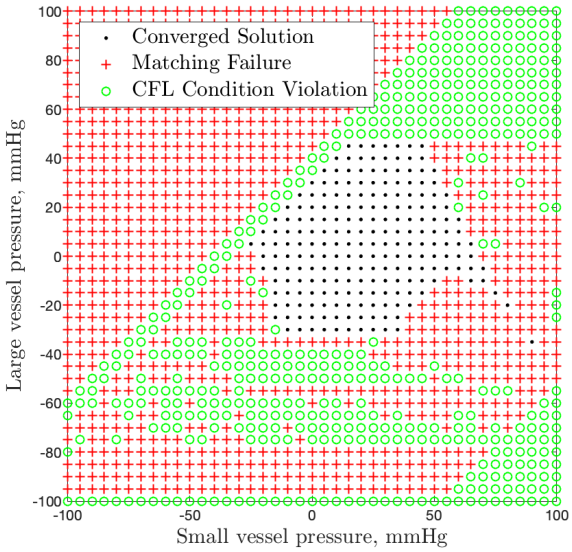

Figure 4.7: The computationally viable domain representation. The central region of black points is the computationally viable domain. It is bounded by infeasible regions in which the matching condition between the arterial and venous side failed (+), or the CFL condition is violated (o).

spatial and temporal resolution so that it is not violated. However, this increases computational cost. Failure to match arterial and venous sides occurs when the Newton scheme (see Section 3.2.4) fails to converge in a prescribed number of iterations. It is possible to increase the number of iterations allowed. Both of these solutions increases computational time. Further, the external pressures for which the simulation fails are high relative ($\geq |20|$ mm Hg) to the 20 mm Hg inlet pressure.

Time-Varying External Pressure

We can apply periodic time-varying external pressures with period in the model, with the constraint that the period of the external pressure and inlet pressure are

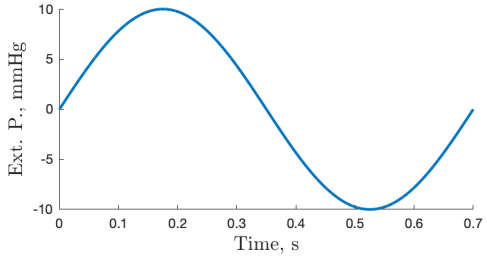

Figure 4.8: Sinusoidal external pressure signal with amplitude 10 mm Hg and period $T = 0.7$ s.

the same. External pressures applied to the tree can be time-dependent, but must have the same period as the inlet data. To show how time-varying external pressure changes simulated flow and pressure, we apply a sinusoidal external pressure with amplitude 10mm Hg shown in Fig. 4.8 in the following four cases

(i) No external pressure,

(ii) External pressure applied to large vessels only,

(iii) External pressure applied to small vessels only,

(iv) External pressure applied to both large and small vessels.

Other than the external pressure, these simulations use the same set of parameter values as those shown in Fig. 4.6.

Figure 4.9 shows fluid pressure p, flow q, and lumen area A at the distal ($x = L$) end of the inlet artery, terminal artery, and vein in the monofurcating tree. Inlet pressure is a steady 20 mm Hg. All the simulations are volume conserving and have reached a periodic state.

Due to the external pressure choice, vessels are compressed from $0 - 0.35$ s and expanded from $0.35 - 0.7$ s. During compression, the fluid pressure in all vessels drops

below the fluid pressure in the reference case. This drop occurs at different times depending on the combination of external pressures, but this can straightforwardly be understood as a consequence of the compliant vessel walls and pulse propagation. Conversely, in the latter half of the period, vessels experience expansion, and fluid pressure increases. The fluid pressure minima and maxima are achieved earliest in the simulation where only large vessels are subject to external pressure (ii), and latest when only small vessels are subject to it (iii). The minima when both small and large vessels is subject to external pressure (iv) lies between these. The pressure deviations from the reference case (i) are approximately 10% of inlet pressure in the inlet artery, which constitutes a significant change.

When small vessels are subject to external pressures in cases (iii) & (iv), flow changes by up to $500\,\mathrm{ml\,s^{-1}}$ over the course of the period as compared to the undisturbed case (i). When the structured trees are compressed, arterial flow is significantly reduced compared to the reference state; conversely when they are expanded, flow increases. Peaks in arterial flow coincide with troughs in venous flow, and vice versa.

Lumen area is governed by the tube law (2.23)

$$\varphi(x,t) = p(x,t) - \text{Þ}(t) = \frac{4}{3}\frac{Eh}{r_0(x)}\left(\sqrt{\frac{A(x,t)}{A_0(x)}} - 1\right).$$

When large vessels are subject to an external pressure, we expect lumen area to change in line with the transmural pressure. That is, area will decrease during compression and increase during expansion. In these cases (ii) & (iv), there is a change of 8% from lumen area in the reference case. Subjecting only the structured tree to external pressure alters large vessel lumen area by no more than 2%.

When structured trees are compressed, we expect to see a back up of fluid and decrease in flow due to increased down-stream resistance; the fluid back up also

causes an increase in lumen area when small vessels are compressed. We can see the drop in arterial flow in small vessel compression in the top two middle panels of Fig. 4.9(a)&(b), and the higher lumen area in cases with structured tree compression in the right hand panels (compare (i) with (iii) and (ii) with (iv)). When large vessels are compressed, we see a drop of approximately 6% in lumen area at the peak of compression as compared to the undisturbed case. This is consistent both with the constant external pressure simulations.

As already observed, fluid pressure drops significantly (by 90% from from 19.9 mm Hg to 2 mm Hg) over the structured tree, but flow volume is conserved. There are peaks in venous flow that correspond to the arterial flow troughs in the cases of vascular bed compression (iii) & (iv). This can be understood as fluid begin squeezed out of the vascular bed. As structured trees are subject to expansive pressures, arterial flow increases and we see corresponding drops in venous flow. There is a finite fluid volume present in the system, so peaks of flow in one vessel at a certain time necessitate that there will be low flow in downstream vessels at that time. We can also see this behaviour in measured arterial and venous flow [105].

Negative Fluid Pressure In this thesis, fluid pressure $p(x,t)$ is pressure along the centreline of each vessel. In the vein we see $p(x,t) < 0$ mm Hg during the application of pressure to the small vessels. This can be straightforwardly explained by Bernoulli's principle: flow velocity is rapidly decreasing, hence the fluid velocity is high, and fluid pressure drops.

There is venous backflow (reversal of flow direction) shortly after fluid pressure drops below 0 mm Hg.

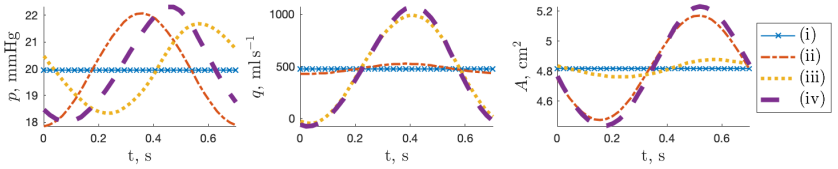

(a) Fluid pressure, flow and lumen area at the distal end of the inlet artery.

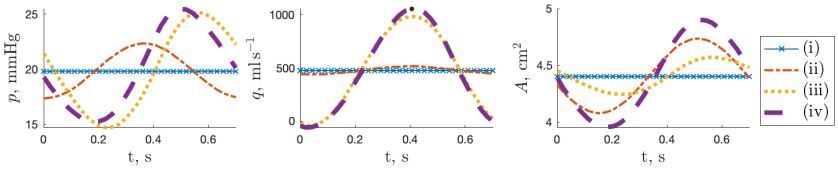

(b) Fluid pressure, flow and lumen area at the structured tree end of the terminal artery.

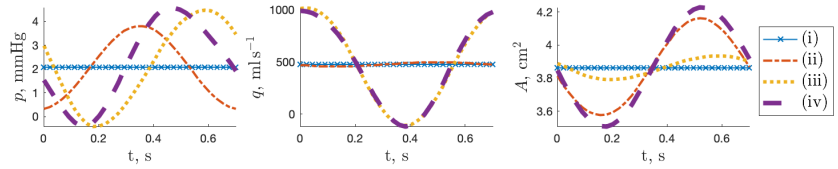

(c) Fluid pressure, flow and lumen area at the structured tree end of the vein.

Figure 4.9: Simulated fluid pressure, flow, and area at the distal end of both arteries and the vein with a periodic external pressure profile as shown in Fig. 4.8. The legends refer to cases: (i) no external pressure; (ii) pressure applied to large vessels only; (iii) pressure applied to small vessels only; (iv) pressure applied to large and small vessels.

Summary Time-varying external pressure applied to large vessels impacts fluid pressure p (by up to 75%), and lumen area A (up to 10%) flow q (up to 10%) in all vessels. External pressures applied to the structured tree do not significantly impact lumen area A (by up to 5%), but significantly change fluid pressure and flow (by up to 25 and 100%, respectively). The changes in p, q, A seen when external pressures are applied to the whole tree are between those for the application to large vessels alone and small vessels alone. All percentages are relative to the undisturbed case (i).

Computationally Viable Domain

As with the steady external pressure simulations, we wish to find the computationally viable domain for time-dependent external pressures. To find the domain, we repeat the analysis above described, but with a sinusoidal external pressure instead of a steady one. This procedure results in Fig. 4.10. The size and shape of this region will additionally depend on the external pressure profile used in simulations.

There were 37 combinations of external pressure amplitudes that result in faults other than the CFL condition violation and a boundary matching failure; 10 of these were caused by a division by 0 in a residual equation, and the other 27 were caused by a convergence failure in the Newton scheme that matches the monofurcation.

The sinusoidal external pressure (Fig. 4.8) is compressive and expansive, so the computationally viable domain has rotational symmetry about the origin.

4.2.2 A Bifurcation

In addition to monofucations (one-to-one branching), we are able to simulate flow through networks containing bifurcations (one-to-two branching). In this subsection,

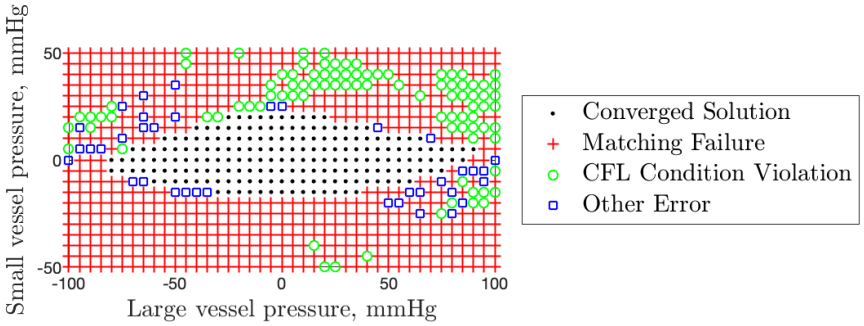

Figure 4.10: The central black region represents combinations of pressure amplitudes for which simulations converge within 6 computational cycles of length 0.7 s, with fixed spatial and temporal step size. Outwith this region, simulations failure is caused arterial-venous boundary matching failure (+, 543 instances), CFL condition violation (○, 91 instances), and other faults (□, 37 instances).

we consider a symmetric bifurcating tree. The summary table for this tree is given in Table 4.3; a cartoon depicting this tree can be seen in Fig. 4.11. Constant pressures of 20 mm Hg and 2 mm Hg are prescribed at the inlet boundary and outlet boundaries, respectively.

Volume Conservation

The fluid volume that passes through the arterial inlet over one period is 470.83 ml, and 235.45 ml is drained by each veins over the same period. There is an insignificant volume loss of 0.07 ml (0.01% of inlet volume) over the course of a period. We have seen that volume is conserved over the structured trees and along each vessel. Hence, the bifurcation matching condition must also be volume conserving. All values are given to 2 decimal places.

Index	Daughter(s)	Length (mm)	Proximal Radius (mm)	Distal Radius (mm)	Type	Marked nodes
0	1, 2	40	11.5	11.5	Inlet artery	1, 2
1	3	40	11.0	11.0	Outlet artery	2, 3
2	4	40	11.0	11.0	Outlet artery	2, 4
3		40	11.0	11.0	Outlet and Terminal Vein	5, 7
4		40	11.0	11.0	Outlet and Terminal Vein	6, 8

Table 4.3: Morphometric table for a toy tree of five vessels with a symmetric arterial bifurcation.

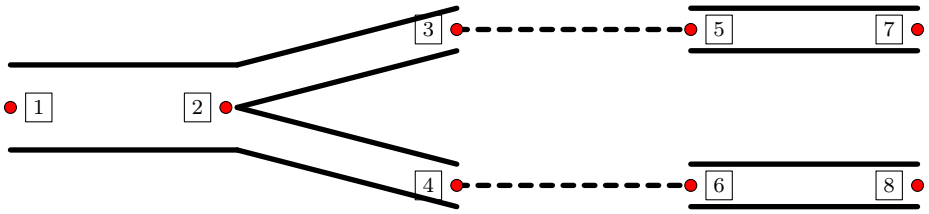

Figure 4.11: A cartoon of a bifurcating tree described in Subsection 4.2.2 and Table 4.3. The red circles indicate the points at which boundary conditions are imposed, and the points between which I check for conservation of flow. The node labelled 2 is the bifurcation point between the three vessels in the junction; this is the point at which the fluid volume is split between the two daughter vessels. The dashed line represents the structured tree that joins the arterial and venous sides.

Spatial Variation in External Pressure in the Bifurcating Tree

For model simplicity, we assumed that external pressure is spatially uniform on the length scale of a single vessel segment. However, we are able to apply different external pressures to each large vessel and to each structured tree, thus allowing spatial variation on a whole-network scale.

To illustrate the impact of spatial variation in external pressure, I apply a sinusoidal external pressure with amplitude 10 mm Hg to the top daughter (between (2) and (3)) artery, structured tree, and vein (Vessels 1 & 3 in Table 4.3). All other vessels are not subject to external pressure. This is the disturbed case. We define a reference case against which to compare this by setting all external pressures to 0. Figure 4.12 shows the difference in pressure and flow between the cases at the mid-point of each large vessel. A negative difference means that the quantity in the vessel is higher in the reference case.

As has already been observed, compressive external pressures in the first half of the period decrease arterial and venous fluid pressure, and arterial flow below the values observed in the reference case. Arterial flow increases by up to 100% compared to the reference case, and fluid pressure by 25% which are in line with the changes seen in the stenotic tree.

Vessels 1 and 3 are subject to the sinusoidal external pressure, as is the structured tree that joins them. Flow from Vessel 1 into 3 is restricted during the first half of the period, so arterial flow drops during this time and venous flow increases above flow in the reference case. In the latter half of the period, external pressures are expansive, so arterial flow increases above the reference level. This effect is seen in the upstream Vessel 0, and propagates through into the sibling Vessel 2. As the structured tree between Vessels 2 and 4 is not subject to an external pressure, the

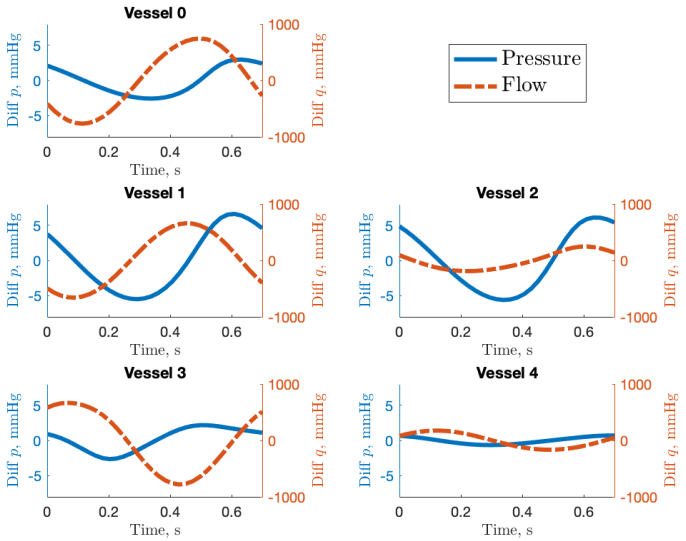

Figure 4.12: A sinusoidal external pressure with amplitude 10 mm Hg is applied to the structured tree that joins vessels 1 and 3. This is compressive in the first half of all periods and expansive in the latter half. In each panel, wer present the difference between pressure (solid blue, left axes) and flow (dotted orange, right axes) against a simulation in which 0 mm Hg of external pressure are applied to all vessels.

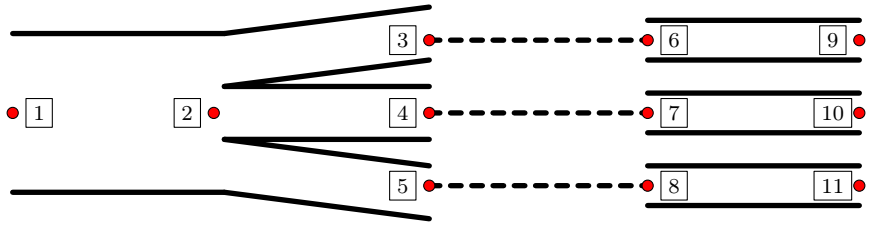

Figure 4.13: A cartoon of the simple trifurcating tree described in Subsection 4.2.3 and Table 4.4. The red circles indicate the points at which boundary conditions are imposed, and the points between which I check for conservation of flow. The nodes labelled 2 is the trifurcation point between the four vessels in the junction; this is the point at which the fluid volume is split between the two daughter vessels. The dashed lines represents the structured tree that joins the arterial and venous sides.

flow in these is more similar to reference flow than in the other branches. Flow range in Vessel 1 is -300 – 1000 ml s^{-1}, where as it is 200 – 600 ml s^{-1} in Vessel 2. Similarly for venous flow, the left flow range is -400 – 900 ml s^{-1}, and the right flow range is 180 – 500 ml s^{-1}.

Spatially inhomogeneous, time-dependent external pressures can be modelled with the framework described in this thesis. Further, such external pressures influence fluid pressure, hence flow, throughout the network regardless of the site(s) of pressure application. The effect of external pressure decreases with increasing distance from the site of pressure application.

4.2.3 Trifurcations

Similarly to the mono- and bifurcating trees, we can model flow through trifurcations (one-to-three branching). As with the previous two sections, we set up a tree with a single large vessel junction as described in Table 4.4 and illustrated in Fig. 4.13.

Index	Daughter(s)	Length (mm)	Proximal Radius (mm)	Distal Radius (mm)	Type
0	1, 2, 3	40	11.5	11.5	Inlet artery
1	4	40	11.0	11.0	Outlet artery
2	5	40	11.0	11.0	Outlet artery
3	6	40	11.0	11.0	Outlet artery
4	N/A	40	11.0	11.0	Outlet and Terminal Vein
5	N/A	40	11.0	11.0	Outlet and Terminal Vein
6	N/A	40	11.0	11.0	Outlet and Terminal Vein

Table 4.4: Morphometric table for a toy tree of seven vessels with a symmetric arterial trifurcation.

As has been shown in mono- and bifurcating trees, fluid volume is conserved within vessels and over the structured tree. So, to check that volume is conserved over the trifurcation, it is sufficient to check the volume change between the arterial inlet and venous outlets over a period. For this purpose, we set the inlet fluid pressure boundary condition to be a steady 20 mm Hg. The fluid volume that passes the inlet is 701.31 ml. The fluid volume that passes each venous outlet is 233.88 ml, and total outlet volume is 701.44 ml. The volume change between the ends is -0.13 ml or -0.02% of inlet volume, hence fluid mass is considered to be conserved.

Note that flow volumes increase with increasing network volume. This is reasonable as the volume of the network has increased, but the pressure prescribed at the inlet is the same for all networks, so fluid volume must increase.

Pressure Drop In simulations driven with a steady inlet pressure of 20 mm Hg and outlet condition of 2 mm Hg, there is a pressure drop of 90% (to 2 mm Hg) from the arterial inlet to the venous outlet. In the monofurcating tree, there was a 0.2 mm Hg pressure drop in the arterial side, and a 18 mm Hg pressure drop over the structured tree (see Fig. 4.9). This is also the case for the bifurcating and trifurcating networks. In the trifurcating network, peak fluid pressure in the parent artery is 20 mm Hg, which drops to 19.7 mm Hg in each of the daughters, and further to 2.1 mm Hg in each vein.

4.3 Pulmonary Flow During Respiration

We have explored some modelling scenarios in toy trees, but we can also simulate blood flow under more realistic scenarios.

I set up a physiologically realistic tree of large pulmonary arteries and veins as described by Qureshi [3, pp. 23]. This large vessel tree contains 7 arteries in three generations and 4 veins of a single generation. The main pulmonary artery (MPA) is the inlet vessel, and all four veins drain into the low-pressure left atrium. Table 4.5 contains the full morphometric details. A schematic of the network can be seen in 4.14.

Vessel Name	Index	Daughter(s)	Length (mm)	Proximal Radius (mm)	Distal Radius (mm)	Type
MPA	0	1, 2	45.0	13.6	13.0	Inlet artery
LPA	1	3, 4	57.5	9.3	6.0	Artery
RPA	2	5, 6	25.0	11.0	10.8	Artery
LIA	3	7	12.5	5.7	5.5	Outlet artery
LTA	4	8	10.0	4.6	4.6	Outlet artery
RTA	5	9	22.5	10.4	9.0	Outlet artery
RIA	6	10	10.0	5.8	5.8	Outlet artery
LIV	7		12.4	5.9	5.5	Outlet and Terminal Vein
LSV	8		15.0	5.1	4.6	Outlet and Terminal Vein
RSV	9		21.8	9.7	9.0	Outlet and Terminal Vein
RIV	10		20.0	6.4	5.8	Outlet and Terminal Vein

Table 4.5: Morphometric table for a toy tree of seven vessels with a symmetric arterial trifurcation.

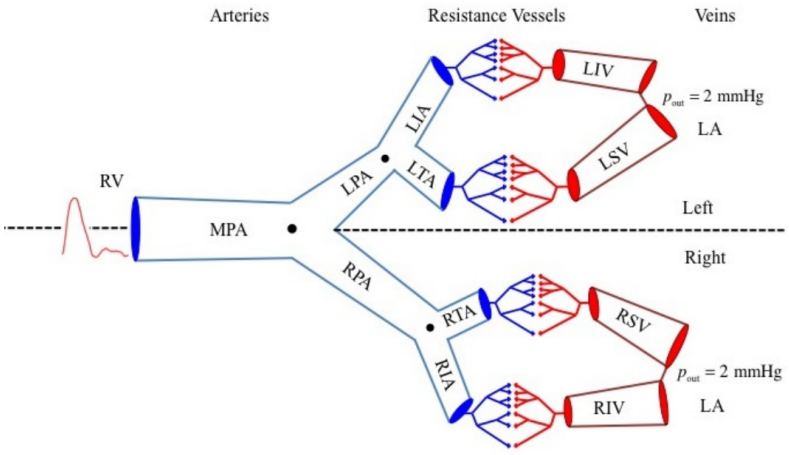

Figure 4.14: A reproduction of the pulmonary vascular network schematic from Qureshi [3]. This schematic shows the spatial relationship of named arteries and veins which are related to indices in Table 4.5.

4.3.1 Time-Dependent Pressure Profiles

Under normal circumstances, the human lung is surrounded by the pleural cavity, a fluid filled sack that is attached to the inner surface of the ribs and upper surface of the diaphragm. During quiet respiration, the ribs move upwards and outwards and the diaphragm moves down, increasing the volume of the chest cavity and subjecting the lungs to a negative pressure which forces them open [106]. Several studies, for example [9, 10, 106, 107], report measurements of pleural cavity pressure during quiet respiration, coughing, and spontaneous pneumothorax.

Pneumothorax is defined as the presence of air within the pleural cavity; a spontaneous pneumothorax is a pneumothorax with sudden onset without apparent cause such as underlying disease or trauma [108]. During a pneumothorax, the pleural pressure of the affected lung increases, and may rise above 0 mm Hg, relative to atmospheric pressure [10].

Initially, we wish to investigate the changes in pulmonary flow predicted by the model during normal respiration, as compared to the model without external pressure. In order to do this, we must make a external pressure profile that is representative of a breath.

Kaneda, Nakano & Murakawa present measurements of pleural cavity pressure in patients with spontaneous pneumothorax [10, Fig. 1]. The waveform of the breaths presented here are qualitatively similar to those for quiet respiration shown by Hu *et al.* [107, Fig. 3], but with less noise. The pressures measured by Kaneda, Nakano & Murakawa have a range of -1 to 1 mm Hg. Pleural cavity pressure is negative relative to atmospheric pressure during quiet respiration [109]. We can shift and stretch any profile to fit in the required pressure range for use in later simulations, which is addressed shortly. We choose to use pleural pressure measurements from patients with pneumothoraces as such data are difficult to find for quiet respiration. The wave forms in both cases should be similar as the pressure change is being driven by the motion of the ribcage and the diaphragm.

We digitize the profile shown in Fig. 4.15a[2] and separate the signal into individual breaths at the lowest 6 local minima values[3] (highlighted in Fig. 4.15b). The individual breaths range from 4.5 – 6 s in length, and can be seen together in Fig. 4.15c. One of the breaths features a substantial drop of 1 mm Hg during the expiratory phase and is discarded. The mean breath pressure profile is found by normalising the lengths of the remaining 5 breaths then finding the arithmetic mean at each time point in the period. The mean profile seen in Fig. 4.15d is not periodic. To achieve periodicity, we find the first time at which the final pressure value is achieved and discard the portion of the profile before that time. The discarded portion accounts

[2]using WebPlotDigitizer

[3]Using `scipy.signal` in Python3.

for 3.5% of the period length. Finally, we choose the length of a breath to be 5.6 s, giving Fig. 4.15e.

The length of each breath represented by the data is between 4.5 and 6 s. I assume that one heartbeat is 0.7 s, and that there are exactly 8 heart beats in one breath, so each breath has a period of 5.6 s. This is slightly outwith the range of 3.75 - 5 s per breath reported by Barrett *et al.* [110].

However, this profile was measured in a patient with a spontaneous pneumothorax. Pneumothoraces change pleural cavity pressure. To obtain a profile for quiet respiration, we vertically shift and rescale the profile $g(t)$ in Fig. 4.15e to give pleural pressure

$$h(t) = \frac{\hat{g}(t)(a-b)}{\max(\hat{g}(t))} + b,$$

in the desired range a – b mm Hg.

As reported by Zielinska-Krawczyk *et al.* [106], pleural pressure during quiet respiration varies between approximately -7.4 mm Hg (inspiration) and -3.7 mm Hg (expiration), and intrapulmonary pressure between -3.7 mm Hg and 3.7 mm Hg for inspiration and expiration, respectively. The intrapulmonary pressure is the pressure within the lung tissue itself, and hence is the pressure that should be applied to the structured trees. Mentzer, Tsuda & Loring [11] give pressure profiles in normal respiration with pressures between about -10 mm Hg (inspiration) and -3 mm Hg (expiration).

In general, pleural pressure drops during inspiration, and increases during expiration, followed by a period of constancy. It is the pattern of changes I wish to investigate here, rather than establishing a patient specific simulation.

The respiratory pressure curves I use begin at peak inspiration, followed by expiration from approximately 0 to 1.5 s; inspiration begins again at about 4 s.

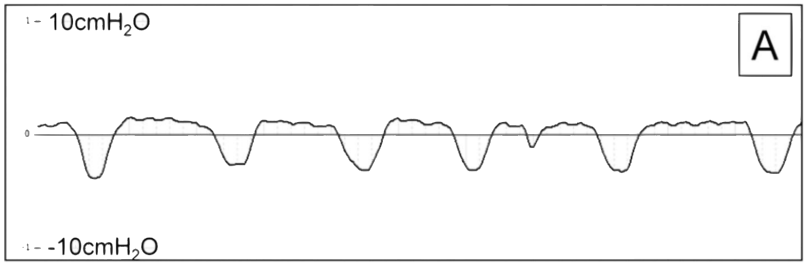

(a) Reproduction of Figure 1 A from Kaneda, Nakano & Murakawa [10]. Cropped and resized. The vertical axis is pressure in centimetres of water column; the horizontal axis is time.

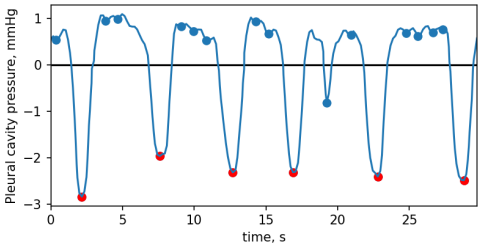

(b) Reproduction of the data from panel (a) with all local minima marked in red or blue points. The six red points indicate the start/end of the breaths.

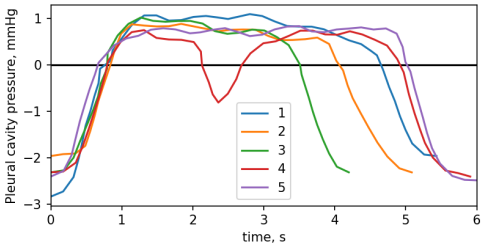

(c) The five breaths are isolated and minimum time is set to 0s.

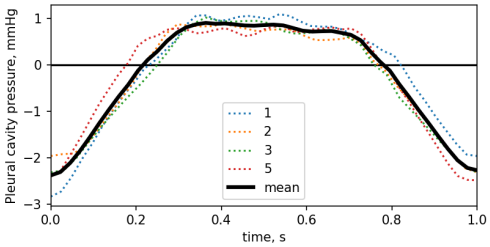

(d) The cleaned and normalised breath pressure profiles (dotted lines) and the resulting mean profile (solid black).

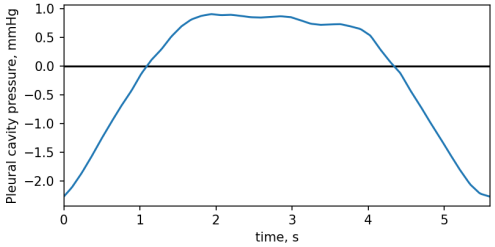

(e) Final periodic spontaneous pneumothorax external pressure profile $g(t)$.

Figure 4.15: Flow and pressure plots illustrating the impact of external pressures applied to the structured tree with and without compression of the large arteries.

Inlet Pressure

As I have chosen to simulate flow over the course of eight heartbeats, I must use an inlet pressure profile covering eight heartbeats. To make this, I simply take eight copies of the original inlet pressure profile shown in Fig. 4.1 in sequence.

4.3.2 Quiet Respiration

We have created pressure profiles within the pleural space and lung during quiet respiration. Using these, we can carry out preliminary investigations on the impact of quiet respiration on pulmonary flow. Quiet respiration, also called normal, good or unlaboured breathing, is the natural breathing pattern of mammals at rest. In quiet respiration, expiration relies only on the elastic recoil of the lungs [111].

Firstly, does the model predict flow changes throughout the respiratory cycle and are the predicted changes in line with observed changes reported in the literature?

In order to evaluate the effect of a respiratory cycle, we simulate two scenarios using the morphometry, parameter values, and pressure profiles established in this chapter. The first scenario is a reference case with no external pressure, the second is with the profiles for quiet respiration. We compute the difference between flows and pressures in the cases with and without respiration at the proximal ($x = 0$) and distal ($x = L$) ends of the MPA (Vessel 0 in Table 4.5) and the left interlobar pulmonary vein (Vessel 9). This can be seen in Fig. 4.16a. Figure 4.16b shows the pressure p (left) and flow q (right) at the distal end of the MPA with (solid blue) and without (orange dashed) respiration pressure. The pressure and flow waveforms are very similar to those computed by Qureshi [3] shown in Fig. 4.1 without external pressure. This is unsurprising as respiratory pressures are low relative to pulmonary arterial pressure, so we would not expect large differences in the waveforms.

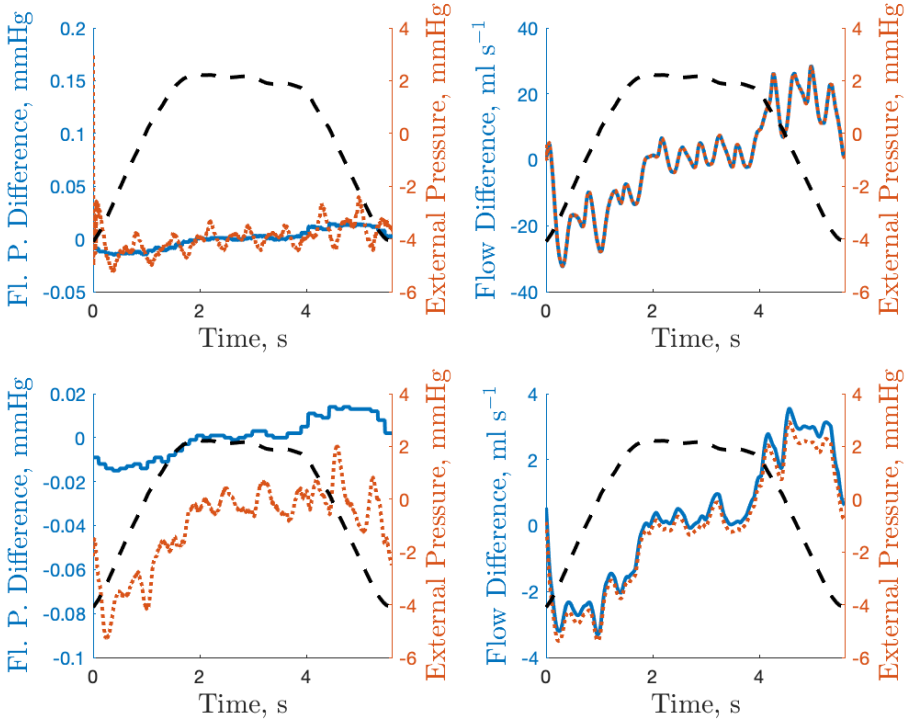

(a) Plots of the difference between reference and disturbed pressure (left) and flow (right) in the main pulmonary artery (top) and the left interlobar pulmonary vein (bottom). The MPA is Vessel 0 and left interlobar pulmonary vein is Vessel 9 in Table 4.5). Each panel shows the proximal ($x = 0$, solid blue) and distal ($x = L$, dotted orange) difference over one breathing cycle of 8 heart beats of 5.6 s. The intrapulmonary pressure is shown in dashed black, with a scale on the right hand axis for each plot.

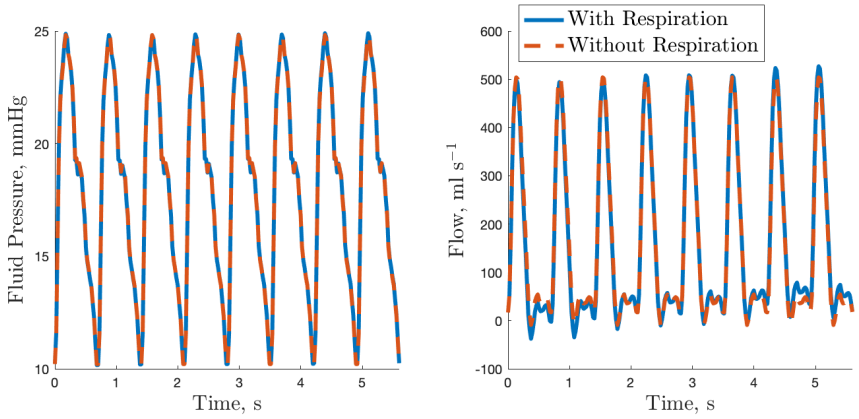

(b) Flow and pressure curves with (blue) and without respiration (orange dashed) at the distal end of the MPA. The difference between these curves is shown in the panel above.

Figure 4.16: Pressure and flow changes during quiet respiration in the MPA and left interlobar pulmonary vein.

A positive difference implies that the pressure or flow in the disturbed case is higher than in the reference case; a negative difference means that the reference quantity is higher. In general, we see that the sign of the difference is opposite to that of the gradient.

Neither mean flow nor total fluid volume vary between the reference case simulations and those with quiet respiratory external pressures. The blood volume at the inlet monotonically increases from 230 ml during the first heart beat to 247 ml during the final heartbeat. The inlet volume in the reference simulation is 238 ml per heart beat. According to Klabunde [112], the expansion of the lung during inspiration causes pulmonary blood flow to increase. Conversely, during expiration lung volume decreases and so does pulmonary flow. This is what the model predicts: flow decreases during inspiration, and increases during expiration, as compared to the reference case.

We impose pressure based boundary conditions at $x = 0$ in both vessels represented in Fig. 4.16a, so it is reasonable that the pressure difference between the disturbed and reference case is low at this end.

There are drawbacks to modelling pulmonary flow during respiration in the manner described above. Most notably, that there is a complex feedback loop between respiration, cardiovascular output, and venous return described by Klabunde [112]. Essentially, venous return, heart rate, and stroke volume all vary throughout the respiratory cycle. Further, we do not account for variation in heart rate or stroke volume [113, 114] throughout the respiratory cycle. Addressing any of these issues is beyond the scope of this thesis.

For the quiet respiration simulations, we assumed that pleural space and intrapulmonary pressures are spatially constant. However, they are not spatially constant: there is a hydrostatic gradient in pleural that varies with posture and is a result of

gravity [11]. Intrapulmonary pressure will vary with position in the lung. However, we cannot find measurements of intrapulmonary pressure that record the spatial variation during respiration.

4.3.3 Spontaneous Pneumothorax

As we have seen, we can model flow with spatially inhomogenous external pressure. This enables us to simulate a pneumothorax to the left, right or both lungs.

The inlet pressure profile and all parameters with the exception of external pressure are the same as those used in the quiet respiration simulation. To simulate pneumothorax, we apply the quiet respiration external pressure profile to the lung without the pneumothorax to the large vessels of the lung with the pneumothroax, we apply the profile found in Fig. 4.15e 1 mm Hg and trough of -3 mm Hg.

From the literature, I cannot ascertain how intrapulmonary pressure changes during pneumothorax. However, I assume that as pleural pressure increases, so does intrapulmonary pressure, and that intrapulmonary pressure is always greater than pleural pressure. For the sake of these simulations, I assume that intrapleural pressure is uniformly 5 mm Hg higher than the the pleural pressure.

Left Pneumothorax

Vessels 2, 5, 6, 9 and 10 (Table 4.5) are the vessels of the left lung. To simulate a left pneumothorax, the pneumothorax pressures are applied to these 5 vessels and to the left structured trees. Similarly to the comparison between the normal respiration case and simulation without respiration, we can quantify the difference made by the pneumothorax. The pattern of change from the reference case without external pressure is the same as is shown in Fig. 4.16a, but the change is lower than

in quiet respiration. There is a maximum difference of -19.8 $\mathrm{ml\,s^{-1}}$ as opposed to -32.4 $\mathrm{ml\ s^{-1}}$ seen during quiet respiration. The right pulmonary arterial flow change (Vessel 1) from quiet respiration is at most 0.5 $\mathrm{ml\ s^{-1}}$, where as the change in the left pulmonary artery (Vessel 2) is quiet high with a maximum increase of 12.9 $\mathrm{ml\ s^{-1}}$ over quiet respiration simulation.

For completeness, I also simulate a left pneumothorax, but using the quiet respiratory intrapulmonary pressure. In this case, we still see a difference in flow in the left lung, but it is reduced: flow differs from normal respiration by up to only 3 $\mathrm{ml\ s^{-1}}$; blood pressure varies little between the cases, by up to only 0.23 mm Hg. As we have already seen, small vessel external pressure significantly effects simulated blood flow. From this, it is evident that pressures applied to vascular beds are a strong determinant of the large vessel flow.

Right Pneumothorax

Similarly, I am able to simulate a right pneumothorax. Vessels 1, 3, 4, 7, and 8 (see Table 4.5) supply the right lung with blood. The procedure and analysis are identical to that for the left pneumothorax. The right pneumothorax makes a less striking change to pulmonary flow, with a maximum increase of 4 $\mathrm{ml\,s^{-1}}$ from quiet respiration. This is due to the higher radii and lengths of the right lung vessels giving rise to higher flows.

Simultaneous Right and Left Pneumothoraces

Further, we can simulate simultaneous right and left pneumothoraces by applying the pneumothorax pressures to all vessels in the tree. Here, we see changes of up to 17 $\mathrm{ml\,s^{-1}}$ over quiet respiration.

Limitations

This subsection highlights a key limitation of this model: simulated flow and pressure are highly sensitive to the pressure applied to structured trees, so without reliably measured pressures, the model cannot accurately capture the haemodynamic changes that occur as external pressure varies. Beards & Lipman [115] report that cardiac output drops during pneumothorax, but Hurewitz *et al.* [116] report that cardiac output remains constant, but stroke volume can drop significantly which is compensated for by an increase in heart rate. In the simulation, I vary none of cardiac output, heart rate, or stroke volume.

Kaneda, Nakano & Murakawa [10] give a few examples of change in pleural space pressure during pneumothorax. I presented simulations using only one of these. The pressure profiles I did not use vary in inspiration and expiration gradient and pressure, as well as respiratory rate. We have already seen that flow change depends on inspiration and expiration gradient, so using a different profile would result in a different simulated volume change due to the pneumothorax. However, there are no intrapulmonary pressures given. Intrapulmonary pressure is a more significant driver of change in these simulations than pleural space pressure.

4.3.4 Mechanical Ventilation in Adults

Mechanical ventilation is a clinical intervention in which gas is moved to and from the lungs of a patient using an external device. The objectives of mechanical intervention are diverse; for example, to substitute respiratory effort. Mentzer, Tsuda & Loring [11] measure and report airway and pleural pressures during pressure-cycled mechanical ventilation. During pressure-cycled ventilation, a positive airway pressure is applied and maintained throughout inspiration for a set time period after which

a valve opens and expiration ensues [117]. The positive airway pressure induces a positive pressure in the pleural space.

We can simulate the effect of positive pressure ventilation on large vessel flow and pressure by using the pleural pressure curve given by Mentzer, Tsuda & Loring [11][4]. The original data are not quite periodic, with the final pressure value 0.27 mm Hg above the initial value; to ensure periodicity, I choose to enforce a period of 2.42 s, as the value at this time is 0.03 mm Hg above the initial value, and I reset this final value to be the same as the final value. The original pressure is shown together with the one used in simulations in Fig. 4.17.

I assume that there are exactly four heart-beats (period 0.61 s) per breath ($T = 2.44$ s), so the inlet fluid pressure is four consecutive copies of the inlet profile Fig. 4.1. Finally, we set the intrapulmonary pressure to be uniformly 5 mm Hg greater than the pleural pressure.

In the pressure profile shown in Fig. 4.17, expiration runs from approximately 1 – 2 s, with inspiration occurring before and after this.

As with the previous simulations, I can compare flow and pressure during mechanical ventilation to the reference case with no respiration shown in Fig. 4.18. In inspiration, flow in the MPA is lower than in the reference case. The positive pressures in mechanical ventilation compresses the microvascular vessels, causing flow arterial drops during the inspiratory phase. During expiration, flow is higher than reference flow which may be unrealistic.

[4]Data extracted from the [11, Fig. 3. A2] using WebPlotDigitizer and linearly interpolated to the correct resolution using `interp1q` in MatLab 2018b.

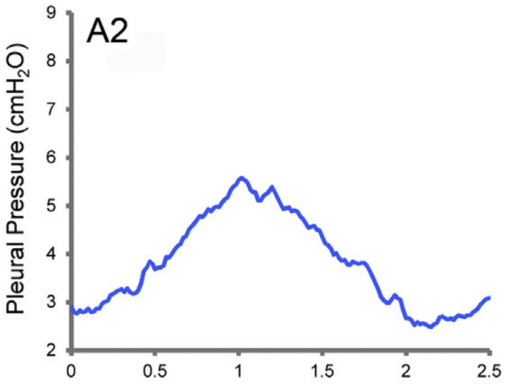

(a) Measured pleural pressure from [11]. Cropped and scaled for use here.

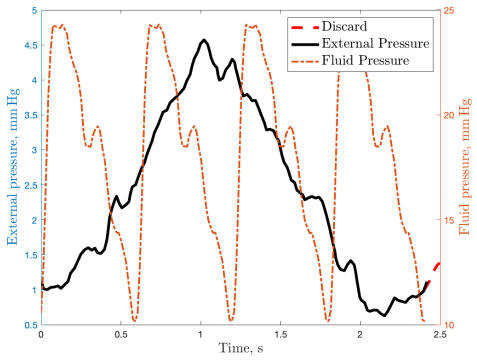

(b) Reproduction of the pleural pressure profile seen in (a) and the inlet pressure profile. The solid black section is periodic and is used in simulations. The dashed red part is discarded to achieve periodicity.

Figure 4.17: Pressure profiles used in mechanical ventilation simulations.

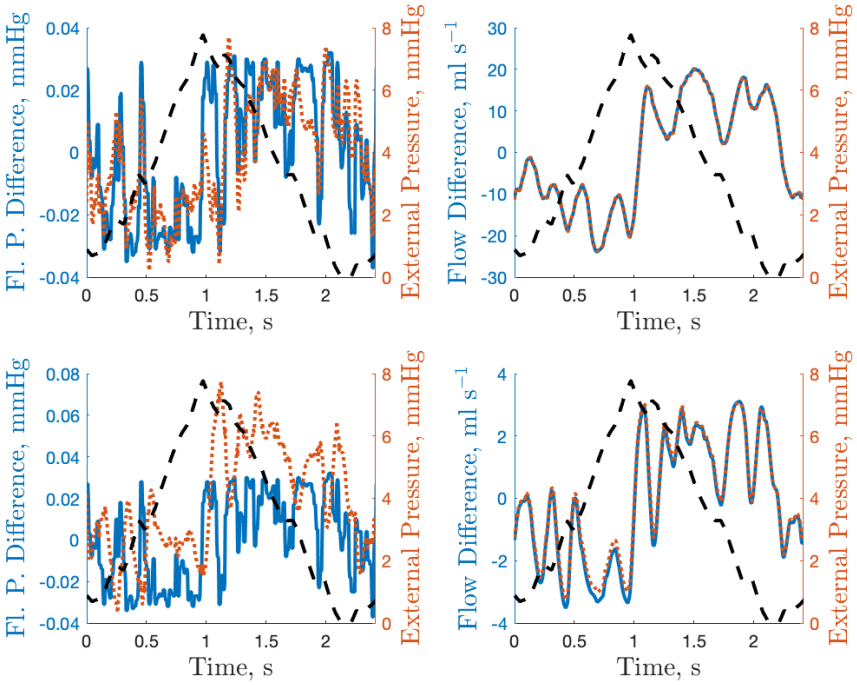

Figure 4.18: Plots of the difference between pressure (left) and flow (right) with and without mechanical respiration in the main pulmonary artery (top) and the left interlobar pulmonary vein. The MPA is Vessel 0 and left interlobar pulmonary vein is Vessel 9 in Table 4.5). Each panel shows the proximal ($x = 0$, solid blue) and distal ($x = L$, dotted orange) difference over one breathing cycle of 8 heart beats of 5.6 s. The intrapulmonary pressure is shown in dashed black, with a scale on the right hand axis for each plot.

4.3.5 Comparison Against Other Models

Quantitative validation is an important step in assessing simulation results. It can be an involved process, as model agreement is best assessed when this model has the same set-up as the model or data against which we are validating, that is, in so far as possible, they use the parameter values, vessel morphometry, and equivalent pressure or flow profiles.

I can preliminarily validate my model against published results from, for example Qureshi [2, 3]. Using a copy of the computational scheme published along with his thesis [3], I am able to simulate the same flow through the same vessel network in both my model and Qureshi's. As my model is an evolution of his, our simulation results in the absence of external pressure are very similar. I find the coefficient of determination $R^2 = 1 - \frac{\sum_i (y_i - f_i)^2}{\sum_i (y_i - \bar{y}_i)}$ between the simulated pressure and flow at all points in all vessels. The flow and pressure from Qureshi's original scheme are the data y, and the predicted values f come from the model presented here. The minimum value that it takes in flow is 0.92 and 0.99 in pressure. This indicates very good agreement between the models. The differences are possibly due to the different inlet boundary conditions we use (Qureshi's model is flow driven, while mine is pressure driven), and that we use different constitutive tube laws, and vascular tree viscosity values (mine is radius-dependent; Qureshi's is constant).

Clipp & Steele [47] investigated the effects of positive and negative ventilation on vascular function using *ex vivo* lamb lungs with steady blood flow. They found significant changes in blood pressure between positive and negative ventilation that this model fails to capture: simulated fluid pressure did not vary by more than 1 mm Hg in any of the pulmonary tree simulations. This discrepancy is possibly due to my use of a pressure, rather than a flow boundary condition to drive simulations.

Further research is needed to investigate such boundary conditions when simulating external pressure effects. Using the model presented in this thesis, it is possible to simulate steady flow throughout a network that is subject to some external pressure. Recreating the pressure changes during ventilation seen by Clipp & Steele may be an interesting area of future research. Careful thought will have to be given to the vessel morphometry and parameter values used in these simulations.

Burton & Patel [118] measured the change in the MPA of excised rabbit lungs with the application of positive and negative pressures. They found that pulmonary resistance (the ratio of flow to pressure) varies throughout the respiratory cycle. They report a drop in MPA flow as the lungs are forced open during positive pressure ventilation, and that flow increases with increasingly large negative inflation pressure. These changes are the same as we observe here, as are the flow changes reported by Klabunde [112] discussed above.

4.4 Summary, Limitations, and Future Directions

4.4.1 Summary

In this chapter, I discussed the parameters that must be set in the model. All of these are measurable, but likely vary between organ, individual, and species. For instance, the constitutive parameters used to define wall stiffness, scaling factors and length-to-radius ratio used to define the structured trees, and characteristic radius vary between organs.

I presented some simulation results in toy trees, showing that the simulated behaviour is well aligned with our intuition and is also self consistent. For example, when vessels in the structured tree are compressed, upstream flow is reduced, and

downstream flow increases as fluid is squeezed from the small vessels. We saw that the stenotic, bifurcating, and trifurcating junctions in large vessels are volume preserving and that one-to-many junctions split flow evenly between daughter branches. Spatially inhomogeneous external pressures can impact the simulation results throughout the tree.

External pressure gradient seems to play an important role in simulation outcome, and pressures applied to structured trees have a large impact simulation results.

Finally, I set a series of pressure driven pulmonary simulations to investigate quiet respiration, pneumothorax, and positive pressure ventilation. The simulated change induced by respiration qualitatively agrees with reports from the literature. Finally, I showed that without respiration, this model performs very similarly to Qureshi's [2, 3].

4.4.2 Limitations

A key limitation and frustration of this work is the need for pressure or flow profiles to use in simulations. Ideally, the required morphometry, parameter values, pressure, and flow measurements would all come from a single individual. However, such a dataset appears not to exist in the literature. Instead, we make do with a amalgam of data from various sources. The work presented here is intended as a proof of concept: respiration induces measurable changes in pulmonary haemodynamics that can be captured by this model.

Throughout the chapter, I have highlighted other limitations. These include: the lack of cardiopulmonary feedback; the model is pressure driven where as the pulmonary system may be better served with a flow-driven model; the use of constant left atrial pressure.

The inclusion of true cardiopulmonary feedback is far beyond the scope of this thesis but would be a fruitful area for research. Such a model may involve coupled models for pulmonary perfusion, ventilation, and cardiac output. A possible step forward could be to develop a flow-driven model that simulates over much longer time scales; the inlet data in such a model could encode a variable heart rate and stroke volume.

We use a pressure based outlet boundary condition of a constant 2 mm Hg in the left atrium. Model realism could be improved in the future by using a time-dependent outlet condition. I have not used such a profile here as this may have confounded the interpretation of simulation results.

Chapter 5

Coronary Modelling

In this chapter, I begin by discussing the morphometry of coronary vasculature and establishing procedures with which we build coronary trees. I then discuss the parameter values and boundary conditions we use in the model of the healthy coronary vasculature. Finally, we investigate the impact of network morphometry, junction choices, parameter values, and external pressure on simulated flow and pressure. This includes preliminary model validation against data from the literature as well as other modelling studies. I conclude by suggesting directions for future research.

5.1 Coronary Vasculature

5.1.1 Left Coronary Arterial Anatomy

The coronary vasculature supplies the myocardium – the heart muscle – with blood. As can be seen in the illustration Fig. 5.1, the left and right-coronary arteries arise from the aorta just above the aortic valve [119]. The left coronary artery (LCA) bifurcates into the left anterior descending (LAD) and left circumflex (LCx) arteries.

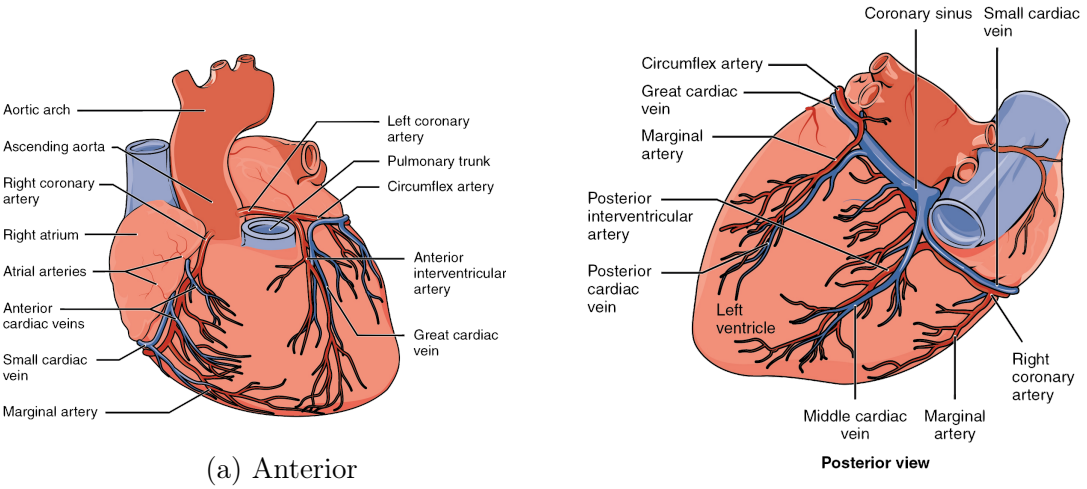

(a) Anterior

(b) Posterior

Figure 5.1: Illustration of the coronary blood vessels, OpenStax College, CC BY 3.0.

The LAD courses the interventricular groove, while the LCx lies along the seam between the left atrium and ventricle. Occasionally, the LAD exhibits a trifurcation, in which case the central daughter is the left intermediate artery [12]. The main branches lie on the epicaridal surface, as do some daughters. Many daughter branches penetrate the epicardial surface to perfuse the left ventricular wall.

Left Coronary Arterial Vascular Data

From Dr. Jack Lee (King's College London) we have data that represent a left coronary arterial tree and left ventricle from a single porcine heart [120,121] reconstructed from *ex vivo* cryomicrotome imaging studies [122]. There is a high degree of similarity between porcine and human coronary anatomy and heamodynamics [123, 124].

The data for the vasculature consist of spatial nodes that lie approximately on the centrelines of vessels. Each node has an associated radius between 0.1035 and 1.7059 mm. There is a list of edges consisting of pairs of nodes that are joined by

straight lines. The edges have lengths between 1.02 mm and 0.1 mm. The point cloud is visualised with a lateral view in Fig. 5.2a, whereas Fig. 5.2b shows only the nodes with radius > 0.22 mm (the mean) which have been scaled to reflect their radii relative to each other. In general vessel radius decreases with increasing distance from the inlet.

There is also a ventricular mesh (seen in Fig. 5.2c and Fig. 5.2d) which is used here to aid in the visualisation of small portions of the tree.

Paths, Segmentation, and Sorting

From the vascular data, our collaborator Megan Chambers (North Carolina State University), created a list for each node that detail the nodes between the inlet node (given) and the target node. These are called *paths*, an example of a path is shown together with the ventricle in Fig. 5.2c. She also found that 41 nodes of 17945 (0.23%) are unreachable from the inlet node; we discard these disconnected nodes without effecting the overall morphometry. Disconnected nodes arise from limitations in imaging techniques.

In the computational scheme, we build large vessel networks using sections of vessels that are joined together by junctions. So, in order to use these data to build a large vessel network, we need to separate the paths into segments that lie between junctions, or between a junction and a terminal node. Terminal nodes appear in the list of edges exactly once, nodes within a vessel (between junctions or a junction and a terminus) must appear exactly twice. All other nodes are junction nodes. By comparing the list of junction nodes and each path to a terminal node, we can create segments. Segments are lists of nodes that begin at one junction and end at the following one. Suppose $\{a, b, c, d, e, f, g\}$ is a path from node a to g, if node e were a

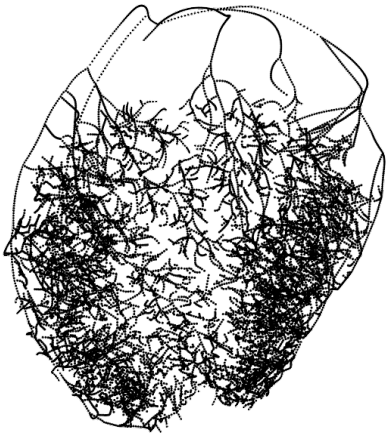

(a) A lateral view of all nodes in the the left coronary arterial tree point cloud.

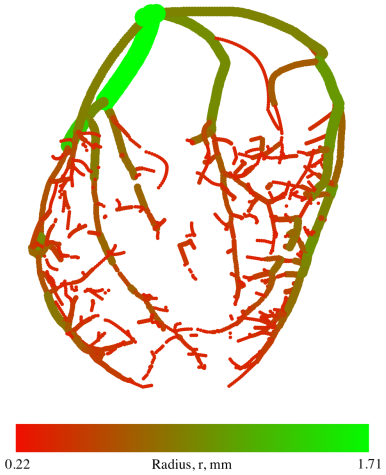

(b) The vascular nodes with radius above 0.22 mm which have been scaled and coloured to indicate vessel radius.

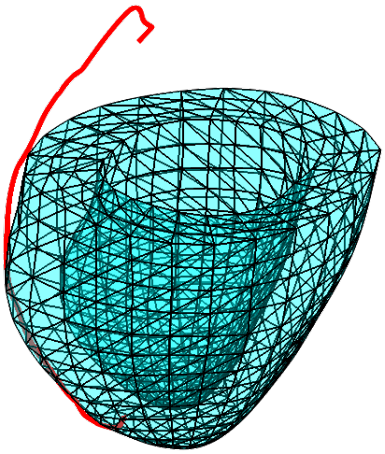

(c) An example of a path running from the inlet to its target node.

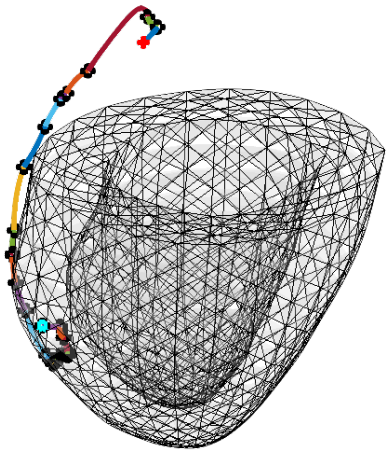

(d) Segmented path from to the inlet (red plus) a terminal node (red circle) with junctions highlighted by black circles.

Figure 5.2: Plots of the porcine vascular and ventricular data.

junction, the path would be divided into two segments $\{a, b, d, e\}$, $\{e, f, g\}$. We now have segments that take us from a to e and from e to g. The algorithm I developed for this procedure is given in Algorithm 2.

For later use, it is convenient to sort the segments into generations. To do so, we choose the inlet node (marked in red in Fig. 5.2d), the segment that starts with this node is generation 0. To find all subsequent generations, list the final nodes of the previous generation, and search the unsorted node collection for segments that begin with these. Stop once the desired number of generations has been reached.

Pseudo-Trifurcations

There are many vessel segments in that contain only two nodes. These are the final node of the parent vessel and the first node of the vessel they branch into. In effect, a trifurcation is represented as two subsequent bifurcations. The length of the short segments joining two bifurcations varies between 1 and 0.1 mm. I call these junctions pseudo-trifurcations, and we wish to model them with a trifurcation, as including very short vessels in the computational model can increase computational costs due to the small spatial and time steps needed to resolve pressure and flow adequately.

We want all segments that arise from a pseudo-trifurcation to arise from the same node. To achieve this, replace the first node in the daughters of the short segment with the first node of the long daughter. The difference between a pseudo-trifurcation and a true trifurcation can be seen in Fig. 5.3.

Mercator Projections

The vascular tree and ventricle data are in 3D. All representations of this data in this thesis are necessarily 2D projections. While I can endeavour to consistently present

Algorithm 2: Create and sort segments

Result: Vessel segments

Input: Terminal node paths, list of junction nodes

Set $k = 1$

for (each path)

- Find the position of the junction nodes in the path
- Append the terminal node to the list of junction nodes in the path
- for (a subsequent pair of indices in list *i, j*)
  - Create a list of the nodes from and including i to j. These are the segments.
  - A path containing n junction nodes will be split into $n + 1$ segments.

Remove duplicate segments from the collection.

Find the path containing a single node. Store it in the 0-th generation. It is the inlet path.

Define the desired number of generations, n

for (*Each generation, n*)

- for (*Each path*)
  - If the path begins with the final node of any path generation $n - 1$, store it in generation n

(a) Pseudo-trifurcation: a trifurcation is formed of two subsequent bifurcations in quick succession.

(b) True trifurcation: all daughters arise from the same node and are in the same generation.

Figure 5.3: A visual comparison between a pseudo- and a true trifurcation. Different generations are represented by different colours.

this data from a fixed view, it is not always easy to see the branching structure of the networks with such a view. I seek to display the networks in a way that is consistent and easy to interpret.

A Mercator projection [125] is a specific kind of 2D projection of a 3D objects, most often seen in world maps. In a Mercator projection, the spatial points on the 3D object we wish to visualise are mapped to the surface of a cylinder in such a way that their latitude and longitude are preserved, and the cylinder is "unwrapped" to form the flat plane, where the angle between each point and the positive direction of the x-axis becomes its horizontal coordinate. Explicitly,

$$(x, y, z) \mapsto \left(\frac{x}{\sqrt{x^2 + y^2}}, \frac{y}{\sqrt{x^2 + y^2}}, z \right) \mapsto (\theta, z)\,,$$

where

$$\theta = \begin{cases} \arctan \frac{y}{x}, & x, y \geq 0 \\ \arctan \frac{y}{x} + \pi, & x < 0 \\ \arctan \frac{y}{x} + 2\pi, & x \geq 0, y < 0 \end{cases}$$

Figure 5.4: The first five generations of vessels within the vascular tree shown with a top-down view (left) and Mercator projection (right). Each generation of vessels is shown in a different colour.

The Mercator projection preserves the branching relationship between vessels, but not the length of vessels.

Radius Truncation Condition

There are many more vessel segments represented by the data than we wish to include in the large vessel tree. Here, I develop a radius based truncation condition for the data to produce trees in which we will simulate blood flow. There are many possible truncation condition choices, such as by vessel length, distance from the ventricle wall, generation number of Strahler order (discussed more later), and total terminal vessel outlet area. We use a radius based truncation condition, as it is straight forward to implement.

There are several ways to implement a radius based truncation condition. The most straight forward is to check the radius at the final point in all segments, and only include the segment if the condition is met. However, this makes the generated

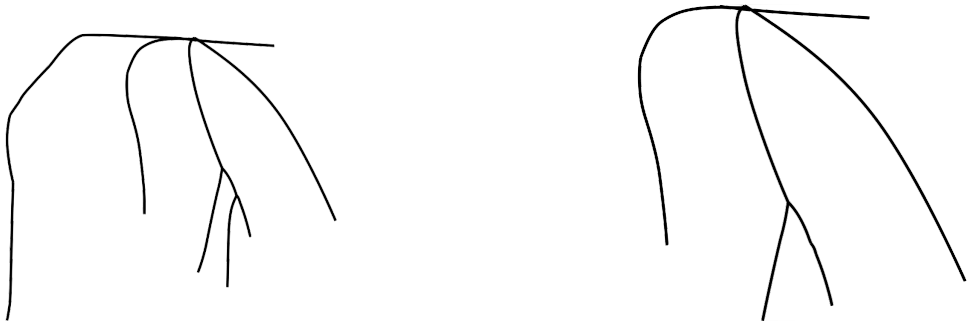

(a) Mean Radius Condition. (b) Final Node Radius Condition.

Figure 5.5: A comparison of radius truncation conditions.

trees sensitive to errors in radius measurement. Instead, we opt for a mean radius condition. If the mean radius in a segment exceeds a prescribed threshold, then it is eligible for inclusion. The trees created using these truncation conditions differ greatly from each other. A pair of sample trees can be seen in Fig. 5.5. For a minimum radius of 700 µm, the trifurcating tree with the mean radius condition has 21 segments, while the tree with the end point radius condition has only 11.

Regardless of the radius truncation condition we use, we must ensure that all segments in the tree are reachable from the inlet segment. After finding the segments that are eligible for inclusion in the tree, we need to know if any of these are disconnected from the inlet. Disconnected segments will have an initial node that is not found else where in the tree, so are easy to search for and can be discarded. Figure 5.6 shows all nodes with radius > 0.7 mm; in these figures, I have highlight the segments in which all nodes exceed the radius bound (a), the segments in which the mean radius truncation condition is met (b), and the segments that meet the truncation condition but are not connected to the inlet (c). We discard the segments that are not connected to the inlet which results in the trees show in Fig. 5.5.

(a) All nodes in the highlighted segments have radius > 0.7 mm.

(b) Mean radius in highlighted segments is > 0.7 mm.

(c) Highlights show the eligible segments that are disconnected from the inlet.

Figure 5.6: Nodes with radius > 0.7 mm are shown in black points. The panels highlight segments of in the tree (a) in which all nodes > 0.7 mm, (b) mean radius > 0.7 mm, (c) disconnected segments to discard.

In addition to the mean radius truncation condition, we are able to specify the maximum number of generations permissible in a tree. However, the tree is made of several vessel segments joined in series with each other (see Fig. 5.7a). While we can include these monofurcatinging junctions in the computational scheme (and indeed do), it is convenient to join series segments to form vessel elements that are then included in the computational scheme, as longer vessels are easier to simulate fluid flow in due to spatial resolution constraints. A vessel element is defined as two or more vessel segments joined together in series. A tree composed of joined segments can contain as much morphometric information as one that includes elements, but the greater number of junctions will lead to increased computational times. Figure 5.7a shows a tree of segments and Fig. 5.7b the equivalent tree with segments joined to form elements.

In Fig. 5.7b, we can see an apparent monofurcation between two vessels, however, this is actually a bifurcation in which the other daughter contains 3 nodes (1.46 mm) and is too short to see clearly. As mentioned above, and as we will discuss later, very

(a) Unjoined segments. (b) Joined segments. (c) Short segment is removed.

Figure 5.7: Trees of 5 generations with monofurcations, without monofurcations, and with outliers removed. Segments of the same colour belong to the same generation.

short vessels require high spatial and temporal resolutions in order to simulate fluid flow through them. For this reason, we may wish to remove terminal vessels that are significantly shorter than the other terminal vessels. A terminal vessels is deemed to be significantly smaller than the others if it has arclength in the 10th percentile.

There is a short vessel in Fig. 5.7b that is too small to be seen clearly. It is in the 7th percentile for both arc-length and node count. We remove it and join the up and downstream vessel elements to form one larger element that can be see in the extreme left of Fig. 5.7c.

Interpretations of the Tree

By comparing the generated left coronary tree and ventricle against images and descriptions from the literature, we can name the major vessels, as is done in Fig. 5.8. The left arterial network features three branches of the LCA. These are the LAD, intermediate artery, and left circumflex.

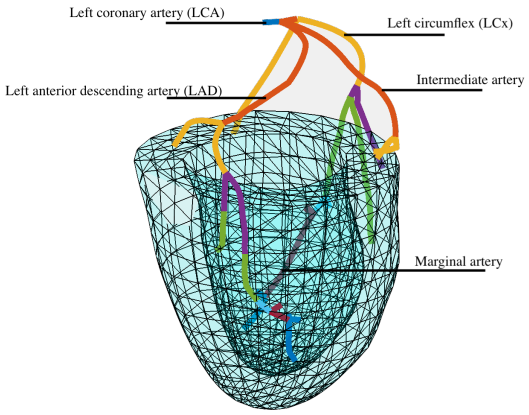

Figure 5.8: Generated left coronary arterial tree with minimum radius 0.5 mm and 8 generations relative to the left ventricle

Summary

From the point cloud seen in Fig. 5.2a, lists of edges, and paths to each node, I have developed a number of algorithms implemented in MATLAB that segment and sort the data. These functions allow us to generate left coronary trees with a prescribed maximal number of generations and minimum radius value. The trees generated can either contain only bifurcations or any kind of large vessel junction.

5.1.2 Right-Coronary Tree

We have access to the 3D discussed above. However, we have no such data for the right-coronary tree or for the venous network. If such data were available, they could also be used to construct right arterial and venous trees, as was done for the left. In order to simulate blood flow in the whole coronary tree, we need large vessel networks for the right-coronary arterial system, and for the venous network.

The right coronary artery (RCA) typically arises from the aorta at the other side

from, but at the same level as the LCA. It commonly gives rise to the posterior interventricular artery (PIVA) and marginal branches (see Fig. 5.1). The RCA descends towards the apex along the right atrioventricular groove, curving posteriorly giving off two or three branches as it goes [126].

For simplicity, we assume that the left and right trees are morphometrically similar, but all trifurcations are replaced by two subsequent bifurcations. That is, use the same branching pattern in the right and left trees. I assume that the marginal branches of the RCA are analogous to the diagonal branches of the LAD, and that the LCx is analogous to the PIVA. This assumption should be revisited in patient specific models, or if more network data becomes available. Although we assume the branching structures are identical, we do not assume that the lengths and radii are the same. These are set with reference to the literature.

This method of constructing a right-coronary artery tree is not ideal. Weaver *et al.* [124] report that porcine and human left coronary arteries are larger in length and diameter than the right-coronary artery. Further, this procedure leads to a balanced vasculature, in which the left and right trees carry approximately the same blood volume, which occurs in only 17% of porcine hearts [124].

Kaimovitz, Lanir & Kassab [127, 128] performed a large scale stochastic reconstruction of the coronary arterial trees. The reconstruction is initally performed on a rectangular slab by means of a global geometric optimization of the vessels. Once complete, the slab and the vessels it contains were mapped onto a prolate spheroid geometry of the heart in order to reconstruct the trees. Such a reconstruction is outwith the scope of this thesis.

5.1.3 Venous Tree

Capillary flows either return via the cardiac veins or the Thebesian vessles. The largest cardiac vein is the coronary sinus (CS), an epicardial vessel that drains into the right atrium. According to Issa, Miller & Zipes [129], there are commonly five first-order tribrutaries of the CS. These are the small cardiac vein, middle cardiac vein, inferior vein of the left ventricle, great cardiac vein, and the oblique vein of the left atrium (OVLA). The small and middle cardiac veins drain the right arterial tree [130, 131]. The middle cardiac vein drains the PIVA and the interventricular septum. These join the CS near its outlet into the right atrium. The CS arises at the confluence of the OVLA and the great cardiac vein. The OVLA itself has two main tributaries: the large left marginal vein, and the posterior cardiac vein of the left ventricle [132]. These latter three vessels (and tributaries) drain the left arterial tree. The anterior interventricular vein drains the anterior wall of the left ventricle and the interventricular septum. Its course is similar to the adjacent LAD. It turns left ward and posteriorly, tracing the course of the LCx and becomes the GCV [129, 131]. It is the largest and most consistent of the cardiac veins [131], and was found in 100 % of patients by Schaffler *et al.* [132]. An illustration of the epicardial vessels can be seen in Fig. 5.1.

The Thebesian venous network is comprised of small venous branches that drain the sub-endocardium (the myocardium not including the epicardium) directly into any of the four chambers, but are more prevalent in the right heart than left and in the atria than the ventricles [129]. Their distal radii are commonly $< 0.25\,\text{mm}$ [133], and have a maxium radius of $0.7\,\text{mm}$ [5] and carry approximately 10% of the venous blood volume.

Kassab and colleagues [4, 5, 7, 12] give details of the length and radius of coro-

nary arterial and venous segments in terms of a Diameter Defined Strahler Order. This is an ordering system that assigns integer order numbers (O.) to vessels with a modification to ensure that successive orders do not overlap. In an unmodified Strahler scheme, when two vessels of different orders converge, the resulting segment has the large of the two orders, but when segments of the same order converge, the resultant's order is one more than that of the daughters. Kassab *et al.* [4] introduced the rule that when two segments of different order meet, the order of the resultant vessel increases if and only if its diameter is greater than those of the converging vessels by a specified amount. Arterial order numbers range from O.0a (arterial side capillaries) to O.11a in the RCA, and from O.0v to O.12v in the venous side. Strahler ordering is important as it provides us with a useful guide to aid in the construction of trees and to evaluate their similarity against organic arterial and venous trees.

All arteries and veins that are matched over the structured tree must have the same distal radius. Because of this constraint, and the radius ranges of each vessel order, we must ensure that an artery of given order is matched to a vein of the same order.

Hence, we must start building a venous tree by determining the Strahler order of the terminal arteries. We find these by comparing the distal radius against the range given by Kassab *et al.* [4], and pictured in Fig. 5.9.

The right-coronary tree drains into the CS closer to its ostium than the left branches. So, we aim to build a venous tree that drains the left coronary branches more distally than the right branches. The CS has five main tributaries, so begin by creating a CS trunk of 4 segments with 3 branches arising along its length and a further 2 at the distal end, as is pictured in Fig. 5.10. To the five branches, add pairs of daughters from the distal to proximal end until the desired number of terminal segments is reached. The first row of additional daughters will result in 10

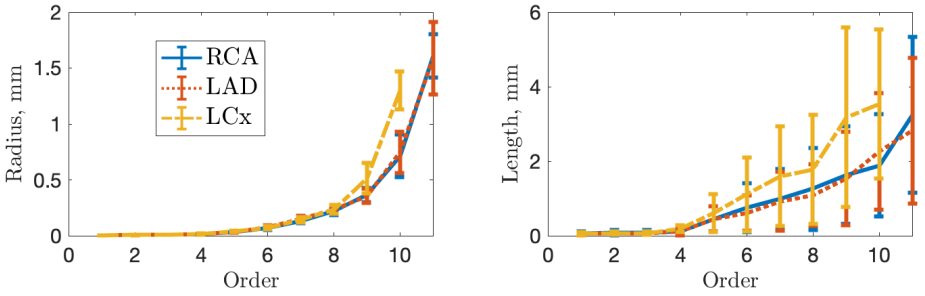

Figure 5.9: Radius and length ranges for each vessel order from Kassab *et al.* [4].

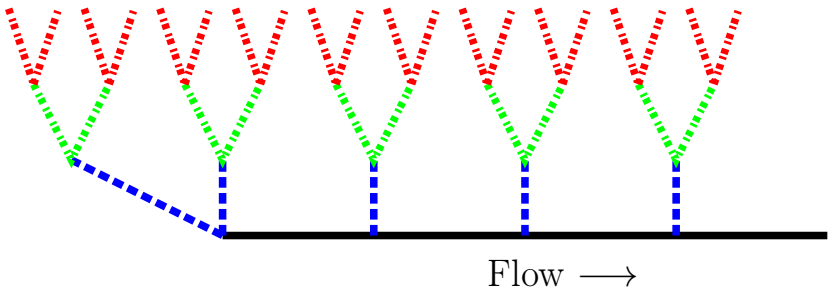

Figure 5.10: Schematic of the cardiac veins and coronary sinus. The solid black trunk is the CS, with five tributaries shown in blue. Following generations are shown in green and red. Pairs of vessels are added from left to right. Red segments can only be added after all 10 green segments. Further generations can be added if needed, but are not pictured here.

terminal segments. If more than 10 terminal segments are needed, an additional row of daughters is started from the distal end.

A terminal vein of length L must have same distal radius $r_0(L)$ as the artery to which it is matched. Further, the length $L \geq 4r_0(L)$ to ensure sufficient spatial points within each vessel. Each terminal vein is given the Strahler order of the artery from which it arises. If the distal radius $r_0(L)$ lies outwith the range given by Kassab *et al.* [4], the closer order is assigned. Once all the terminal veins have an order number,

Order	9	10	11	12
Radius range (mm)	0.36 – 0.42	0.54 – 0.63	0.67 – 1.13	2.96 – 2.96
Length range (mm)	0.96 – 11.18	1.88 – 18.52	1.60 – 50.00	71.90 – 71.90

Table 5.1: Radius and length ranges for the largest 4 orders of porcine coronary venous elements from Kassab *et al.* [7]. Kassab *et al.* define an element as two or more segments of the same order that lie end to end.

all other segments in the tree are given an order using an unmodified Strahler scheme. The total length of segments of O.12 is 71.9 mm. For simplicity, we divide this length evenly between the O.12 segments. Another possible approach would be to divide vein so that each of the segments has the same length-to-radius ratio. Further, the distal radius of a O.12 segment is the proximal radius of the following segment. The range of O.12 radii is 1.783 – 4.14 mm. All other segments are assigned a length and radius based on the order number. The order based ranges for venous segment radius and length come from Kassab *et al.* 's values for elements [7] and are given in Table 5.1. The distal radius of a bifurcating vessel must be at least as large as the proximal radius of the larger daughter. We use the ranges for elements, as these are equivalent to the segments discussed here.

A Specific Example

Generate a trifurcating left tree in which all vessels have mean radius $> 800\,\mu$m. This tree contains 8 vessels, including 5 terminal segments, and is shown in Fig. 5.11. The right tree has the same truncation condition, but all trifurcations are modelled by two successive bifurcations. This tree also has 6 terminal segments. The summary tables for the right and left trees are given in Table 5.2.

Vessel	Length (mm)	Proximal radius (mm)	Distal radius (mm)	D1	D2	D3	V	O.
0	8.3	1.8	1.4	1	2	3		11
1	7.5	1.4	1.1	4	5			11
2	44.7	1.4	0.9				33	10
3	87.2	1.4	0.7				32	10
4	35.7	1.1	0.8				30	10
5	31.7	1.5	1.5	6	7			11
6	18.2	1.5	0.7				34	10
7	7.9	1.5	0.9				35	10
8	8.3	1.8	1.4	9	10			11
9	7.5	1.4	0.8	11	12		11	
10	87.2	1.4	0.7				31	10
11	7.8	1.1	1.1	13	14			11
12	44.5	0.9	0.9				26	10
13	35.7	1.1	0.8	15	16			11
14	31.7	1.5	1.5				23	10
15	18.2	1.5	0.7				27	10
16	7.9	1.5	0.9				22	10

Table 5.2: Summary tables listing the length, proximal and distal radii, row number of the daughters (D1, D2, D3), and order of all arteries in the left (segments 0 – 9) and right (10 – 20) arterial trees. Trifurcations have tree values (D1, D2, D3), whereas bifurcations only have two (D1, D2). Column V indicates the vein to which the terminal arteries are joined, see Table 5.3

Figure 5.11: Arterial side of the tree with mean truncation radius 800 µm.

Using the method described above, of creating a CS trunk with five tributaries and adding further tributaries until the desired number of terminal vessels is reached, we create the venous side shown in Fig. 5.12 along with the arterial trees.

There are 10 terminal arteries in total. Each of the 10 terminal veins inherits their distal radii from the arteries to which they are joined. In this example, all terminal radii correspond to venous O.11. Figure 5.12 shows the full two-sided tree constructed using the method described above. The venous summary table is given in Table 5.3. The length and radii of the terminal veins is determined first using the distal radius of terminal arteries.

The segments of O.12 have total length of 79.1 mm which is divided equally between them. In this case there are 4 vessels. The proximal radius of the CS must be 4.1 mm and the distal radius of the final O.12 segment is 1.8 mm. The distal radius of an O.12 segment gives the proximal radius of the following segment. To find the proximal and distal radius, linearly space the range 1.8 – 4.1 to n+1 values, where $n \in \mathbb{Z}$ is the number of O.12 segments.

The remaining segments are within the body of the tree. Each has a known order, and their lengths and radii are assigned based on the ranges given in Table 5.1.

5.1.4 Variations

I have described the coronary vasculature in general, but network structure varies between individuals and between species. Below, I discuss some common variations in coronary vascular morphometry. Kastellanos *et al.* [134] give a good overview of typical coronary vascular anatomy, and of the common variations.

Dominance

The PIVA typically supplies blood to the basal and posterior third of the interventricular septum, the atrioventricular nodal artery (AVNA) and the posterolateral left ventricular artery (PLVA). These arteries supply blood to the atrioventricular node and inferior portion of the myocardium. If the PDA, atrioventricular nodal artery, and posterolateral left ventricular artery all arise from the RCA, the system is said to be right-dominant [119]. This is the case for 70 – 85 % of people [119, 134, 135]. If these vessels arise from the LCA, the system is left dominant, and is the case for approximately 5 – 10% of people. In the remaining 10 – 25 % the arteries arises from both trees — they are co-dominant. This is illustrated in Figure 5.13.

Trifurcations

Trifurcations (one parent vessel branching into three daughters) account for up to 14.5% of left coronary arterial tree junctions [91]. Further, the left coronary arterial tree exhibits a trifurcation as the first junction in 31% of networks — such a trifurcation gives rise to the *ramus intermedius* or intermediate branches in addition to

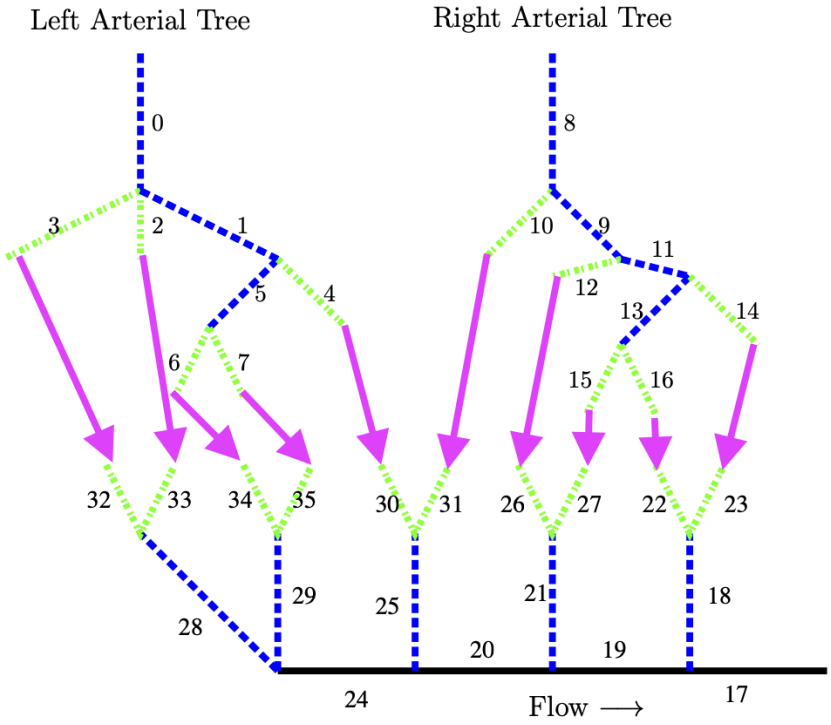

Figure 5.12: Schematic showing the branching pattern of the full coronary tree with minimum mean radius 800 µm. Green dot-dash segments are O.10, blue dashed segments are O.11, and solid black segments are O.12. Arterial and venous terminal segments are joined via structured trees indicated by magenta arrows. Each segment is labelled, and these correspond to the vessel number in the summary Tables 5.2 and 5.3.

Vessel	Length (mm)	Proximal radius (mm)	Distal radius (mm)	D1	D2	O.
17	19.775	4.1	3.7	18	19	12
18	19.775	3.7	3.2	22	23	11
19	25.8	0.9	0.9	20	21	12
20	19.775	3.2	2.7	24	25	12
21	25.8	1.0	1.0	26	27	11
22	3.2	0.8	0.8			10
23	3.2	0.8	0.8			10
24	19.775	2.7	2.5	28	29	12
25	25.8	0.9	0.9	30	31	11
26	2.8	0.7	0.7			10
27	4.0	1.0	1.0			10
28	25.8	0.9	0.9	32	33	11
29	25.8	0.9	0.9	34	35	11
30	2.8	0.7	0.7			10
31	2.8	0.7	0.7			10
32	2.8	0.7	0.7			10
33	2.8	0.7	0.7			10
34	2.8	0.7	0.7			10
35	2.8	0.7	0.7			10

Table 5.3: Summary tables listing the length, proximal and distal radii, daughters, and order of venous tree shown in Fig. 5.12. D1 and D2 indicate the vessel to which a segment branches. The Strahler order of each element is given the final column.

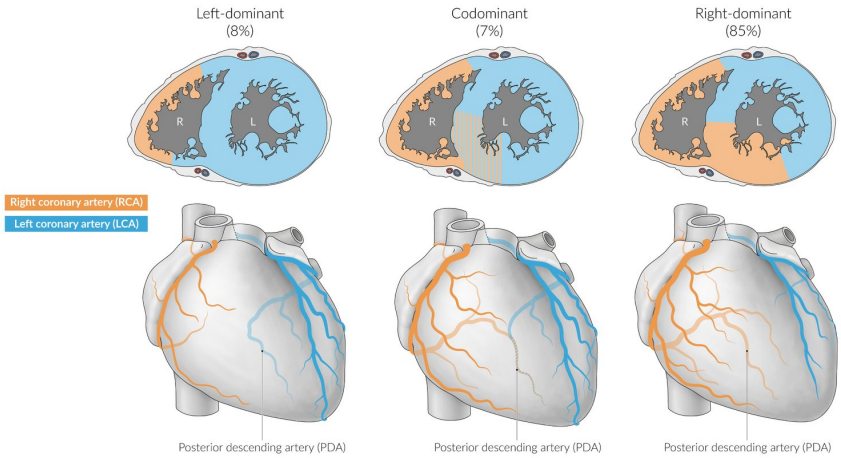

Figure 5.13: Axial illustrations of the human heart showing the distribution of coronary arteries supplying different areas of the heart wall. The left most figure shows a left dominant heart, the central figure a co-dominant heart, and the right most a right dominant heart. From amboss.com/us/knowledge/Heart/. Accessed online 24 Aug. 2021.

the left anterior descending and circumflex arteries that are usually present.

Other Anatomical Variations

Not all blood vessels run in the typical locations or drain into the expected vessel. Habib *et al.* [131] report that in approximately 25% of patients, the posterior ventricular vein and the middle cardiac vein share an ostium into the CS. This constitutes a venous trifurcation. The small cardiac vein typically drains into the CS, but has also been found to drain into the right atrium and the middle cardiac vein, or be absent altogether [136]. The oblique vein of the left atrium is present in up to 95% of individuals, it can also be completely fibrotic forming the ligament of Marshall [137].

Myocardial Bridging

The myocardial bridge is an anomaly in which an epicardial vessel is routed beneath a bridge of myocardial tissue. In such anomalies, the buried vessel portion will be subject to unusually high external pressures.

5.1.5 A Note on Nomenclature

There is no central authority that regulates the naming of arteries, so vessel names vary between publications. For instance, the left coronary artery is also called the left common coronary artery [12], left main coronary artery [119] and sometimes as the left main stem coronary artery [134]. We have tried to eliminate errors arising from this source of confusion. Here, we aim for internal consistency. The left anterior descending is also called the anterior interventricular artery.

5.2 Parameter choices

Constitutive parameters We must establish values for k_1, k_2, k_3 that govern vessel wall stiffness in

$$\frac{Eh}{r_0} = k_1 \exp(k_2 r_0) + k_3, \tag{5.1}$$

where E is Young's modulus, h is wall thickness, and $r_0(x)$ the reference configuration radius. Compliance

$$C = \frac{\partial A}{\partial \varphi} = \frac{\partial}{\partial \varphi}\left(A_0\left(\frac{\varphi}{f}+1\right)^2\right) = 2\frac{A_0}{f}\left(\frac{\varphi}{f}+1\right), \quad \text{where } f = \frac{4}{3}\frac{Eh}{r_0}$$

is an elastic body's ability to distend under pressure. Kassab & Molloi [8] investigated the relationship between porcine coronary arterial cross-sectional area and pressure over a range of vessel radii. The data are measured *in situ*, hence are influenced by vessel tethering to adjacent tissues. The resulting data can be seen in Fig. 5.14b. We find the compliance of each vessel by least squares fitting a straight line $A = Cp + b$ to the data in each curve in the physiological pressure range 60 – 160mm Hg with constants $C, b \in \mathbb{R}$. The compliance for a particular vessel is the gradient of the fitted line. The compliance values are given in Table 5.4 and are used to find the parameters in the stiffness relation. The stiffness

$$\frac{Eh}{r_0} = A_0 \frac{3}{4} \frac{1 + \sqrt{1 + 2\frac{C\varphi}{A_0}}}{C}, \; Eh/r_0 > 0$$

is found by rearranging the expression for C and setting $\varphi \in [60, 160]$ mm Hg in the physiological range. The values for C and Eh/r_0 for vessels of diameter between 2.8 mm and 1.0 mm are given in Table 5.4. From this table, we can see that the goodness of fit decreases with vessel size, this is due to the relative experimental error increasing with decreasing vessel size. Vessels with diameter 2.4 – 1.2 mm

Diameter (mm)	C (mm^2/mmHg)	Eh/r_0(Pa)	R^2
2.8	5.6×10^{-3}	3.06×10^5	0.90
2.4	7.1×10^{-3}	1.83×10^5	0.87
2.0	4.3×10^{-3}	2.06×10^5	0.82
1.6	2.7×10^{-3}	2.08×10^5	0.75
1.3	1.2×10^{-3}	3.12×10^5	0.74
1.2	1.1×10^{-3}	3.00×10^5	0.62
1.0	1.45×10^{-3}	1.57×10^5	0.72
8.9	1.75×10^{-3}	1.07×10^5	0.85
7.4	1.37×10^{-3}	0.96×10^5	0.55

Table 5.4: Compliance C, stiffness and value for vessels of given diameter from Kassab & Molloi [8]. The goodness of fit of lines to the data seen in Fig. 5.14b with $R^2 = 1-(\sum_i(y_i-g_i)^2)/(\sum_i(y_i-\bar{y})^2)$ values given in the fourth column, for a model g and data y. Stiffness is evaluated at 100 mm Hg.

show decreasing vessel compliance with diameter. Vessels of diameter 1 mm and less, indicating a structure change in the wall [138]. Further, in general we see that, except for the largest vessels, compliance decreases with vessel size and stiffness increases.

Hence, set $k_1 = 0$ Pa and $k_3 = 2.53\times10^5$ Pa for $\varphi = 100$ mm Hg, the mean stiffness. When $k_1 = 0$, the choice of k_2 is arbitrary. The value of k_3 depends on the choice of φ. In the physiological range 60 – 100 mm Hg $k_3 \in [2.48\times10^5, 2.60\times10^5]$ Pa. This is about 3 times larger than the systemic arterial stiffness 8.65×10^4Pa [29], and about ten times larger than the pulmonary arterial stiffness value used in the previous chapter and by Qureshi [3]. Vessel compliance varies between organs, individuals, and species, as well as with vessel size and age [139]. Further, large arterial stiffening

has been correlated to an increase in adverse cardiovascular events [140]. Further research is needed to refine the coronary arterial stiffness parameters in health and disease. Van Andel, Pistecky & Borst [141] measured the compliance of *ex vivo* porcine and human inframamary arteries and coronary arteries. They found that finding that systemic arteries are more compliant (in both swine and humans) than coronary arteries, and that porcine arteries can be up to three times more compliant than human arteries with similar diameters, wall thicknesses and functions. Relative to radius, coronary fluid pressure is higher than systemic fluid pressure, so it is reasonable that coronary vessels would be stiffer than their systemic counterparts.

The smallest two vessel diameters investigate by Kassab & Molloi [8] have stiffnesses of 1.1×10^5 Pa and 0.96×10^5 Pa, respectively. Again, there is not enought data to establish a clear trend, so set $k_3 = 1.03 \times 10^5$ Pa, the mean value. Given the lack of coronary venous stiffness measurements, we assume that veins have the same material properties as vessels within the structured tree. There is a trend of decreasing vessel stiffness with diameter, so this value is likely to be an over estimation of the true value. Later, we will explore the impact of the stiffness of vessels within the vascular bed.

Length-to-Radius Ratio and Minimum Radius The length l of vessel segments within the structured tree are governed by their proximal radius r_0 and the length-to-radius ratio (l_{rr}). This is calculated for the coronary tree using the length and diameter of porcine coronary arterial and venous segments [4, 5]. The data are presented in Fig. 5.15 as a log-log plot. There is a gradient separation between the smallest four vessel orders and larger vessels, so two lines of the form

$$\log(l) = a\log(r_0) + b,$$

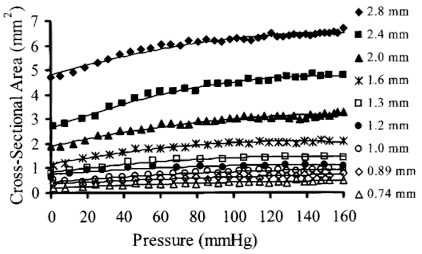

(a) Compliance curves for several generations of porcine coronary arteries from [8]. Legend values are vessel diameter at 80 mm Hg.

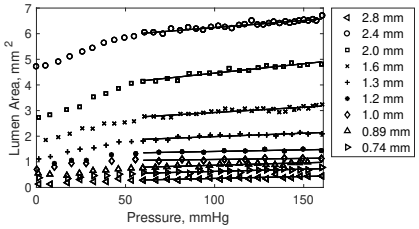

(b) Reproduction of the data shown in Figure 5.14a. Straight lines best fit of the form $A = Cp + b$ are added to determine compliance. Values for C are given in Table 5.4.

Figure 5.14: Pressure-area curves measured in *in situ* porcine coronary arteries.

are least squares fitted to the data with parameters $a, b \in \mathbb{R}$ chosen to maximise R^2. The l_{rr} is given by e^b and is set as $\exp(3.58) \approx 36$ for both arteries and veins.

Set $r_{min} = 10\,\mu\text{m}$ to be the smallest radius of a vessel in the structured tree. This value is chosen as this is the radius of capillaries. The value of r_{min} controls controls the number of vessels within a structured tree; lower values allow for larger trees. We investigate the impact of the choice of r_{min} in Section 5.3.9.

Vessels of O.4 have radii less than 35.4 µm. The l_{rr} change at this level can be understood as arising from the differences in structure and function venules and arterioles (radius < 100 µm) and arteries and veins (radius > 100 µm) [138]. Given this, the minimum radius of structured tree vessels is set at 35 µm.

Boundary Pressures For the inlet fluid pressure profile, we use a signal adapted from data measured *in vivo* by Mynard, Penny & Smolich [6]. The original data and adapted signal are shown in Fig. 5.16. The measured diastolic pressure is 83 mm Hg , and systolic 102 mm Hg , which is considered to be optimal [142]. The original

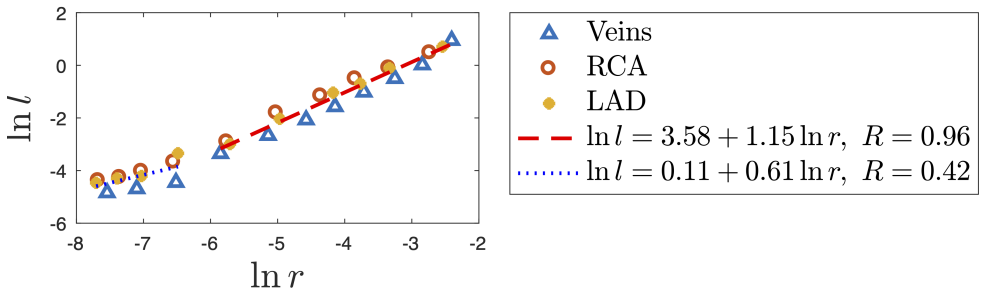

Figure 5.15: Log-log plots of the element length and radius for coronary arteries and veins from Kassab *et al.* [4,5] with lines of best fit for small (blue) and large vessels (red). $R = 1 - \frac{RSS}{TSS}$ is a goodness of fit measure, where RSS is the residual sum of squares and TSS is the total sum of squares.

pressure profile is not periodic. In order to make it so, I find the value final value taken by the profile $p(T)$, and the time at which that value was first achieved τ. The signal $p(t)$, $t \in [\tau, T]$ for period T is periodic. The 0.08 s of the signal (highlighted in red dots in Fig. 5.16) is discarded in order to achieve periodicity. The period is reset $T = 0.7$ s. Systole runs from 0 – 0.3 s, ending at the diacrotic notch – the small dip in fluid pressure. This marks the beginning of diastole which runs until the end of the period at 0.7 s.

The CS drains into the right atrium. Mean right atrial pressure is generally varies about 5 mm Hg [143,144]. Given this, we set the venous outlet pressure at 5 mm Hg.

External Pressure Bovendeerd *et al.* [145] studied the dependence of coronary blood flow and pressure on ventricular loading and contractility using lumped parameter models for the coronary and systemic circulation. They report that the peak intramyocardial pressure coincides with peak left ventricle pressure. Intramyocardial pressure is the pressure applied to the structured trees. Bovendeerd *et al.* give an example of an external pressure profile with a peak of 67 mm Hg. Heineman &

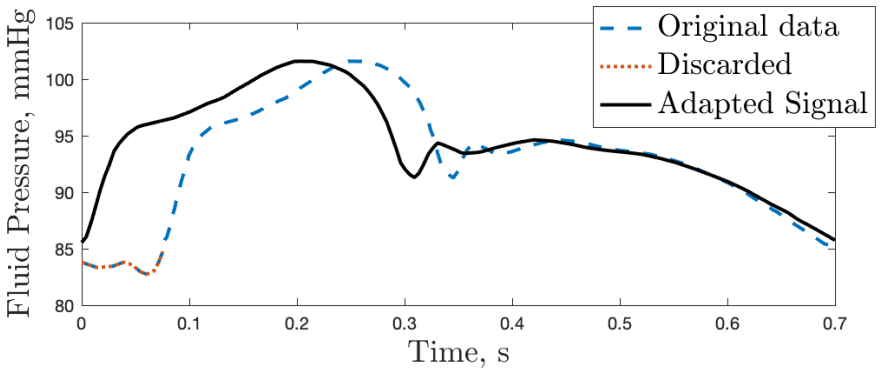

Figure 5.16: The measured fluid pressure profile used as the inlet boundary condition adapted from Mynard, Penny & Smolich [6]

Grayson [146] measured intramyocardial pressure, reporting that is is closely correlated to left ventricle pressure and varies between 2 mm Hg and 107 mm Hg (with associated left ventricle pressure of 146 mm Hg). Here, we choose the intramyocardial pressure to peak at approximately 0.21 s, to coincide with peak fluid pressure. The profile is shown in Fig. 5.17a with a peak of 1 mm Hg. In practice, we set peak pressure during simulations, the values of which are discussed later.

The heart sits within the pericardium, a fluid-filled sac that transfers pressures from the pleural cavity to the epicardial surface under normal conditions [148]. Pericardial pressure increases during cardiac tampanode, a condition in which the pericardium is overfilled with blood or another fluid (pericardial effusion), preventing the heart from beating normally. In the absence of a pericardial effusion, pressure within the sac is typically around -2 mm Hg. Borlaug & Reddy [147] report that mean pericardial pressure varies directly with right atrial pressure. This relationship is shown in Fig. 5.17b.

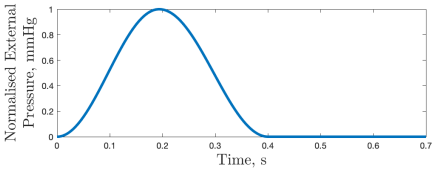

(a) Normalised external pressure profile applied to structured trees.

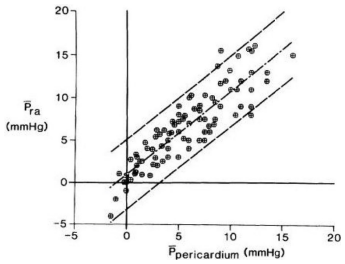

(b) The relationship between mean pericardial and right atrial pressure from Borlaug & Reddy [147].

Figure 5.17: Fluid pressure and external pressure profiles used in coronary simulations, and experimental data showing the relationship between right atrial and pericardial pressure.

5.3 Simulations

In this section, I present simulation results from various coronary trees. I compare simulations from several left coronary trees generated using the method described at the beginning of the chapter. We attempt to quantify the difference to wave intensity made by, for example, modelling arterial trifurcations directly, as opposed to successive bifurcations.

The period $T = 0.7s$ unless noted otherwise. Again, unless noted all simulations use the same parameter values for vessel stiffness k_1, k_2, k_3, minimum structured tree radius r_{min}, characteristic length, and temporal resolution. The time-step is set to be at most $\approx 1.5 \times 10^{-5}$ s.

5.3.1 Computational Time

The networks used in coronary simulations have between ten and fourty-four vessels. In addition to this, the radii of coronary vessels are small compared to the pulmonary system with maximum radii of 1.8 and 13.6 mm, respectively. Due to the small size of coronary vessels, a the characteristic radius $L_r = 2.5\,\text{mm}$ is chosen for these simulations. The characteristic radius governs the spatial step. In order to satisfy the CFL condition, we need a smaller time-step than in the pulmonary simulations. The combination of small time-step and large network size extends computational time for the coronary simulations. A typical pulmonary simulation takes fewer than 10 s, where as a coronary simulations can take hours to complete.

5.3.2 Network Optimisation

The coronary networks produced using the methods discussed above often require some refinement for use in simulations to avoid excessive computational times caused by small spatial steps or many computational cycles needed to reach a periodic solution. These adjustments are limited to increasing segment length and distal radii.

Spatial resolution can be set in each vessel individually. Insufficient resolution within a vessel leads to numerical instability and a failure to converge to a periodic solution. However, high spatial resolutions require high temporal resolutions to satisfy the CFL condition.

We require that each vessel contain at least 4 spatial nodes, i.e., for a vessel of length L step size is $\Delta x < L/4$. If a choice for Δx causes the CFL condition to be violated, then the L and Δx are increased by some constant factor.

Vessels taper longitudinally. However, due to errors in radius measurement, the

data from which we construct trees does not reflect this assumption. For each vessel to be included in a tree generated from data, the proximal and distal radii are $\bar{r}_0 \pm \sigma$, respectively, where $\bar{r}_0$ is the mean radius at the nodes in the vessel, and σ is their standard deviation.

We have observed that if a network contains large vessel in which the taper, i.e. ratio of proximal to distal radii $r_0(0)/r_0(L) > 4/3$ for a vessel of length L, simulations produce high frequency oscillations that do not necessarily reach a periodic steady state within 100 computational cycles. An example of this behaviour can be seen in the blue curves of Fig. 5.18. To rectify this, a lower limit

$$r_0(L) = \frac{3}{4} r_0(0)$$

of the distal radius is set. If the distal radius of a terminal artery is adjusted, then the distal radius of any veins is also altered. The proximal radii of veins is altered only if $r_0(0) < r_0(L)$ is violated. The simulated flow and pressure in an artery and adjoining vein with adjusted radii are shown in orange in Fig. 5.18. The summary table of the trees used for these figures is given in Table C.1. The original vessel had radii $r_0(0) = 1.5\,\text{mm}$, $r(L) = 0.9\,\text{mm}$ and length $L = 7.7\,\text{mm}$; the adjusted radius is $r(L) = 1.15\,\text{mm}$. Further research is needed to determine the acceptable limit of the ratio $r_0(0)/r_0(L)$, and whether this ratio varies between networks. Such instances of high-frequency oscillation may arise due to our choice of PDE solver (Richtmyer's two-step Lax–Wendroff method), and could potentially be avoided by using, for example a flux-splitting scheme. This is outwith the scope of this thesis, but is a potentially fruitful area of research.

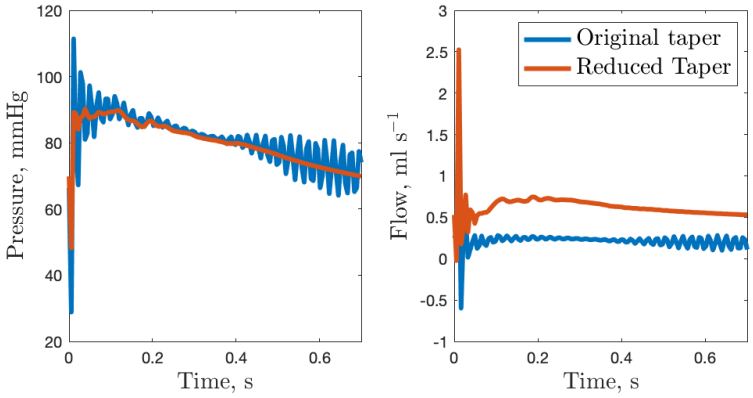

(a) Simulated flow and pressure at the outlet of Artery[3].

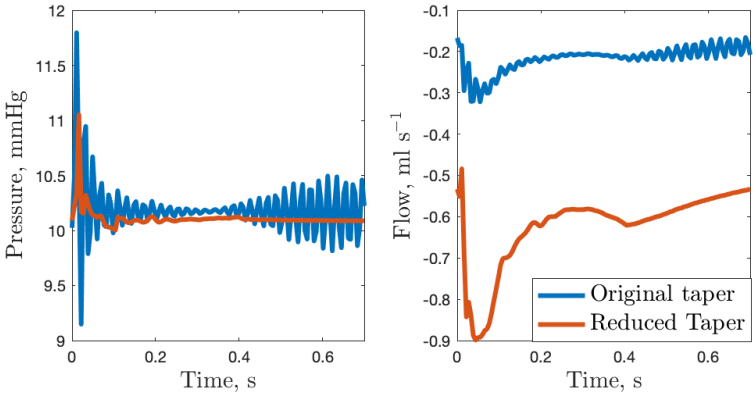

(b) Simulated flow and pressure at the outlet of the adjoining vein.

Figure 5.18: Pressure and flow simulations at the mid-point of an artery (a) and adjoining vein (b) with (orange) and without (blue) adjusted radii. Flow is higher in the case with reduced taper, as this depends on vessel area which was increased. Both simulations are run for 10 cycles. Venous flow is negative due to the convention of veins running from the outlet in the RA to the vascular beds.

5.3.3 Convergence to a Periodic Solution

For pulmonary simulations, we defined a periodic solution as one in which no quantity (pressure, flow, wavespeed, etc.) varies by more then 1% from the previous period and where the venous outlet volume is within 3% of the arterial inlet volume. To assess periodicity, all quantities of interest are compared at each spatial point in the computational domain against the value from the previous period. Flow conservation within coronary vessels is relatively poor, with some Vessel 4 from the 850 µmtrifurcating tree in Table C.1 showing volume losses of 23% from 0.30 ml at the inlet to 0.37 ml at the outlet. In general, volume conservation is worse in shorter vessels that contain fewer spatial points than longer vessels. The absolute volume change is small, but the low flow in narrow coronary vessels means that they are relatively large. We saw absolute changes in fluid volume within vessels in the pulmonary circulatory model. Volume change within vessels is indicative of insufficient spatial resolution, doubling the spatial step-size increases the volume gain to 51% in a Vessel 5. This also holds true in the pulmonary circulation, where we showed that increasing the spatial resolution decreases volume loss, see Fig. 4.5. Volume is conserved at all junctions, so any change that occurs has arisen with the vessel. Given this, we accept satisfactory volume conservation as a volume loss or gain between the arterial inlet and venous outlet of less than 10% relative to the inlet volume.

No coronary simulations converged when using the radius dependent viscosity. Therefore, for the following simulations, we use a constant viscosity of $\mu = 4.503\,\text{mPa s}$ in all vessels. Introducing the radius dependent viscosity has the effect of increasing vascular bed resistance. As we will see shortly, downstream resistance strongly impacts peak flow and pressure. Further work needs to be done to establish structured tree parameters that allow successfully use a radius dependent viscosity

description.

5.3.4 Impact of Junction Type on Wave Intensity

When generating large arterial trees, the user must make several decisions about the network morphometry. To quantify the impact of network morphometry on simulations, I generate three trees using the same truncation (mean radius $> 850\,\mu\text{m}$). The first tree includes a trifurcation and segments in series with each other are consolidated into longer vessels; the second replaces the trifurcation with two sucessive bifurcations; and the third has a trifurcation but does not join series segments into vessel elements which we call a segmented tree. The arterial sides of the trees is shown in Fig. 5.19a, Fig. 5.19b and Fig. 5.19c and their summary tables can be found in Tables C.1, C.2 and C.3. The venous side is comprised of a single generation of veins that all have a static outlet pressure or 5 mm Hg. The simulations are all driven with the same fluid pressure and use the same set of parameter values described above. These simulations have no external pressure applied to either small or large vessels.

The difference between simulations in these trees is quantified using the net wave intensity at the distal end of the initial artery of the trees. Net wave intensity $I = \mathrm{d}p \cdot \mathrm{d}u$ is the flux of energy per unit area that is carried by the wavefronts that are propagating backwards and forwards [149], where dp fluid pressure change (mm Hg) and $\mathrm{d}u$ fluid velocity change ($\mathrm{m\,s^{-1}}$). This definition of wave intensity is sensitive to the sampling rate, so we adopt the definition

$$I' = \frac{\partial p}{\partial t}\frac{\partial u}{\partial t},$$

given by, for example, Broyd *et al.* [13].

The inlet artery in all three trees is the same, so any differences in pressure, flow, and wave intensity must arise from the tree morphometry. Figure 5.19d shows

the fluid pressure, flow, and wave intensity at the distal end of the left coronary artery. The pressure in all of the trees is very similar, but there are some differences in the flow and wave intensity. The flow in the trifurcating tree is higher than in the other two trees, but the network volume in the reference configuration is also higher (1.19 ml, versus 1.11 ml for the bifurcating tree and 1.02 ml for the segmented network). The network comprised of unjoined segments is the smallest in volume and also has the lowest flow. We saw the same behaviour in the mono-, bi-, and trifurcting trees in Chapter 4; the trifurcating tree had the largest volume, and the largest flow. Wave intensity is lower in the trees with smaller volume as the fluid velocity is lower. There are no discernable changes in pressure or flow waveforms that arise in the different networks. From this, we can conclude that network volume is an important determinant of predicted flow and wave intensity.

Broyd *et al.* [13] report peak net coronary arterial wave intensity of approximately $1.8\times10^5\,\mathrm{kg\,s^{-4}}$ which occurs in early systole. The peak wave intensities in the simulations presented here are between 1.5 and $1.8\times10^5\,\mathrm{kg\,s^{-4}}$, also occurring in early systole. Further, there is a second peak in wave intensity that coincides with end systole. Such peaks have also been reported by Mynard *et al.* [150], Broyd *et al.* [13], and Sen *et al.* [14].

All three simulations are volume conserving and have achieved periodicity.

5.3.5 Radius Truncation Condition and Predicted Flow

Using the method described at the beginning of this chapter, we are able to generate trees using different truncation radii. The value of the truncation radius affects the fluid pressure, flow and wave intensity. The truncation condition therefore is an important consideration building patient specific coronary flow models. Similarly to

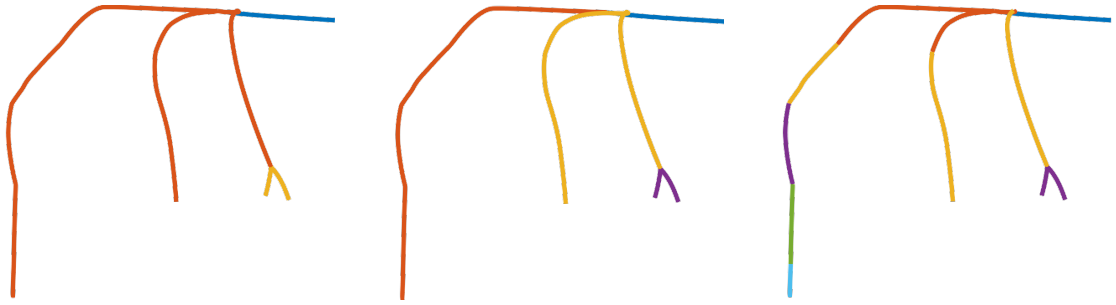

(a) Trifurcating tree. (b) Bifurcating tree. (c) Segmented tree.

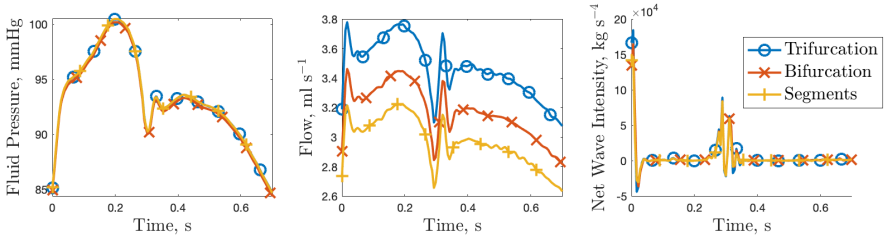

(d) Pressure, flow and wave intensity at the distal end of the inlet artery in the trifurcating (blue), bifurcating (orange) and monofurcating (yellow) trees using $r_{min} = 0.35\,\text{mm}$.

Figure 5.19: Comparisons in flow and pressure between trees using different junction types. The networks arterial side of the networks are shown in (a) – (c) in which a change in edge colour indicates the generation of the vessels.

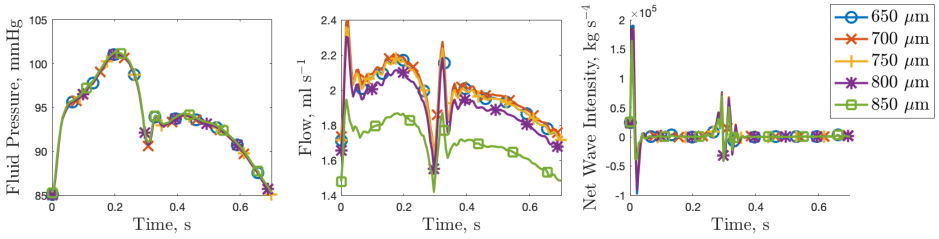

Figure 5.20: Pressure, flow and wave intensity at the distal end of the inlet artery in trifurcating trees with different mean truncation radii without external pressure.

the above comparison between junction types, we plot the pressure, flow, and wave intensity at the distal end of the inlet artery in five trees that were built using different mean truncation radii. The fluid pressure curves are all within 2% of each other, the flows, however, drop with increasing truncation radius. Trees that are truncated at higher radii contain fewer vessels than trees truncated at lower radii, so contain fewer vessels and have lower volumes. The volume of the networks with truncation radii 650 µm and 700 µm have a volume difference of 0.9 nl in the reference configuration and the maximal flow difference between the two networks is 2nl s^{-1}. The 850 µm tree has the smallest volume at 1.19 ml and the lowest flow. This further suggests that the reference configuration network volume is an important determinant of simulated flow.

5.3.6 Large Vessel External Pressure

According to Ramchandaran *et al.* [148], pericardial pressure is approximately equal to pleural cavity pressure. As we saw in the previous Chapter, pleural cavity pressure is typically low, with a mean of around -2 mm Hg. Coronary blood pressure and vessel stiffness are very high relative to the physiologically realistic external pressure expected within the pericardium.

To quantify the impact of pericardial pressure on coronary blood flow, we simulate blood flow and pressure when a sinusoidal pressure (Fig. 4.8) of amplitude 2 mm Hg is applied to the large vessels in the network with truncation radius 650 µm. We then compare the simulated flow and pressure against a simulation using the same parameter set and network. Figure 5.21a shows the percentage difference between the flow and pressure at several points along in the LCA. The simulations we compare have both reached a periodic state and are volume conserving, but there is a low-amplitude high-frequency oscillation that can be seen in the difference that arises because of slight differences in the periodic solutions. The flow difference caused by the imposition of the external pressure never exceeds 1.1% ($0.0074\,\mathrm{ml\,s^{-1}}$) of the undisturbed flow. Venous pressure is the most impacted with changes of up to 7% of the undisturbed pressure which is a uniform 5 mm Hg for an absolute change of 0.35 mm Hg.

For completeness, we run several more simulations with pericardial pressures outwith the physiological range. Figure 5.21b shows the percentage difference from the undisturbed simulation at the distal end of the inlet artery that each of the pressure amplitudes induces in the pressure and flow. From the figure we can see that applying larger pressures causes larger changes in flow and pressure. The pressure profile applied in these simulations is sinusoidal (shown in Fig. 4.8), and the change from the simulated flow and pressure without external pressure is approximately cosinusoidal; this aligns with our earlier observation from Section 4.3 that the change induced by external pressure resembles the time-derivative of the external pressure profile.

Pericardial pressure change is driven by respiration, so the period of physiologically realistic pericardial pressure profiles will be the same as a breath. As is discussed in Chapter 4, breaths are typically a few heart beats long. Increasing the

period of coronary simulations to include pericardial pressure will lead to a increase in computational time. The magnitude of changes induced by pericardial pressures is very low, so we choose to neglect it from now on. Pericardial pressure elevated above 10 mm Hg effect coronary flow by preventing the heart from beating normally, so cannot be captured using this model, as it lacks a ventricle. Elevated pericardial pressure can arise due to excess fluid in the pericardium, known as cardiac tamponade [148].

The largest difference between the simulations presented in Fig. 5.21a occurs 2.5 mm from the inlet of the artery. This difference seen in the plot is caused by a difference in solution to which each simulation converged. This accounts for the slight oscillations seen in the differences for each time step. It is likely that such slight differences also occur in the spatial dimension. This discrepancy is likely to be resolvable by imposing a stricter convergence condition on simulations, at the cost of increasing computational time.

5.3.7 Small Vessel Compression

Coronary arterial flow paradoxically drops during systole [14], to coincide with peak pressure, due to the compression of the majority of the vasculature. Flow then increases during diastole as the microvasculature decompresses. This flow drop can be seen in numerous measurement [14, 151, 152] and simulation studies [6, 48, 153]. Vascular beds are buried within the myocardium so are subject to intramyocardial pressure, as is discussed above. Diastolic intramyocardial pressure is approximately 2 mm Hg, but peak systolic pressure has a range of at least 33 mm Hg (for peak left ventricle pressure 80 mm Hg) to 107 mm Hg (left ventricle pressure is 146 mm Hg) [146]. Figure 5.22a shows the simulated fluid pressure, flow, and wave intensity

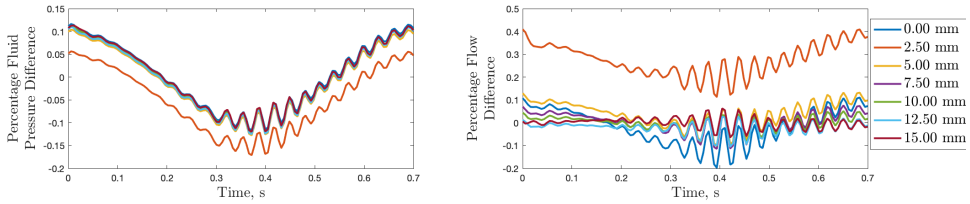

(a) Percentage difference between pressure and flow at several points along a terminal vessel from simulations without external pressure and with a physiologically realistic pressure amplitude. The legend lists distances from the proximal end of the vessel.

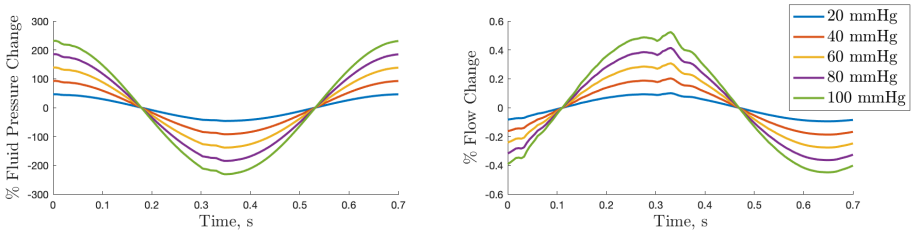

(b) Percentage pressure and flow difference between simulations with external pressure applied and no external pressure. The legend lists the pressure amplitudes for each simulation.

Figure 5.21: Quantification of the impact that large vessel external pressures have on flow and fluid pressure. The low amplitude oscillations arise from slight differences in the periodic solution of the simulations with and without external pressure.

at the distal end of the LCA in the tree with truncation radius 650 µmfor several external pressure amplitudes within the physiological range [30, 110] mm Hg. We compare these against a simulation without an imposed external pressure.

In order to quantify the impact on flow of imposing a compressive external pressure to the structured tree, we run a simulation with no external pressure, and one with the external pressure profile shown in Fig. 5.17a with amplitude 60 mm Hg. The external pressure during diastole is set at 0 mm Hg. Pressure and flow at the inlet of the left coronary artery are shown in Fig. 5.22a.

From the figure, we can see that during systole when the vascular beds are compressed, arterial flow is lower than in the undisturbed case, and diastolic flow is higher. Systolic flow drops by upto $0.4\,\mathrm{ml\,s^{-1}}$ (20%) compared to the undisturbed case. Diastolic flow is similarly higher when an external pressure is applied, versus in the reference case. During systole, when vascular beds are compressed, downstream flow is restricted so upstream flow is reduced; as the compression decreases after peak systole the expanding vascular bed in sucks arterial blood [154], increasing flow in diastole.

Thollon & Vilaine [155] report that systolic flow drops to near 0 during systole. This is a well-known phenomenon, and one that several other modelling studies, e.g. [34, 48, 156] attempt to capture. For any pressure amplitude within the physiological range, we cannot replicate such a flow drop.

Mantero, Pietrabissa & Fumero [156] do so with a 0D lumped parameter model of the cardiovascular system that includes components for the coronary vascular bed and left ventricle with a parameter that controls coronary vascular bed resistance that is analogous to external pressure in this model. They found that increasing vascular bed resistance decreases systolic flow, which agrees well with the model presented here. However, they also found that diastolic flow decreases as vascular

bed resistances increases, contrary to my findings. Vascular bed compression in the model presented here is time dependent, whereas Mantero, Pietrabissa & Fumero's resistance increase was constant throughout the cycle, so would be more akin to a applying a constant external pressure to the vascular bed. In Fig. 5.22b, I have reproduced their graph showing flow change with increasing resistance. The coronary arterial flows predicted by Mantero, Pietrabissa & Fumero are much higher than those found using the model presented here, and other than the pattern of change with increasing resistance, the simulated flow profiles bear little resemblance to each other.

Mynard & Nithiarasu [34] and Duanmu *et al.* [48] present coronary flow profiles that include the effects of vascular bed compression. Duanmu *et al.* also present an example of measured coronary arterial flow. These models use different periods T, and different systolic and diastolic times, as well as external pressure magnitudes. Given these differences, it is difficult to compare our model results quantitatively against theirs. To qualitatively compare our coronary flow against these, the flows are normalised to the lie in the interval [0, 1], and we shift and scale the period so that the flow peaks in systole and diastole coincide for the purposes of comparison. The result of this can be seen in Fig. 5.22c. From the figure, we see reasonable qualitative agreement with the other simulations and with measured data: there is a sharp decline in coronary flow during systole, a flow increase during systole, and a sharp increase during diastole. The systolic flow increase predicted by the model presented here is both higher and later than in the other models – this is possibly due to our choice of external pressure (amplitude 60 mm Hg) relative to peak systolic pressure (102 mm Hg), as we have seen that increasing intramyocardial pressure causes the systolic peak to occur later and for its peak to be higher. The simulation and measurement from Duanmu *et al.* show very good agreement with each other. This

is because the simulation is patient specific and the model parameters were tuned to data from which the measurement was taken. Another possible source of error is the external pressure profile we chose: Mynard & Nithiarasu use a scaled left-ventricle pressure which has plateau like interval during peak systole; this extended period of compression may suppress the rise in systolic flow in their model.

Peak net wave intensity varies between $2.22\times10^5\,\mathrm{kg\,s^{-4}}$ without the external pressure, and $1.99\times10^5\,\mathrm{kg\,s^{-4}}$ with external pressure. These values are inline with those reported in the literature [13, 14].

5.3.8 Increasing Small Vessel Stiffness

We have seen that applying a time-varying external pressure to the vessels in a vascular bed can qualitatively capture the early and late systolic flow minima, and sharp systolic rise seen in measured data and reported in the mathematical literature [34,48,157]. The systolic flow drop depends on many factors, including microvascular stiffness. From Fig. 5.23, it can be seen that as microvascular stiffness increases the fall to the systolic flow minima decrease, and that the diastolic flow peak is smaller. The effect of external pressure applied to the vascular bed is more apparent in more compliant vessels, as compared to stiffer ones, which is to be expected. The same time-varying external pressure (shown in Fig. 5.17a) with amplitude 60mm Hg is applied in all cases.

5.3.9 Microvascular Rarefaction

Vascular rarefaction is the decrease in density of vessels per unit volume within a vascular bed. Microvascular rarefaction has been linked to hypertension [158]. This

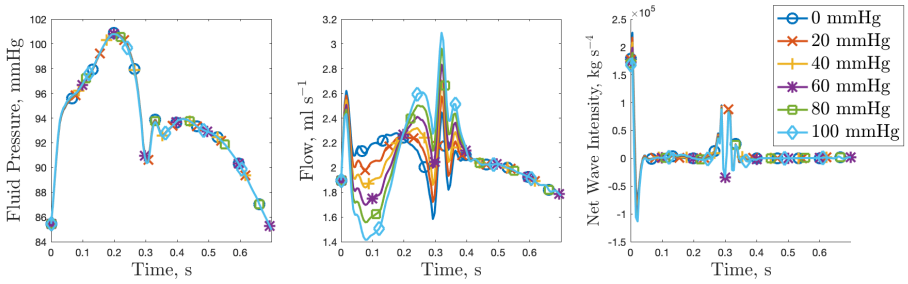

(a) Pressure, flow, and wave intensity at the inlet of the LCA in the 650 µm trifurcating tree with increasing vascular bed compression. The legend gives the peak pressure applied with the time-varying profile given in 5.17a.

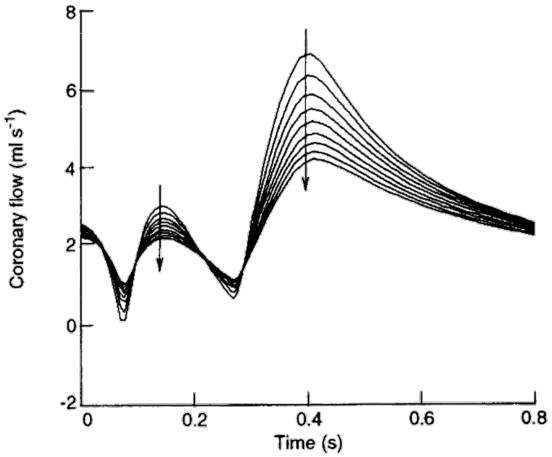

(b) Reproduction of the plot showing flow decrease with increasing vascular bed pressure from Mantero, Pietrabissa & Fumero [156] in a 0D model of the cardiovascular system. The arrows show the direction of change as vascular bed resistance increases.

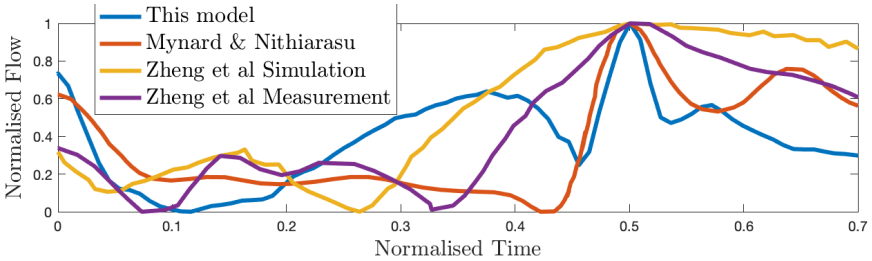

(c) Comparision of normalised LCx flow from this model (blue), Mynard & Nithiarasu, a simulation and measured data from Duanmu *et al.* [48]. We have shifted and scaled the data so peak systolic flow occurs at $t = 0$ and peak diastolic flow at $t = 0.5$.

Figure 5.22: Comparisons of coronary arterial flow showing the drop in systole, late systolic minima, and sharp diastolic rise.

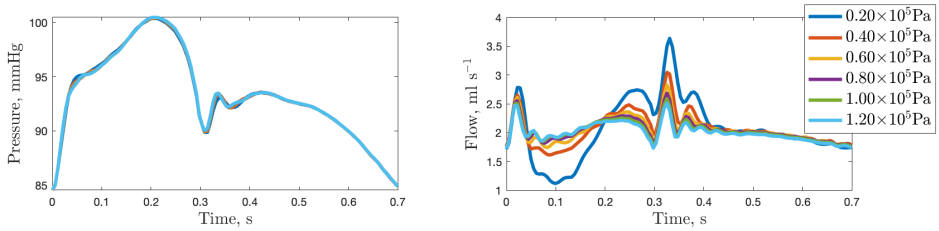

(a) Distal LCA pressure and flow in the 650 µm trifurcating tree for several values of constant microvascular vessel stiffness.

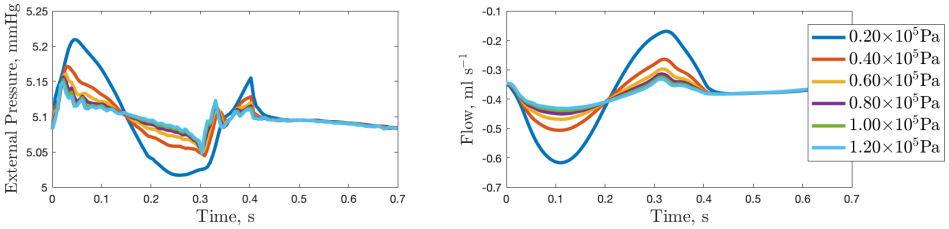

(b) Distal venous pressure and flow (Vessel 10) 650 µm trifurcating tree for several values of constant microvascular vessel stiffness with time-varying external pressure of amplitude 60 mm Hg. Venous flow is negative by convention.

Figure 5.23: Flow and pressure curves at a fixed point in an artery and vein for one period with time-varying external pressure of amplitude 60 mm Hg with increasing vascular bed and venous stiffness. The impact of external pressure is more evident in more compliant vessels.

model uses the parameters ξ, γ, η, r_{min} to control microvascular density

$$r_p^{\xi} = r_{d_1}^{\xi} + r_{d_2}^{\xi}, \qquad \xi \in [2.33, 3], \tag{5.2}$$

$$\gamma = \frac{r_{d_2}^2}{r_{d_1}^2}, \tag{5.3}$$

$$\eta = \frac{r_{d_1}^2 + r_{d_2}^2}{r_p^2} = \frac{1+\gamma}{\left(1+\gamma^{\xi/2}\right)^{2/\xi}}, \qquad \eta > 1. \tag{5.4}$$

As with the pulmonary model, we have set $\xi = 2.76$, $\gamma = 0.41$, and $r_{min} = 10$ µm. Only two of the three η, γ, ξ are independent (see Section 4.1 Scaling Factors). By altering these, we are able to simulate coronary microvascular rarefaction with a time-varying external pressure with amplitude 60mm Hg applied to the vascular beds. Increasing the minimum radius of vessels in the structured tree decreases overall vascular resistance, to arterial flow increases and pressure drops, as can be seen in Fig. 5.24a. However, setting r_{min} constant and increasing ξ, the radius exponent increases the number of vessels and terminal branches, so has the effect of decreasing vascular resistance. Decreased vascular resistance leads to higher arterial and venous peak flow, and flow over all and lower peak blood pressures. These effects are the same as those found by Vaughan in the systemic circulation [29].

The main features of arterial flow and pressure waves are not altered by changing the structured tree parameters. Arterial pressure maintains the systolic peak followed by the dicrotic notch that marks the beginning of systole. Flows show a early and late systolic minima before a sharp increase in early diastole. Increasing r_{min} decreases the number of vessels in the strucutred tree, so decreases the number of vessels that are subject to the intramyocardial pressure. With increasing r_{min} we see that the systolic flow drop decreases, as does the gradient of the diastolic flow increase.

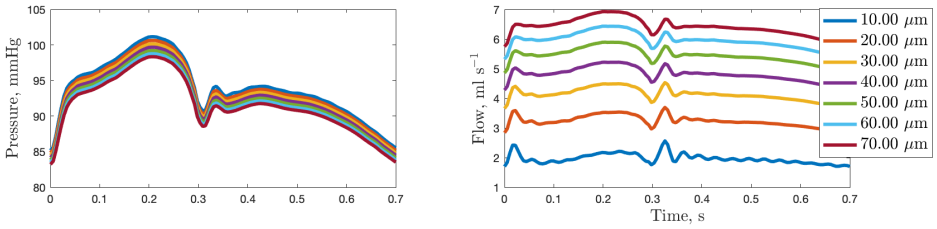

(a) Distal LCA pressure and flow in the 650 µm trifurcating tree for several values r_{min}.

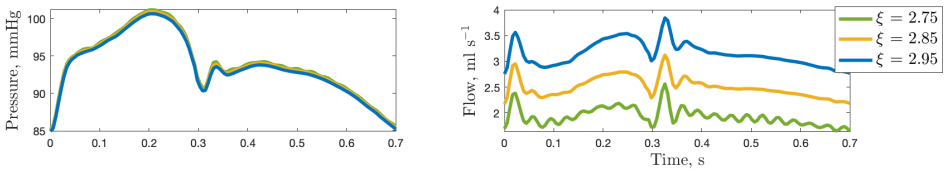

(b) Distal venous pressure and flow (Vessel 10) 650 µm trifurcating tree for several values of constant microvascular vessel stiffness with time-varying external pressure of amplitude 60 mm Hg.

Figure 5.24: Flow and pressure curves at a fixed point in an artery and vein for one period with time-varying external pressure of amplitude 60 mm Hg with increasing vascular bed and venous stiffness. The impact of external pressure is more evident in more compliant vessels.

5.3.10 Branching Venous Network Simulations

All of the simulations shown up to this point have been composed of a left coronary tree and a single generation of veins that are not joined to each other. However, we are able to include separate left and right-coronary arterial trees and a branching venous side with a coronary sinus trunk that drains into the left atrium. The arterial trees were generated with a mean truncation radius of 800 µm. The venous tree was constructed using the method described above. The full summary table is given in Table C.8. Adjustments were made to the tree as described in Section 5.3.2. This tree would have a schematic similar to the one shown in Fig. 5.12, with a two bifurcations in the left tree, and an extra segment. Its summary table is given in Table C.8. Using this tree, can investigate the impact of including a full venous tree on left coronary arterial flow by simulating flow in a network with a single generation of veins, and the full network.

To the best of our knowledge, there is no other coronary flow model that includes a detailed, branching venous network. Studies such as those of Duanmu [49], Huo & Kassab [159], Mynard & Nithiarasu [34], and Mynard, Penny & Smolich [6] use 1D arterial flow models in explicitly defined networks, but use lumped downstream boundary conditions to represent the vascular beds and venous side.

For these simulations, a large arterial stiffness $k_3 = 2.53 \times 10^5\,\mathrm{Pa}$, small vessel and venous stiffness $k_3 = 1.03 \times 10^5\,\mathrm{Pa}$, and characteristic radius $L_r = 1.25\,\mathrm{mm}$ are used. An external pressure of amplitude 60 mm Hg is applied to all structured trees.

The same pressure based boundary condition is prescribed at the inlet of the left and right arterial trees, but flow at the left arterial inlet is higher (71 ml min^{-1}, versus 66 ml min^{-1}). The right and left arterial trees are identical by construction, as are the data for each tree. As such, any flow and pressure differences in the arterial side

must arise from interactions with the venous tree. The left and right-coronary arterial flows are also different from the flow in the inlet artery of the 800 µm trifurcating tree with 5 veins (see Table C.4). The venous outlet boundary condition for each of these veins is the right atrial pressure of 5 mm Hg and there are no vein-vein connections. In general, the RCA gives rise to branches that supply the right atrium, ventricle, and interventricular septum with blood, whereas the LCA and its branches supply the left ventricle. The left ventricle has a higher metabolic demand than the right, due to the thicker wall and greater forces it generates. The left ventricle, therefore requires a greater blood volume to meet its energy needs [160].

The ratio of heart mass to total mass of young pigs of mass 20 – 30 kg is 5 g/kg [123], giving a heart mass of 100 – 150 g. This ratio is identical to that of adult humans. Goodwill *et al.* [161] give approximate flow ranges based on heart mass as $\approx 0.5 - 1.0\,\mathrm{ml\,min^{-1}\,g^{-1}}$ for the left coronary arteries and $\approx 0.3 - 0.6\,\mathrm{ml\,min^{-1}\,g^{-1}}$ for the right. Therefore, we might expect porcine left coronary flows of between 50 – 150 ml $\mathrm{min^{-1}}$ and right-coronary flows of 30 – 90 ml $\mathrm{min^{-1}}$. Our simulated coronary flow does indeed lie within these ranges.

In comparison, total human coronary arterial flow is around $250\,\mathrm{ml\,min^{-1}}$ at rest [15], which is significantly more than in the young porcine heart, since adult humans are significantly bigger. Human hearts range in mass from 188 – 575 g with mean 331 g [162].

It is worth noting that the application of external pressure does not impact the net inflow volume.

5.3.11 Increased Large Artery Stiffness

Coronary artery disease is caused by the formation of atherosclerotic plaques and is characterised by the chronic inflammation of artery walls [163]. Coronary artery disease can lead to local vessel stiffening, lumen narrowing, or both [89]. We can use this model to investigate the impact of large artery stiffness in the coronary circulation. Figure 5.25 shows blood pressure, flow and net wave intensity at the distal end of the LCx in the trifurcating tree with truncation radius 650 µm (vessels 3 and 11 from Table C.7).

As large arterial stiffness increases, and structured tree and venous stiffness are held constant, we see that flow and pressure are both relatively insensitive to this change, but the flow peak and trough seen in early diastole (around 0.3 s) decrease in amplitude. As vessels become increasingly stiff, their ability to distend and increase their fluid capacity is reduced, and the variation between the peak and trough flows decreases.

There is no external pressure in these simulations. The same changes in pressure and flow are seen when a time-dependent external pressure is applied to the vascular beds.

The flow in the venous side is negative by convention, as veins are oriented from the outlet in the right atrium to the vascular bed. From Fig. 5.25b we can also see the pulse propagation into the venous side. A key advantage of the grand admittance based boundary condition is that it allows us to capture this wave propagation.

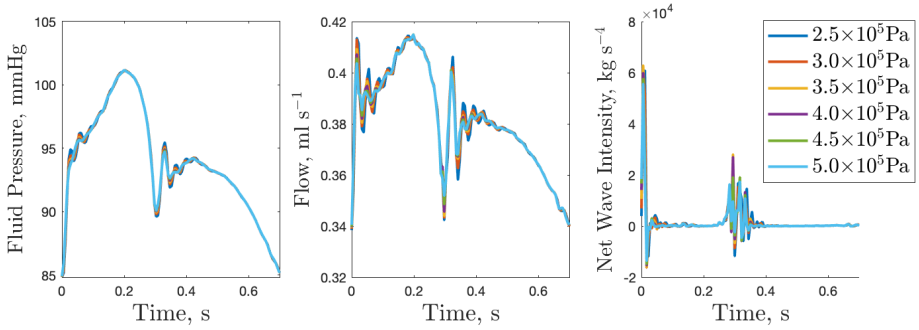

(a) Pressure, flow, and net wave intensity in an artery with increasing large arterial stiffness.

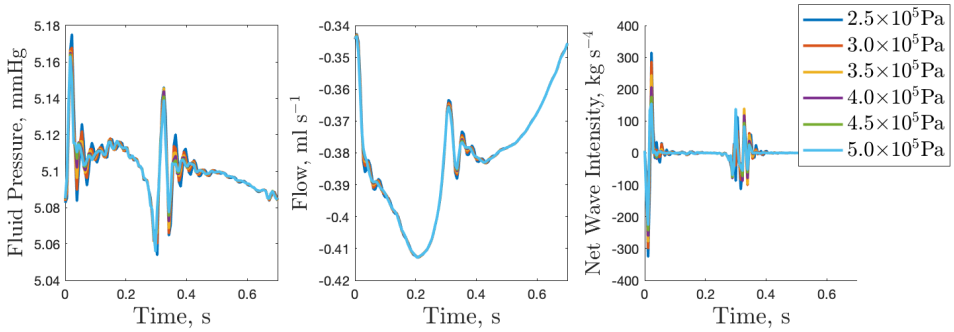

(b) Pressure, flow, and net wave intensity in a vein with increasing large arterial stiffness.

Figure 5.25: Fluid pressure, flow and net wave intensity in a large artery (Vessel 2 in Table C.7) and adjoining vein. Large arterial stiffness is increased between simulations we see that flow and pressure peaks and troughs have smaller amplitude.

5.4 Summary and Future Directions

The simulated coronary flow profiles seen above have relatively large diastolic peaks. These are likely due to the choice of large vessel stiffnesses and structured tree parameters. A larger statistical parameter study, such as those conducted by Paun and others [164–166], is needed to choose values that result in simulated flows and pressures that more closely align with results from the literature. Similarly, the simulated coronary flows in all trees are lower than the physiological range, and more research is needed to develop trees.

The right and left coronary trees were assumed to have the same reference configuration morphometry, which is not physiologically realistic, as the RCA has shorter length and smaller radius than the LCA trunk and does not give rise to large branches as proximally as the LCA. It would be advantageous to implement this model using a right and left coronary arterial trees, and a venous tree with data from a single heart.

In this model we only include venous drainage via the coronary sinus, however, as much as 10% of the coronary blood volume drains into all chambers of the heart via the Thebesian vessels. These are entirely neglected in this model. It may be possible to include these by developing a one-sided structured tree and pressure profile at the outlet of each of the terminal vessels in the structured tree. Similarly, there are many possible variations of venous anatomy, including the absences of the oblique vein of the left atrium, and the small cardiac vein draining directly into the right atrium. No such venous variations have been modelled here.

There are pathologies, such as high take-off [167] that the model is not equipped to deal with. High take-off is a coronary artery anomaly in which either the LCA or RCA arises more than 1 cm above the typical position at the sinotubular junction.

Modelling such a condition would require that we simulate flow and pressure in the aortic root. Our model assumptions are not applicable in the aorta owing to its large size and complexity of flow, but, for example, Chen *et al.* [168] have successfully simulated 3D flow in the left ventricle coupled to a 1D model for the systemic circulation.

As the fluid model is 1D, we are unable to accurately model anomalies of tortuosity as in a "shepherd's crook" RCA [134] in which the vessel follows a switchback course across the epicardium.

Intramyocardial pressure varies throughout the heart wall, both with depth (endocardial pressures are higher than epicardial pressures), and with the region of the heart wall that is being perfused. As part of an ongoing cardiovascular modelling project, we are working to integrate this coronary flow model with a poroelastic wall model of the beating heart. The 1D coronary flow model is coupled to the poroelastic wall model, and supplies net inflow into regions of the myocardium that are perfused and drained by different large vessels. Such a model may be capable of modelling coronary flow during cardiac tampanode, as it could include the restriction of the left ventricle by the fluid filled pericardium.

Chapter 6

Summary, Conclusions, and Future Directions

We began by deriving a system of 1D equations for pulsatile flow in finitely long, elastic walled vessels, filled with homogenous, viscous blood, that explicitly include a time-varying external pressure applied uniformly along the length of the vessel. We extended the analysis to flow in the vessels of the structured-tree, finding an admittance matrix boundary condition that relates fluid and external pressure to arterial and venous flow. The theory we developed allows different external pressure to be applied to each vessel. In principle, this includes those in the structured-tree.

In Chapter 3, we develop the numerical schemes used in the model. This began with the two-step Lax–Wendroff scheme used to solve the system of model equations within a section of vessel. After this we moved on to discussing the boundary conditions at the vessel inlet, at junctions, over the structured-tree, and at the outlet. Here, we extended the structured-tree boundary-matching condition developed by Qureshi [3] and Vaughan [29] to include the external pressure profile that is applied

to the structured-tree. As it stands, the numerical scheme described assumes that the pressure applied to the structured-tree is spatially uniform. Further, we generalised the bifurcation matching condition to join one parent vessel to arbitrarily many daughters – an r-furcation. The new junction-matching condition can be used to directly model vessel stenoses or local changes in vessel stiffness. It is also more robust than previous boundary matching scheme, and is less prone to rounding errors. The r-furcations presented here are superficially similar to those presented by Mynard & Nithiarasu [34], but are developed and implemented independently.

Chapter 4 is concerned with model testing and simulation of pulmonary flow during different respiratory states. We saw that the model behaves in an intuitively sensible and self-consistent manner — fluid volume is preserved across all boundaries, including during the application of external pressure. Further, when a vascular bed is compressed, arterial flow drops (due to increased microvascular resistance) and venous flow increases (as fluid is squeezed out of the vascular bed); we see the opposite behaviour when a negative pressure is applied such as during quiet respiration.

In Chapter 5 we developed a framework with which to build full coronary trees from limited data that approximate the morphometry of physiologically realistic trees. Using data from the literature, we set parameter values for use in the coronary simulations, all of which are directly measurable or inferable from measurements. We then simulated flow in several of these trees, showing that large vessel network morphometry is an important determinant of flow. We further showed that physiologically realistic compressive pressures applied to large vessels alone do not have a significant impact on coronary flow; this is due to the high fluid pressure in large arteries relative to external pressure, and the stiff large vessel walls. Pressures applied to the structured-trees do, however, significantly impact the simulated flow profiles; we see a large flow drop during systole as the vascular beds are compressed

by the squeezing of the myocardium, and a peak in early diastole as the compression decreases. The pattern of changes we see aligns well with reports from the literature, and agrees qualitatively with other coronary modelling studies.

In practice, it is straight forward to apply a different external pressure to each large vessel, and to the structured-trees, but varying pressures within a structured-tree proved more complicated. A possible way forward is to introduce a radius-based scaling factor into the calculation of admittance matrices, so that pressures may be allowed to vary throughout the structured-tree. This is motivated by the assumption that smaller vessels are typically buried deeper within a tissue than larger vessels, so will be subject to greater external pressures as the organ moves.

As was noted in the discussion of pulmonary circulation models in Chapter 4, Clipp & Steele [46] found that flow is insensitive to changes in external pressure when using a flow as the inlet boundary condition. In our model, we use a pressure based boundary condition, and see that flow changes during respiration, but pressure largely remains the same. To better compare these models, we could implement a flow inlet condition, and simulate pulmonary flow using the same inlet data as Clipp & Steele.

This model could be coupled to a left ventricle model, such as was done by Chen [40], and a right atrium to include feedback throughout the respiratory cycle [169]. Such a model could be used to simulate pulmonary flows over longer time scales, and adapting the inlet boundary condition so that flow is driven by a beating heart model. Further, the pulmonary circulation model could be coupled with those for ventilation and flow around the alveoli to assesses pulmonary perfusion during respiration, with extensions to the quantification of alveolar injury resulting from mechanical over inflation.

Much validation needs to be carried out before this model is used in a patient-

specific setting, or to inform clinical decision making. Such validation could involve practical microfluidic experiments, as in, for example Sirs [170]. Other model validation should come in the form of quantitative comparisons against measured data in the pulmonary system.

The large coronary trees are built using measured data from a left porcine coronary arterial, and from averaged vessel lengths for several porcine hearts. We believe that this is a reasonable facsimile of the porcine coronary vasculature, but further study is needed to determine the accuracy of our idealised trees. Further, the model can be made patient-specific, and a patient specific coronary modelling study with a model implemented using only parameters with physical significance would likely be of mathematical and medical interest. If such data were available, detailed patient specific model calibration and validation could be carried out.

While simulated coronary flow did lie within the physiological bounds, a a larger statistical study on flow variation with network geometry and structured tree parameters would better inform our parameter choices in later modelling studies [164,165].

No coronary simulations converged to a periodic solution when using the radius dependent viscosity description. More research is needed to establish where the issue lies, and to resolve it.

As mentioned previously, we are currently working to couple the 1D coronary flow model to a poroelastic model of a beating heart. This work is not presented here, but will lead to detailed mathematical studies of, for example, perfusion during myocardial infarction, vessel stenosis, microvascular rarefaction, or cardiac tamponade.

In addition to the above research directions, the model developed here has the potential to be used to answer clinically or biomedically relevant questions. For instance, a properly calibrated model could be used to help predict blood pressure

changes given appropriate flow measurements. This may obviate some of the clinical need for regular invasive blood pressure measurements as are made [171].

Appendix A

Further Mathematical and Numerical Details

A.1 Calculation of B and its Derivatives

In this section we find $B(x,t)$ and its derivatives that are necessary for the computational scheme. To do this, we define

$$\hat{B}(r_0(x),\varphi(x,t)) = \int_{p_0}^{\varphi(x,t)} A(p^*)\ \mathrm{d}p^* \tag{A.1}$$

where

$$A(p^*) = A_0(x)\left(\frac{p^*}{f(r_0(x))}+1\right)^2,\ f(r_0(x)) = \frac{4}{3}\frac{Eh}{r_0(x)}.$$

so

$$\begin{aligned}\hat{B}(r_0(x),\varphi(x,t)) &\equiv \frac{f}{2\sqrt{A_0}}\int_{A_0}^{A(\varphi)}\sqrt{A(p^*)}\ \mathrm{d}A(p^*)\\ &= \frac{f}{3\sqrt{A_0}}\left(\left[A(\varphi)\right]^{3/2}-A_0^{3/2}\right)\\ &= A_0 f\left[\frac{1}{3}\left(\frac{\varphi}{f}\right)^3+\left(\frac{\varphi}{f}\right)^2+\frac{\varphi}{f}\right].\end{aligned} \tag{A.2}$$

as

$$\frac{\mathrm{d}A(p^*)}{\mathrm{d}p^*} = 2\frac{\sqrt{A_0\,A}}{f}. \tag{A.3}$$

To write (2.8, 3.2) in conservation form we require

$$\left.\frac{\partial B}{\partial x}\right|_t = \left.\frac{\partial \tilde{B}}{\partial r_0}\right|_\varphi \frac{\mathrm{d}r_0}{\mathrm{d}x} + \left.\frac{\partial \tilde{B}}{\partial \varphi}\right|_{r_0} \left.\frac{\partial \varphi}{\partial x}\right|_t = \left.\frac{\partial \tilde{B}}{\partial r_0}\right|_\varphi \frac{\mathrm{d}r_0}{\mathrm{d}x} + \left.\frac{\partial \tilde{B}}{\partial \varphi}\right|_{r_0} \left.\frac{\partial p}{\partial x}\right|_t, \tag{A.4}$$

by the multivariate chain rule.

By definition of $\hat{B}$ and the first fundamental theorem of integral calculus

$$\frac{\partial \hat{B}}{\partial \varphi} = A(\varphi).$$

The fluid pressure p and external pressure þ come from data, so we find $\partial p/\partial x$ numerically. As there is no obvious or general functional form for p or þ, I do not evaluate any pressure derivatives. For convenience, I aim to express all the following derivatives as functions of p or φ.

Large vessels taper axially according to

$$r_0(x) = r_0(0)\exp(kx)$$

so $\mathrm{d}r_0/\mathrm{d}x = r_0(0)ke^{kx}$ where $k = \frac{1}{L}\ln\left(\frac{r_0(L)}{r_0(0)}\right)$ determines degree of taper. For a vessel of length L, $r_0(0)$ and $r_0(L)$ are given.

Lastly, we find

$$\begin{aligned}\left.\frac{\partial \tilde{B}}{\partial r_0}\right|_\varphi &= \frac{\partial}{\partial r_0}\left(\frac{f}{3\sqrt{A_0}}\left([A(\varphi(x,t)]^{3/2} - A_0^{3/2}\right)\right) \\ &= \underbrace{\frac{\mathrm{d}}{\mathrm{d}r_0}\left(\frac{f}{3\sqrt{A_0}}\right)}_{(1)}\left(A(\varphi)^{3/2} - A_0^{3/2}\right) + \frac{f}{3\sqrt{A_0}}\Bigg(\underbrace{\frac{\partial}{\partial r_0}\left(A(\varphi)^{3/2}\right)}_{(2)} - \underbrace{\frac{\partial}{\partial r_0}\left(A_0^{3/2}\right)}_{(3)}\Bigg).\end{aligned}$$

Let us evaluate the three derivatives separately. The first is

$$\frac{\mathrm{d}}{\mathrm{d}r_0}\left(\frac{f}{3\sqrt{A_0}}\right) = \frac{1}{3\sqrt{A_0}}\frac{\mathrm{d}f}{\mathrm{d}r_0} - \frac{\sqrt{\pi}}{3}\frac{f}{A_0},$$

the second

$$\frac{\partial}{\partial r_0}\left(A(\varphi)^{3/2}\right) = 3\left(\sqrt{\pi\frac{A^3}{A_0}} - \frac{1}{f}\left(A^{3/2} - \sqrt{A_0}A\right)\frac{\mathrm{d}f}{\mathrm{d}r_0}\right), \tag{A.5}$$

and the third

$$\frac{\mathrm{d}}{\mathrm{d}r_0}\left(A_0^{3/2}\right) = 3\sqrt{\pi}A_0. \tag{A.6}$$

Taking these together gives, collecting like terms, and writing all areas $A(\varphi)$ as explicit functions of φ gives

$$\begin{aligned}
\left.\frac{\partial\tilde{B}}{\partial r_0}\right|_{\varphi} &= \left(\frac{1}{3\sqrt{A_0}}\frac{\mathrm{d}f}{\mathrm{d}r_0} - \frac{\sqrt{\pi}}{3}\frac{f}{A_0}\right)\left(A(\varphi)^{3/2} - A_0^{3/2}\right) \\
&\quad + \frac{f}{\sqrt{A_0}}\left(\sqrt{\pi\frac{A^3}{A_0}} - \frac{1}{f}\left(A^{3/2} - \sqrt{A_0}A\right)\frac{\mathrm{d}f}{\mathrm{d}r_0} - \sqrt{\pi}A_0\right). \\
&= -\frac{2}{3}\left(\frac{A^{3/2}}{\sqrt{A_0}}\frac{\mathrm{d}f}{\mathrm{d}r_0} + \frac{\sqrt{\pi}}{A_0}A^{3/2}f + \sqrt{\pi A_0}f\right) + \left(A - \frac{A_0}{3}\right)\frac{\mathrm{d}f}{\mathrm{d}r_0} \\
&= -\frac{2}{3}\left(\left(\frac{\varphi}{f}+1\right)^3 A_0\frac{\mathrm{d}f}{\mathrm{d}r_0} + \sqrt{\pi A_0}f\left(\left(\frac{\varphi}{f}+1\right)^3 + 1\right)\right) + A_0\left(\left(\frac{\varphi}{f}+1\right)^2 - \frac{1}{3}\right)\frac{\mathrm{d}f}{\mathrm{d}r_0}.
\end{aligned} \tag{A.7}$$

Vessel wall stiffness is assumed to be $f(r_0(x)) = \frac{4}{3}(k_1\exp(k_2 r_0) + k_3)$ for known constants k_1, k_2, k_3.

The computational scheme also requires $(\mathrm{d}\hat{p}/\mathrm{d}A)$, $(\partial B/\partial A)$, $(\partial^2 B/\partial A\partial x)$. Firstly,

$$\frac{\mathrm{d}\varphi}{\mathrm{d}A} = f\frac{\mathrm{d}}{\mathrm{d}A}\left(\sqrt{\frac{A}{A_0}} - 1\right) + \frac{\mathrm{d}p_e(t)}{\mathrm{d}A} = f\frac{\mathrm{d}}{\mathrm{d}A}\left(\sqrt{\frac{A}{A_0}}\right) = \frac{1}{2}\frac{f}{\sqrt{A\,A_0}}. \tag{A.8}$$

Also,

$$\frac{\partial B}{\partial A} = \frac{f}{3\sqrt{A_0}}\frac{\partial}{\partial A}A^{3/2} = \sqrt{\frac{A}{A_0}}\frac{f}{2} \tag{A.9}$$

from the definition of B. Finally,

$$\frac{\partial^2 B}{\partial A \partial x} = \frac{1}{2}\frac{\partial f}{\partial r_0}\frac{\partial r_0}{\partial x}\sqrt{\frac{A}{A_0}} + \frac{f}{2}\frac{\partial}{\partial x}\left(\sqrt{\frac{A}{A_0}}\right) \tag{A.10}$$

$$= \frac{1}{2}\left(\frac{\partial f}{\partial r_0}\frac{\partial r_0}{\partial x} + \left.\frac{\partial \varphi}{\partial x}\right|_t\right) \tag{A.11}$$

in which

$$\begin{aligned} \frac{\mathrm{d}}{\mathrm{d}x}(f(r_0(x))^{-1}) &= -\frac{1}{f(r_0(x))^2}\frac{\mathrm{d}f}{\mathrm{d}r_0}\frac{\mathrm{d}r_0}{\mathrm{d}x} \\ \frac{\mathrm{d}f}{\mathrm{d}r_0} &= \frac{4}{3}Eh\frac{\mathrm{d}}{\mathrm{d}r_0}(r_0^{-1}) = -\frac{4}{3}\frac{Eh}{r_0^2} \end{aligned} \tag{A.12}$$

and an expression $(\mathrm{d}r_0/\mathrm{d}x)$ is given above.

A.2 Time-Dependent Pressure Inlet Boundary Condition

As discussed in Ch. 3, the time-dependent pressure based inlet condition presented here does not differ from the one derived and presented by Qureshi [3] when we include external pressure.

A fluid pressure profile $p(0,t)$ is prescribed at the inlet over the period of length T s, $t \in [0,T]$. Similarly, we prescribe an external pressure profile $\text{Þ}(t)$. Hence, we can find $\varphi(0,t) = p(0,t) - \text{Þ}(t)$ for the whole period.

Given the constitutive tube law (2.25), $A(x,t) = A_0(x)\left(\frac{\varphi(x,t)}{f(r_0(x))} + 1\right)^2$, $A(0,t)$ is known. The flow $q(0,t)$ is yet to be determined using $\varphi(0,t)$ and $A(0,t)$ with the equation (3.13)

$$\boldsymbol{U}_m^{n+1} = \boldsymbol{U}_m^n + \frac{\Delta t}{2}\left[\boldsymbol{S}_{m+1/2}^{n+1/2} + \boldsymbol{S}_{m-1/2}^{n+1/2}\right] - \frac{\Delta t}{\Delta x}\left[\boldsymbol{W}_{m+1/2}^{n+1/2} - \boldsymbol{W}_{m-1/2}^{n+1/2}\right]$$

so at $m = 0$

$$q_0^{n+1} = q_0^n + \frac{\Delta t}{2}\left[(S_2)_{1/2}^{n+1/2} + (S_2)_{-1/2}^{n+1/2}\right] - \frac{\Delta t}{\Delta x}\left[(W_2)_{1/2}^{n+1/2} - (W_2)_{-1/2}^{n+1/2}\right] \tag{A.13}$$

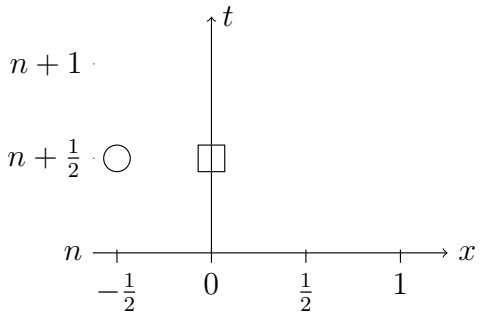

Figure A.1: Inlet: Ghost point marked ∘ is a half step before the inlet of a vessel. Points marked × are known. The point marked □ is found by averaging between adjacent time steps.

in which $(S_2)^{n+1/2}_{\pm 1/2}$, $(W_2)^{n+1/2}_{\pm 1/2}$ are given by (3.5c), and (3.5b) and depend on $A^{n+1/2}_{\pm 1/2}$. Hence, we need to be able to evaluate $A^{n+1/2}_{-1/2}$ which we achieve by using a ghost-point

$$A_0^{n+1/2} = \frac{1}{2}\left(A_{-1/2}^{n+1/2} + A_{1/2}^{n+1/2}\right) \iff A_{-1/2}^{n+1/2} = 2A_0^{n+1/2} - A_{1/2}^{n+1/2} \tag{A.14}$$

as illustrated in Fig. A.1.

Also from (3.13), we have

$$\begin{aligned} A_0^{n+1} &= A_0^n - \frac{\Delta t}{\Delta x}\left[q_{1/2}^{n+1/2} - q_{-1/2}^{n+1/2}\right] \Rightarrow \\ q_{1/2}^{n+1/2} &= \frac{\Delta x}{\Delta t}\left(A_0^n - A_0^{n+1}\right) + q_{-1/2}^{n+1/2}. \end{aligned} \tag{A.15}$$

Between them, (A.13), (A.14), (A.15) have three unknowns $A^{n+1/2}_{1/2}$, $q^{n+1/2}_{1/2}$ and q_0^{n+1}.

Specific choices of inlet boundary condition are discussed in Ch. 4 & 5 as required.

A.3 One-to-many Branching

The unknown when matching a single parent vessel to r daughters are

$$\begin{aligned} &x_{3i+1} = (q_{d_i})^{n+1}_{\mathcal{M}}, \quad && x_{3i+2} = (q_{d_i})^{n+1/2}_{\mathcal{M}}, \quad && x_{3i+3} = (q_{d_i})^{n+1/2}_{\mathcal{M}-1/2}, \\ &x_{3(i+r)+4} = (A_{d_i})^{n+1}_{\mathcal{M}}, && x_{3(i+r)+5} = (A_{d_i})^{n+1/2}_{\mathcal{M}}, && x_{3(i+r)+6} = (A_{d_i})^{n+1/2}_{\mathcal{M}-1/2}, \end{aligned} \tag{A.16}$$

for $i = 0, ..., r$. The parent vessel is denoted d_0.

A.3.1 Residual Equations for Junction Matching

Residual 1 from (3.18a):

$$\begin{aligned} g_1 = &- (q_p)_L^{n+1} + (q_p)_L^n - \frac{\Delta x}{\Delta t}\left(\left((W_2)_p\right)_{L+1/2}^{n+1/2}\right. \\ &\left. - \left((W_2)_p\right)_{L-1/2}^{n+1/2}\right) + \frac{\Delta t}{2}\left(\left((S_2)_p\right)_{L+1/2}^{n+1/2} + \left((S_2)_p\right)_{L-1/2}^{n+1/2}\right). \end{aligned} \tag{A.17}$$

Residuals 2,..., $r+1$ from (3.18a):

$$\begin{aligned} g_{i+1} = &-q_0^{n+1} + q_0^n - \frac{\Delta x}{\Delta t}\left(\left((W_2)_{d_i}\right)_{1/2}^{n+1/2} - \left((W_2)_{d_i}\right)_{-1/2}^{n+1/2}\right) + \\ &\frac{\Delta t}{2}\left(\left((S_2)_{d_i}\right)_{1/2}^{n+1/2} + \left((S_2)_{d_i}\right)_{-1/2}^{n+1/2}\right), \\ &i = 1, 2, ..., r. \end{aligned} \tag{A.18}$$

Residual $r+2$ from (3.18b):

$$g_{r+2} = -A_L^{n+1} + A_L^n - \frac{\Delta x}{\Delta t}\left((q_p)_{L+1/2}^{n+1/2} - (q_p)_{L-1/2}^{n+1/2}\right).$$

Residuals $r+3$, ..., $2(r+1)$ from (3.18b):

$$g_{r+2+i} = -A_0^{n+1} + A_0^n - \frac{\Delta x}{\Delta t}\left((q_{d_i})_{1/2}^{n+1/2} - (q_{d_i})_{-1/2}^{n+1/2}\right).$$

Residual $2r+2$ from 3.19b:

$$g_{2(r+1)+1} = - (q_p)_L^{n+1/2} + \frac{1}{2}\left((q_p)_{L-1/2}^{n+1/2} + (q_p)_{L+1/2}^{n+1/2}\right).$$

Residuals $2(r+1)+2$, ..., $3(r+1)$ from 3.19b:

$$g_{2(r+1)+1+i} = - (q_{d_i})_0^{n+1/2} + \frac{1}{2}\left((q_{d_i})_{-1/2}^{n+1/2} + (q_{d_i})_{1/2}^{n+1/2}\right),\ i = 1, 2, ..., r.$$

Residual $3(r+1)+1$ from 3.19a:

$$g_{3(r+1)+1} = -\left(A_p\right)_L^{n+1/2} + \frac{1}{2}\left(\left(A_p\right)_{L-1/2}^{n+1/2} + \left(A_p\right)_{L+1/2}^{n+1/2}\right).$$

Residuals $3(r+1)+2$, ..., $4(r+1)$ from 3.19a:

$$g_{3(r+1)+1+i} = -\left(A_{d_i}\right)_0^{n+1/2} + \frac{1}{2}\left(\left(A_{d_i}\right)_{-1/2}^{n+1/2} + \left(A_{d_i}\right)_{1/2}^{n+1/2}\right),\ i = 1, 2, ..., r.$$

Residuals $4(r+1)+1$ from (3.17b):

$$g_{4(r+1)+1} = -\left(q_p\right)_L^{n+1} + \sum_{i=1}^{r}\left(q_{d_i}\right)_0^{n+1}$$

a flow conservation condition at time level $n+1$.

Residuals $4(r+1)+2$ from (3.17b):

$$g_{4(r+1)+2} = -\left(q_p\right)_L^{n+1/2} + \sum_{i=1}^{r}\left(q_{d_i}\right)_0^{n+1/2}$$

a flow conservation condition at time level $n+1/2$.

Residuals $4(r+1)+3$, ..., $5(r+1)+1$ from (3.17a):

$$g_{4(r+1)+2+i} = -\left(f_p\right)_L\left(\sqrt{\frac{\left(A_p\right)_L^{n+1/2}}{\left(\left(A_0\right)_p\right)_L}} - 1\right) - \text{Þ}_p^{n+1/2} + \left(f_{d_i}\right)_0\left(\sqrt{\frac{\left(A_{d_i}\right)_0^{n+1/2}}{\left(\left(A_0\right)_{d_i}\right)_0}} - 1\right) + \text{Þ}_{d_i}^{n+1/2}$$

a fluid pressure matching condition at time step $n+1/2$.

Residuals $5(r+1)+2$, ..., $6(r+1)$ from (3.17a):

$$g_{5(r+1)+1+i} = -\left(f_p\right)_L\left(\sqrt{\frac{\left(A_p\right)_L^{n+1}}{\left(\left(A_0\right)_p\right)_L}} - 1\right) - \left(\text{Þ}_p\right)^{n+1} + \left(f_{d_i}\right)_0\left(\sqrt{\frac{\left(A_{d_i}\right)_0^{n+1}}{\left(\left(A_0\right)_{d_i}\right)_0}} - 1\right) + \left(\text{Þ}_{d_i}\right)^{n+1}$$

a fluid pressure matching condition at time step $n+1$.

A.3.2 Example: Jacobian for Matching a Monofurcation

Because we dictate the order in which we list unknowns $\boldsymbol{x}$ and residuals $\boldsymbol{g}(\boldsymbol{x})$, the Jacobian J has a predictable structure. Jacobians can be generated using Alg. 1. Each element of the matrix is the derivative of a residual with respect to one of the unknowns: $J(i,j) = \dfrac{\partial g_i(\boldsymbol{x})}{\partial x_j}$. Explicitly, for $r = 1$ we have

$$J = \begin{bmatrix}
-1 & \cdot & \chi_1 & \cdot & \cdot & \cdot & \cdot & \cdot & \chi_2 & \cdot & \cdot & \cdot \\
\cdot & \cdot & \cdot & -1 & \cdot & \chi_3 & \cdot & \cdot & \cdot & \cdot & \cdot & \chi_4 \\
\cdot & \cdot & -\theta & \cdot & \cdot & \cdot & -1 & \cdot & \cdot & \cdot & \cdot & \cdot \\
\cdot & \cdot & \cdot & \cdot & \cdot & \theta & \cdot & \cdot & \cdot & -1 & \cdot & \cdot \\
\cdot & -1 & \frac{1}{2} & \cdot & \cdot & \cdot & \cdot & \cdot & \cdot & \cdot & \cdot & \cdot \\
\cdot & \cdot & \cdot & \cdot & -1 & \frac{1}{2} & \cdot & \cdot & \cdot & \cdot & \cdot & \cdot \\
\cdot & \cdot & \cdot & \cdot & \cdot & \cdot & \cdot & -1 & \frac{1}{2} & \cdot & \cdot & \cdot \\
\cdot & \cdot & \cdot & \cdot & \cdot & \cdot & \cdot & \cdot & \cdot & \cdot & -1 & \frac{1}{2} \\
\cdot & -1 & \cdot & \cdot & 1 & \cdot & \cdot & \cdot & \cdot & \cdot & \cdot & \cdot \\
-1 & \cdot & \cdot & 1 & \cdot & \cdot & \cdot & \cdot & \cdot & \cdot & \cdot & \cdot \\
\cdot & \cdot & \cdot & \cdot & \cdot & \cdot & \cdot & \chi_5 & \cdot & \cdot & \chi_6 & \cdot \\
\cdot & \cdot & \cdot & \cdot & \cdot & \cdot & \chi_7 & \cdot & \cdot & \chi_8 & \cdot & \cdot
\end{bmatrix}$$

where, for example, $\chi_1 = \dfrac{\partial g_1}{\partial x_3}$ with $x_3 = (q_p)_{L+1/2}^{n+1/2}$ and $\chi_3 = \dfrac{\partial g_2(\boldsymbol{x})}{\partial x_6}$, $x_6 = (q_{d_1})_{-1/2}^{n+1/2}$. These are straightforwardto find using a computer algebra package.

A.3.3 List of Functions χ

The functions χ_i, $i = 1, ..., 4(r+1)$ are derivatives of the elements of $\boldsymbol{g}$ with respect to the elements of $\boldsymbol{x}$, hence, the number of functions increases with increasing r. A consequence of this is that we can only usefully write them down in general. However,

they can be found for $i = 0, ..., r$ as follows:

$$\chi_{1+2i} = \frac{\mathrm{d}g_{i+1}(\boldsymbol{x})}{\mathrm{d}x_{3(i+1)}} \tag{A.19}$$

$$\chi_{2+2i} = \frac{\mathrm{d}g_{i+1}(\boldsymbol{x})}{\mathrm{d}x_{3(2+i+r)}} \tag{A.20}$$

$$\chi_{3+2r} = \frac{\mathrm{d}g(\boldsymbol{x})}{\mathrm{d}x_{3(1+r)+2}} \tag{A.21}$$

$$\chi_{3+2r+i} = \frac{\mathrm{d}g(\boldsymbol{x})}{\mathrm{d}x_{3(1+r+i)}} \qquad i = 1, ..., r \tag{A.22}$$

$$\chi_{4+3r} = \frac{\mathrm{d}g(\boldsymbol{x})}{\mathrm{d}x_{3r+2}} \tag{A.23}$$

$$\chi_{4+3r+i} = \frac{\mathrm{d}g(\boldsymbol{x})}{\mathrm{d}x_{3r+2+3i}} \qquad i = 1, ..., r \tag{A.24}$$

A.4 Structured Tree Boundary Matching Condition

To find the area and flow at the terminii of the artery and vein to be matched, consider the four-point formula (3.13) at the current spatial-step (M^A for arteries, M^V for veins) and the next time-step. Explicitly, this is

$$A_{M^A}^{n+1} = A_{M^A}^{n} - \frac{\Delta x}{\Delta t}\left((W_1)_{M^A+1/2}^{n+1/2} - (W_1)_{M^A-1/2}^{n+1/2}\right) \tag{A.25a}$$

$$q_{M^A}^{n+1} = q_{M^A}^{n} - \frac{\Delta x}{\Delta t}\left((W_2)_{M^A+1/2}^{n+1/2} - (W_2)_{M^A-1/2}^{n+1/2}\right) + \frac{\Delta t}{2}\left((S_2)_{M+1/2}^{n+1/2} + (S_2)_{M-1/2}^{n+1/2}\right) \tag{A.25b}$$

$$A_{M_V}^{n+1} = A_{M_V}^{n} - \frac{\Delta x}{\Delta t}\left((W_1)_{M_V+1/2}^{n+1/2} - (W_1)_{M_V-1/2}^{n+1/2}\right) \tag{A.25c}$$

$$\begin{aligned} q_{M_V}^{n+1} = q_{M_V}^{n} &- \frac{\Delta x}{\Delta t}\left((W_2)_{M_V+1/2}^{n+1/2} - (W_2)_{M_V-1/2}^{n+1/2}\right) \\ &+ \frac{\Delta t}{2}\left((S_2)_{M_V+1/2}^{n+1/2} + (S_2)_{M_V-1/2}^{n+1/2}\right). \end{aligned} \tag{A.25d}$$

Between them, these equations have 10 unknowns:

$$\begin{aligned} &A^{n+1}_{M^A},\ q^{n+1}_{M^A},\ \ (W_1)^{n+1/2}_{M^A+1/2}, (W_2)^{n+1/2}_{M^A+1/2}, (S_2)^{n+1/2}_{M^A+1/2}, \\ &A^{n+1}_{M^V},\ q^{n+1}_{M^V},\ \ (W_1)^{n+1/2}_{M^V+1/2}, (W_V)^{n+1/2}_{M^V+1/2}, (S_2)^{n+1/2}_{M^V+1/2}. \end{aligned} \tag{A.26}$$

In order to determine the S and W terms we need $A^{n+1/2}_{M^A+1/2}$, $q^{n+1/2}_{M^A+1/2}$, $A^{n+1/2}_{M^V+1/2}$, $q^{n+1/2}_{M^V+1/2}$, which we find by considering the ghost-point a half spatial step behind these

$$A^{n+1/2}_{M^A} = \frac{1}{2}\left(A^{n+1/2}_{M^A+1/2} + A^{n+1/2}_{M^A-1/2}\right), \tag{A.27a}$$

$$q^{n+1/2}_{M^A} = \frac{1}{2}\left(q^{n+1/2}_{M^A+1/2} + q^{n+1/2}_{M^A-1/2}\right), \tag{A.27b}$$

$$A^{n+1/2}_{M^V} = \frac{1}{2}\left(A^{n+1/2}_{M^V+1/2} + A^{n+1/2}_{M^V-1/2}\right), \tag{A.27c}$$

$$q^{n+1/2}_{M^V} = \frac{1}{2}\left(q^{n+1/2}_{M^V+1/2} + q^{n+1/2}_{M^V-1/2}\right). \tag{A.27d}$$

Introducing the ghost points has added four unknowns to the system: $A^{n+1/2}_{M^A}$, $q^{n+1/2}_{M^A}$, $A^{n+1/2}_{M^V}$, $q^{n+1/2}_{M^V}$. To find the unknown flows, use the discretised boundary matching conditions (3.22a), (3.22b) at the appropriate point

$$\begin{aligned} \left(q^A\right)^{n+1/2}_{M^A} = \Big(&\left(p^A\right)^{n+1/2}_{M^A}(y_{11})^0 + \left(p^V\right)^{n+1/2}_{M^V}(y_{12})^0 \\ &- \left[\left(\mathfrak{p}^A\right)^{n+1/2}(y^e{}_{11})^0 + \left(\mathfrak{p}^V\right)^{n+1/2}(y^e{}_{12})^0\right] \\ &+ \sum_{k=1}^{N-1}\Big[(p^A)^{\langle n+1/2-k\rangle_N}_{M^A}(y_{11})^k + (p^V)^{\langle n+1/2-k\rangle_N}_{M^V}(y_{12})^k \\ &- \left\{(\mathfrak{p}^A)^{\langle n+1/2-k\rangle_N}(y^e{}_{11})^k + (\mathfrak{p}^V)^{\langle n+1/2-k\rangle_N}(y^e{}_{12})^k\right\}\Big]\Big)\,\Delta t, \end{aligned} \tag{A.28a}$$

$$
\begin{aligned}
\left(q^V\right)_{M^V}^{n+1/2} = \Big(& \left(p^A\right)_{M^A}^{n+1/2} \left(y_{21}\right)^0 + \left(p^V\right)_{M^V}^{n+1/2} \left(y_{22}\right)^0 \\
& - \left(\mathfrak{p}^A\right)^{n+1/2} \left(y^e{}_{21}\right)^0 - \left(\mathfrak{p}^V\right)^{n+1/2} \left(y^e{}_{22}\right)^0 \\
& + \sum_{k=1}^{N-1} \Big[\left(p^A\right)_{M^A}^{\langle n+1/2-k \rangle_N} \left(y_{11}\right)^k + \left(p^V\right)_{M^V}^{\langle n+1/2-k \rangle_N} \left(y_{12}\right)^k \\
& - \left(\mathfrak{p}^A\right)^{\langle n+1/2-k \rangle_N} \left(y^e{}_{11}\right)^k - \left(\mathfrak{p}^V\right)^{\langle n+1/2-k \rangle_N} \left(y^e{}_{12}\right)^k \Big] \Big) \, \Delta t.
\end{aligned}
\tag{A.28b}
$$

The quantities

$$
\left(W_1\right)_{M^A+1/2}^{n+1/2}, \left(W_2\right)_{M^A+1/2}^{n+1/2}, \left(S_2\right)_{M^A+1/2}^{n+1/2}, \quad \left(W_1\right)_{M^V+1/2}^{n+1/2}, \left(W_V\right)_{M^V+1/2}^{n+1/2}, \left(S_2\right)_{M^V+1/2}^{n+1/2}.
$$

are now known and there are now twelve unknowns

$$
\begin{gathered}
A_{M^A}^{n+1}, \;\; q_{M^A}^{n+1}, \;\; A_{M^A+1/2}^{n+1/2}, q_{M^A+1/2}^{n+1/2}, \;\; A_{M^A}^{n+1/2}, q_{M^A}^{n+1/2} \\
A_{M^V}^{n+1}, \;\; q_{M^V}^{n+1}, \;\; A_{M^V+1/2}^{n+1/2}, q_{M^V+1/2}^{n+1/2}, \;\; A_{M^V}^{n+1/2}, q_{M^V}^{n+1/2}
\end{gathered}
\tag{A.29}
$$

and ten equations. Evaluate the discretised boundary condition at time level $n+1$ to add two more equations without adding more unknowns

$$
\begin{aligned}
\left(q^A\right)_{M^A}^{n+1} = \Big(& \left(p^A\right)_{M^A}^{n+1} \left(y_{11}\right)^0 + \left(p^V\right)_{M^V}^{n+1} \left(y_{12}\right)^0 \\
& - \left(\mathfrak{p}^A\right)^{n+1} \left(y^e{}_{11}\right)^0 - \left(\mathfrak{p}^V\right)^{n+1} \left(y^e{}_{12}\right)^0 \\
& + \sum_{k=1}^{N-1} \Big[\left(p^A\right)_{M^A}^{\langle n+1-k \rangle_N} \left(y_{11}\right)^k + \left(p^V\right)_{M^V}^{\langle n+1-k \rangle_N} \left(y_{12}\right)^k \\
& - \left(\mathfrak{p}^A\right)^{\langle n+1-k \rangle_N} \left(y^e{}_{11}\right)^k - \left(\mathfrak{p}^V\right)^{\langle n+1-k \rangle_N} \left(y^e{}_{12}\right)^k \Big] \Big) \, \Delta t,
\end{aligned}
\tag{A.30a}
$$

$$
\begin{aligned}
\left(q^V\right)_{M^V}^{n+1} = \Big(& \left(p^A\right)_{M^A}^{n+1} \left(y_{21}\right)^0 + \left(p^V\right)_{M^V}^{n+1} \left(y_{22}\right)^0 \\
& - \left(\mathfrak{p}^A\right)^{n+1} \left(y^e{}_{21}\right)^0 - \left(\mathfrak{p}^V\right)^{n+1} \left(y^e{}_{22}\right)^0 \\
& + \sum_{k=1}^{N-1} \Big[\left(p^A\right)_{M^A}^{\langle n+1-k \rangle_N} \left(y_{11}\right)^k + \left(p^V\right)_{M^V}^{\langle n+1-k \rangle_N} \left(y_{12}\right)^k \\
& - \left(\mathfrak{p}^A\right)^{\langle n+1-k \rangle_N} \left(y^e{}_{11}\right)^k - \left(\mathfrak{p}^V\right)^{\langle n+1-k \rangle_N} \left(y^e{}_{12}\right)^k \Big] \Big) \, \Delta t.
\end{aligned}
\tag{A.30b}
$$

Following Qureshi [3], we can reduce the number of equations by substituting (A.27a, A.27b, A.27c) into (A.28), and (A.27a, A.27c, A.27d) into (A.28) so (A.28) is written as

$$\begin{aligned}
\frac{q_{M-1/2}^{n+1/2}+q_{M+1/2}^{n+1/2}}{2} &= P_A\left(M,\frac{1}{2}(A_{M-1/2}^{n+1/2}+A_{M+1/2}^{n+1/2})\right)(y_{11}^0)\Delta t \\
&+ P_V\left(0,\frac{1}{2}(A_{-1/2}^{n+1/2}+A_{1/2}^{n+1/2})\right)(y_{12}^0)\Delta t \\
&- \left[\left(\mathfrak{p}^A\right)^{n+1/2}\left(y^e{}_{11}\right)^0+\left(\mathfrak{p}^V\right)^{n+1/2}\left(y^e{}_{12}\right)^0\right]\Delta t \\
&+ \sum_{k=1}^{N-1}\left[(p^A)_M^{\langle n+1/2-k\rangle_N}(y_{11})^k+(p^V)_0^{\langle n+1/2-k\rangle_N}(y_{12})^k\right]\Delta t \\
&- \sum_{k=1}^{N-1}\left[(\mathfrak{p}^A)^{\langle n+1/2-k\rangle_N}(y^e{}_{11})^k+(\mathfrak{p}^V)^{\langle n+1/2-k\rangle_N}(y^e{}_{12})^k\right]\Delta t
\end{aligned} \tag{A.31}$$

and (A.28) as

$$\begin{aligned}
\frac{q_{-1/2}^{n+1/2}+q_{1/2}^{n+1/2}}{2} &= P_A\left(M,\frac{1}{2}(A_{M-1/2}^{n+1/2}+A_{M+1/2}^{n+1/2})\right)(y_{21}^0)\Delta t \\
&+ P_V\left(0,\frac{1}{2}(A_{-1/2}^{n+1/2}+A_{1/2}^{n+1/2})\right)(y_{22}^0)\Delta t \\
&- \left[\left(\mathfrak{p}^A\right)^{n+1/2}\left(y^e{}_{21}\right)^0+\left(\mathfrak{p}^V\right)^{n+1/2}\left(y^e{}_{22}\right)^0\right]\Delta t \\
&+ \sum_{k=1}^{N-1}\left[(p^A)_M^{\langle n+1/2-k\rangle_N}(y_{11})^k+(p^V)_0^{\langle n+1/2-k\rangle_N}(y_{12})^k\right]\Delta t \\
&- \sum_{k=1}^{N-1}\left[(\mathfrak{p}^A)^{\langle n+1/2-k\rangle_N}(y^e{}_{11})^k+(\mathfrak{p}^V)^{\langle n+1/2-k\rangle_N}(y^e{}_{12})^k\right]\Delta t.
\end{aligned} \tag{A.32}$$

These substitutions have reduced the number of unknowns from twelve to eight and a system of 8 equations (A.25a, A.25b, A.25c, A.25d, A.28a, A.28b, A31, A32).

A.5 Matching Over the Structured Tree

From the eight equations, we can write down eight residual equations, each of which is stored in a row of a vector $\boldsymbol{f}(\boldsymbol{x})$ where $\boldsymbol{x}$ is a vector of the unknowns. Explicitly,

$$x_1 = A_M^{n+1},\ x_2 = q_M^{n+1},\ x_3 = A_{M+1/2}^{n+1/2},\ x_4 = q_{M+1/2}^{n+1/2},$$
$$x_5 = A_0^{n+1},\ x_6 = q_0^{n+1},\ x_7 = A_{0+1/2}^{n+1/2},\ x_8 = q_{0+1/2}^{n+1/2}$$

and $\boldsymbol{x} = (x_1, ..., x_8)$.

A.5.1 The Jacobian

The Jacobian for matching the boundary is

$$\begin{pmatrix}
-1 & \cdot & \cdot & -\theta & \cdot & \cdot & \cdot & \cdot \\
\cdot & -1 & \chi_1 & \chi_2 & \cdot & \cdot & \cdot & \cdot \\
\chi_3 & -1 & \cdot & \cdot & \chi_4 & \cdot & \cdot & \cdot \\
\cdot & \cdot & \cdot & \cdot & -1 & \cdot & \cdot & -\theta \\
\cdot & \cdot & \cdot & \cdot & \cdot & -1 & \chi_5 & \chi_6 \\
\chi_7 & \cdot & \cdot & \cdot & \chi_8 & -1 & \cdot & \cdot \\
\cdot & \cdot & \chi_9 & -\frac{1}{2} & \cdot & \cdot & \chi_{10} & \cdot \\
\cdot & \cdot & \chi_{11} & \cdot & \cdot & \cdot & \chi_{12} & -\frac{1}{2}
\end{pmatrix}$$

where $\theta = \Delta x/\Delta t$ and $\gamma = \Delta t/2$. As with J for junctions, the element in the i-th row and j-th column, $J(i,j) = \partial f_i/\partial x_j$, and hence the functions χ are placeholders for these derivatives.

A.6 Pressure-Based Venous-Outlet Boundary Condition

At the outlet of the system A, p, φ, and þ are known, but flow q is unknown and will be determined from the boundary condition for A. Similarly to the determination of q at the inlet, we must evaluate $A^{n+1/2}_{M+1/2}$ by using a ghost point a half spatial step after the outlet boundary (see Fig. 3.2). Then,

$$A^{n+1/2}_{M} = \frac{1}{2}\left(A^{n+1/2}_{M-1/2} + A^{n+1/2}_{M+1/2}\right) \iff A^{n+1/2}_{M\pm1/2} = 2A^{n+1/2}_{M} - A^{n+1/2}_{M\mp1/2}. \tag{A.33}$$

And, from (3.13)

$$q^{n+1}_{M} = q^{n}_{M} - \frac{\Delta x}{\Delta t}\left((W_2)^{n+1/2}_{M} + (W_2)^{n-1/2}_{M}\right) + \frac{\Delta t}{2}\left((S_2)^{n+1/2}_{M} + (S_2)^{n-1/2}_{M}\right) \tag{A.34}$$

where W_2, S_2 are given by (3.5b, 3.5c), respectively. Also using (3.13), (3.5a) we can write

$$A^{n+1}_{M} = A^{n}_{M} - \frac{\Delta x}{\Delta t}\left((W_1)^{n+1/2}_{M} + (W_1)^{n-1/2}_{M}\right) + \frac{\Delta t}{2}\left((S_1)^{n+1/2}_{M} + (S_1)^{n-1/2}_{M}\right) \tag{A.35}$$

$$= A^{n}_{M} - \frac{\Delta x}{\Delta t}\left(q^{n+1/2}_{M} + q^{n-1/2}_{M}\right) \tag{A.36}$$

$$\Rightarrow q^{n+1/2}_{M} = \frac{\Delta x}{\Delta t}(A^{n}_{M} - A^{n+1}_{M}) - q^{n-1/2}_{M}, \tag{A.37}$$

since $(W_1)^{n}_{m} = q^{n}_{m}$, $(S_1)^{n}_{m} = 0$ from (3.5b, 3.5c). Equations (A.33, A.34, A.37) give a system of three equations with three unknowns $A^{n+1/2}_{M+1/2}$, $q^{n+1/2}_{M+1/2}$, and q^{n+1}_{M}.

Appendix B

Grand Admittance Algorithms

Algorithm 3: Function Series

Result: Admittance of vessels in series $Y(i,j)$

Input: Admittances of vessels to join in series $Y^S(i,j)$, $Y^T(i,j)$

$D^k = Y^k_{11}Y^k_{22} - Y^k_{12}Y^k_{21}$, $k = S,T$

$Y_{11} = (D^S + Y^S_{11}Y^T_{11})/(Y^S_{22} + Y^T_{11})$

$Y_{12} = (-Y^S_{12}Y^T_{12})/(Y^S_{22} + Y^T_{11})$

$Y_{21} = (-Y^S_{21}Y^T_{21})/(Y^S_{22} + Y^T_{11})$

$Y_{22} = (D^T + Y^S_{22}Y^T_{22})/(Y^S_{22} + Y^T_{11})$

If a spatially homogenous external pressure is applied to a structured tree, create two separate instances of `admit` with the fluid pressure `series` function and the external pressure series function `ExtSeries`. This allows us to compute Y, Y^e in (2.59) separately. If the structured tree external pressure is homogenous, then $Y^e = Y$, and we need only a single instance of `admit`.

Algorithm 4: Function ExtSeries

Result: Admittance of vessels in series $Y(i,j)$ in the case of inhomogeneous external pressure

Input: Admittances of vessels to join in series $Y^S(i,j)$, $Y^T(i,j)$

$D^k = Y^k_{11}Y^k_{22} - Y^k_{12}Y^k_{21}$, $k = S,T$

$Y_{11} = (D^S + Y^S_{11}Y^T_{11})/(Y^S_{22} + Y^T_{11})$; $Y_{12} = (-Y^S_{12}Y^T_{12})/(Y^S_{22} + Y^T_{11})$

$Y_{21} = (-Y^S_{21}Y^T_{21})/(Y^S_{22} + Y^T_{11})$; $Y_{22} = (D^T + Y^S_{22}Y^T_{22})/(Y^S_{22} + Y^T_{11})$

Algorithm 5: Recursive Function `admit(i, j)`

Result: Grand Admittance $Y(i,j)$.

Input: Integers indices i,j

if ($r(i+1,j) < r_{min}$)

  for ($k = A,V$)

    $Y^k(i+1,j) = (2.47)\ \omega \neq 0$; $Y^k(i+1,j) = (2.51)\ \omega = 0$

  $Y(i+1,j) = \texttt{series}(Y^A(i+1,j), Y^V(i+1,j))$

else

  $Y(i+1,j) = \texttt{admit}(i+1,j)$

if ($r(i,j+1) < r_{min}$)

  for ($k = A,V$)

    $Y^k(i,j+1) = (2.47)\ \omega \neq 0$; $Y^k(i,j+1) = (2.51)\ \omega = 0$

  $Y(i,j+1) = \texttt{series}(Y^A(i,j+1), Y^V(i,j+1))$

else

  $Y(i,j+1) = \texttt{admit}(i,j+1)$

$Y_{mid}(i,j) = Y(i+1,j) + Y(i,j+1)$

for ($k = A,V$)

  $Y^k(i,j) =(2.47)\ \omega \neq 0$; $Y^k(i,j) =(2.51)\ \omega = 0$

$Y(i,j) = \texttt{series}(\texttt{series}(Y^V(i,j), Y_{mid}(i,j)), Y^A(i,j))$

Appendix C

Summary Tables for Large Coronary Vessel Networks

This appendix contains the summary tables for the coronary trees used in Chapter 5. In each table, every vessel has an unique ID number. These are used to indicate vessel branching. Vessels also all have a length, and proximal and distal radii in mm. Some vessels have entries have in the D1, D2, D3, and V columns. These are the first, second, and third daughter vessels of a parent, and the index of the vein. Values for all of D1 – D3 indicates a trifurcation, values for D1 & D2 indicate a bifurcation and a value for D1 alone is a monofurcation. The V column indicates the vein to which an artery is joined. Rows with no D or V values has no daughters and is not joined to a vein – these are all terminal veins joined to arteries.

C.1 Left Sided Trifurcating Tree 850μm Mean Truncation Radius

Vessel	Length (mm)	Proximal radius (mm)	Distal radius (mm)	D1	D2	D3	V
0	0.83143	0.18476	0.13857	1	2	3	
1	3.6422	0.15321	0.15321	4		5	
2	4.4741	0.13684	0.10263				6
3	8.0876	0.13684	0.10263				7
4	0.76607	0.15321	0.11491				8
5	0.78886	0.15321	0.11491				9
6	1.4113	0.10263	0.10263				
7	1.403	0.10263	0.10263				
8	0.96955	0.11491	0.11491				
9	1.3814	0.11491	0.11491				

A taper adjustment was made to vessel 5 by changing the distal radius from 0.9 to 0.115 mm.

C.2 Left Sided Bifurcating Tree 850μm Mean Truncation Radius

Vessel	Length (mm)	Proximal radius (mm)	Distal radius (mm)	D1	D2	D3	V
0	0.83143	0.18476	0.13857	1		2	
1	0.75264	0.13684	0.10263	3		4	
2	8.0876	0.13684	0.10263				7
3	3.6181	0.15321	0.15321	5		6	
4	4.4549	0.088206	0.088206				8
5	0.76607	0.15321	0.11491				9
6	0.78886	0.15321	0.11491				10
7	1.403	0.10263	0.10263				
8	1.4113	0.088206	0.088206				
9	0.96955	0.11491	0.11491				
10	1.3814	0.11491	0.11491				

C.3 Left Sided Segmented With Tree 850µm Mean Truncation Radius

Vessel	Length (mm)	Proximal radius (mm)	Distal radius (mm)	D1	D2	D3	V
0	0.83143	0.18476	0.13857	1	2	3	
1	0.75264	0.13684	0.10889	4			
2	1.9612	0.13684	0.10263	5			
3	3.4366	0.13684	0.10263	6			
4	3.1737	0.15321	0.15321	7		8	
5	2.5129	0.088206	0.088206				12
6	1.9243	0.081408	0.07897	9			
7	0.76607	0.15321	0.11491				13
8	0.78886	0.15321	0.11491				14
9	1.2401	0.095432	0.095432	10			
10	1.0579	0.095432	0.090549	11			
11	0.75027	0.090549	0.087688				15
12	1.4113	0.088206	0.088206				
13	0.96955	0.11491	0.11491				
14	1.3814	0.11491	0.11491				
15	1.403	0.087688	0.087688				

C.4 Left Sided Trifurcating Tree 800μm Mean Truncation Radius

Vessel	Length (mm)	Proximal radius (mm)	Distal radius (mm)	D1	D2	D3	V	
0	0.8314	0.1848	0.1386	1	2	3		
1	0.7526	0.1368	0.1089	4	5			
2	4.4741	0.1368	0.1026					8
3	8.7244	0.1368	0.1026					9
4	3.5721	0.1089	0.0817					10
5	3.1737	0.1532	0.1532	6	7			
6	0.7661	0.1532	0.1149					11
7	2.1356	0.1532	0.1149					12
8	1.4113	0.1026	0.1026					
9	1.1312	0.1026	0.1026					
10	1.2455	0.0817	0.0817					
11	0.9696	0.1149	0.1149					
12	1.2106	0.1149	0.1149					

C.5 Left Sided Trifurcating Tree 750μm Mean Truncation Radius

Vessel	Length (mm)	Proximal radius (mm)	Distal radius (mm)	D1	D2	D3	V
0	0.83143	0.18476	0.13857	1	2	3	
1	0.75264	0.13684	0.10889	4	0	5	
2	4.4741	0.13684	0.10263				10
3	8.7244	0.13684	0.10263				11
4	3.5721	0.10889	0.081664				12
5	3.1737	0.15321	0.15321	6	7		
6	0.76607	0.15321	0.11491				13
7	0.78886	0.15321	0.11491	8	9		
8	0.79474	0.10316	0.10316				14
9	1.5045	0.086339	0.075661				15
10	1.4113	0.10263	0.10263				
11	1.1312	0.10263	0.10263				
12	1.2455	0.081664	0.081664				
13	0.96955	0.11491	0.11491				
14	1.6505	0.10316	0.10316				
15	1.2106	0.075661	0.075661				

C.6 Left Sided Trifurcating Tree 700μm Mean Truncation Radius

Vessel	Length (mm)	Proximal radius (mm)	Distal radius (mm)	D1	D2	D3	V
0	0.83143	0.18476	0.13857	1	2	3	
1	0.75264	0.13684	0.10889	4		5	
2	4.4741	0.13684	0.10263				10
3	8.7244	0.13684	0.10263				11
4	3.5721	0.10889	0.081664				12
5	3.1737	0.15321	0.15321	6		7	
6	1.8187	0.15321	0.11491				13
7	0.78886	0.15321	0.11491	8		9	
8	0.79474	0.10316	0.10316				14
9	1.5045	0.086339	0.075661				15
10	1.4113	0.10263	0.10263				
11	1.1312	0.10263	0.10263				
12	1.2455	0.081664	0.081664				
13	1.1253	0.11491	0.11491				
14	1.6505	0.10316	0.10316				
15	1.2106	0.075661	0.075661				

C.7 Left Sided Trifurcating Tree 650μm Mean Truncation Radius

Vessel	Length (mm)	Proximal radius (mm)	Distal radius (mm)	D1	D2	V
0	0.83143	0.18476	0.13857	1	2	3
1	0.75264	0.13684	0.10889	4	5	
2	5.4794	0.13684	0.10263			10
3	8.7244	0.13684	0.10263			11
4	3.5721	0.10889	0.081664			12
5	3.1737	0.15321	0.15321	6	7	
6	1.341	0.15321	0.11491			13
7	0.78886	0.15321	0.11491	8	9	
8	0.79474	0.10316	0.10316			14
9	1.5045	0.086339	0.075661			15
10	0.87373	0.10263	0.10263			
11	1.1312	0.10263	0.10263			
12	1.2455	0.081664	0.081664			
13	1.1321	0.11491	0.11491			
14	1.6505	0.10316	0.10316			
15	1.2106	0.075661	0.075661			

C.8 Full Summary Table

Vessel	Length (mm)	Proximal radius (mm)	Distal radius (mm)	D1	D2	V
0	0.8314	0.1848	0.1386	1	2	
1	0.7526	0.1386	0.1026	3	4	
2	8.7244	0.1386	0.1026			31
3	0.7778	0.1089	0.1089	5	6	
4	4.4549	0.0882	0.0882			36
5	3.5721	0.1089	0.0817			35
6	3.1737	0.1532	0.1532	7	8	
7	0.7661	0.1532	0.1149			33
8	2.1356	0.1532	0.1149			34
9	0.8314	0.1848	0.1386	10	11	
10	0.7526	0.1386	0.1026	12	13	
11	8.7244	0.1386	0.1026			24
12	0.7778	0.1089	0.1089	14	15	
13	4.4549	0.0882	0.0882			23
14	3.5721	0.1089	0.0817			28
15	3.1737	0.1532	0.1532	16	17	
16	0.7661	0.1532	0.1149			32
17	2.1356	0.1532	0.1149			27

Vessel	Length (mm)	Proximal radius (mm)	Distal radius (mm)	D1	D2	V
18	1.44	0.41	0.37	19	20	
19	1.44	0.37	0.32	21	22	
20	2.58	0.09	0.09	23	24	
21	1.44	0.32	0.27	25	26	
22	2.58	0.09	0.09	27	28	
23	1.02	0.0882	0.0882			
24	1.02	0.1026	0.1026			
25	1.44	0.27	0.23	29	30	
26	2.58	0.09	0.09	31	32	
27	1.02	0.1149	0.1149			
28	1.02	0.0817	0.0817			
29	1.44	0.23	0.18	33	34	
30	2.58	0.09	0.09	35	36	
31	1.02	0.1026	0.1026			
32	1.02	0.1149	0.1149			
33	1.02	0.1149	0.1149			
34	1.02	0.1149	0.1149			
35	1.02	0.0817	0.0817			
36	1.02	0.0882	0.0882			

References

[1] B. K. Lee et al. Microcirculatory dysfunction in cardiac syndrome x. *Microcirculation*, 15:451 – 459, 2008.

[2] M. U. Qureshi et al. Numerical simulation of blood flow and pressure drop in the pulmonary arterial and venous circulation. *Biomech. Model Mechanobiol.*, 13(5):1137–1154, 2014.

[3] M. U. Qureshi. *Simulating the pulse wave in the human pulmonary circulation.* PhD thesis, School of Mathematics & Statistics, University of Glasgow, 2013.

[4] G. S. Kassab et al. Morphometry of pig coronary arterial trees. *Am. J. Physiol.*, 265(1 Pt 2):H350–H365, 1993.

[5] G. S. Kassab and Y.-C. B. Fung. Topology and dimensions of pig coronary capillary network. *Am. J. Physiol.*, 267(1 Pt 2):H319–H315, 1994.

[6] J. P. Mynard, D. J. Penny, and J. J. Smolich. Scalability and in vivo validation of a multiscale numerical model of the left coronary circulation. *Am. J. Physiol. Heart Circ.*, 306(4):H517–H528, 2014.

[7] G. S. Kassab, D. H. Lin, and Y.-C. B. Fung. Morphometry of pig coronary venous system. *Am. J. Physiol.*, 267(6 Pt 2):H2100–H2113, 1994.

[8] G. S. Kassab and S. Molloi. Cross-sectional area and volume compliance of porcine left coronary arteries. *Am. J. Physiol. Heart. Circ. Physiol.*, 281:H623–H628, 2001.

[9] S. J. Lai-Fook and J. R. Rodarte. Pleural pressure distribution and its relationship to lung volume and interstitial pressure. *J. Appl. Physiol.*, 70(3):967–978, 1991.

[10] H. Kaneda, T. Nakano, and T. Murakawa. Measurement of intrapleural pressure in patients with spontaneous pneumothorax: a pilot study. *BMC Pulm. Med.*, 19(1):1–6, 2019.

[11] S. J. Mentzer, A. Tsuda, and S. H. Loring. Pleural mechanics and the pathophysiology of air leaks. *J. Thorac. Cardiovasc. Surg.*, 155(5):2182, 2018.

[12] G. S. Kassab. *Coronary Circulation: Anatomy, Mechanical Properties, and Biomechanics*. Springer, 2019.

[13] C. J. Broyd, J. E. Davies, J. E. Escaned, A. Hughes, and K. Parker. Wave intensity analysis and its application to the coronary circulation. *Glob. Cardiol. Sci. Pract.*, 2015(5):64, 2016.

[14] S. Sen et al. Wave intensity analysis in the human coronary circulation in health and disease. *Curr. Cardiol. Rev.*, 10(1):17–23, 2014.

[15] T. Ramanathan and H. Skinner. Coronary blood flow. *Contin. Educ. Anaesth. Crit. Care Pain*, 5(2):61–64, 2005.

[16] M. Calder et al. Computational modelling for decision-making: where, why, what, who and how. *R. Soc. Open Sci.*, 5(6):172096, 2018.

[17] A. Quarteroni, A. Manzoni, and C. Vergara. The cardiovascular system: mathematical modelling, numerical algorithms and clinical applications. *Acta Numer.*, 26:365–590, 2017.

[18] R. B. Chambers. The role of mathematical modeling in medical research: "research without patients?". *Ochsner J.*, 2(4):218 – 223, 2000.

[19] W. Herrington et al. Epidemiology of atherosclerosis and the potential to reduce the global burden of atherothrombotic disease. *Circulation research*, 118(4):535–546, 2016.

[20] S. Barquera et al. Global overview of the epidemiology of atherosclerotic cardiovascular disease. *Archives of medical research*, 46(5):328–338, 2015.

[21] J. R. Ortale, L. C. B. Keiralla, and L. Sacilotto. The posterior ventricular branches of the coronary arteries in the human heart. *Arq. Bras. Cardiol.*, 82(5):468–472, 2004.

[22] E. H. Graf. Just what did archimedes say about buoyancy? *Phys. Teach.*, 42(5):296–299, 2004.

[23] W. W. Nichols and M. F. O'Rourke. The life and times of donald a. mcdonald. *Artery Res.*, 2(1):1 – 8, 2008.

[24] B. E. Carpenter and R. W. Doran. John womersley: Applied mathematician and pioneer of modern computing. *IEEE Ann. Hist. Comput.*, 36(2):60 – 70, 2014.

[25] C. G. Caro, T. J. Pedley, R. C. Schroter, and W. A. Seed, editors. *The Mechanics of the Circulation*. Oxford University Press, Oxford, UK, 1978.

[26] J. R. Womersley. Method for the calculation of velocity, rate of flow andviscous drag in arteries when the pressure gradient is known. *J. Physiol.*, 127:553–563, 1955.

[27] J. R. Womersley. Oscillatory flow in arteries: the constrained elastic tube as a model of arterial flow and pulse transmission. *Phys. Med. Biol.*, 2(2):178–187, 1957.

[28] L. Formaggia, A. Quarteroni, and A. Veneziani. *Cardiovascular Mathematics: Modeling and simulation of the circulatory system*, volume 1. Springer Science & Business Media, 2010.

[29] G. D. A. Vaughan. *Pulse propagation in the pulmonary and systemic arteries*. PhD thesis, School of Mathematics & Statistics, University of Glasgow, 2009.

[30] M. S. Olufsen and J. T. Ottesen. A fluid-dynamical model of the aorta with bifurcations. Technical report, Roskilde Universitet, Roskilde, Denmark, 1995.

[31] L. O. Müller. *Mathematical modelling and simulation of the human circulation with emphasis on the venous system: application to the CCSVI condition*. PhD thesis, Department of Civil, Environmental and Mechanical Engineering, University of Trento, 2014.

[32] P. J. Blanco et al. An anatomically detailed arterial network model for one-dimensional computational hemodynamics. *IEEE. Trans. Biomed. Eng.*, 62(2):736–753, 2015.

[33] R. B. Clipp and B. N. Steele. Impedance boundary conditions for the pulmonary vasculature including the effects of geometry, compliance, and respiration. *IEEE Trans. Biomed. Eng.*, 56(3):862–870, 2008.

[34] J. P. Mynard and P. Nithiarasu. A 1D arterial blood flow model incorporating ventricular pressure, aortic valve and regional coronary flow using the locally conservative galerkin (lcg) method. *Commun. numer. methods eng.*, 24(5):367–417, 2008.

[35] J. H. Spühler, J. Jansson, N. Jansson, and J. Hoffman. 3d fluid-structure interaction simulation of aortic valves using a unified continuum ale fem model. *Front. Physiol.*, 9:363, 2018.

[36] J. Janela, A. Moura, and A. Sequeira. A 3d non-newtonian fluid–structure interaction model for blood flow in arteries. *J. Comput. Appl. Math.*, 234(9):2783–2791, 2010.

[37] L. M. Ellwein et al. Optical coherence tomography for patient-specific 3d artery reconstruction and evaluation of wall shear stress in a left circumflex coronary artery. *Cardiovasc. Eng. Tech.*, 2(3):212–227, 2011.

[38] M.-C. Hsu et al. Dynamic and fluid–structure interaction simulations of bioprosthetic heart valves using parametric design with t-splines and fung-type material models. *Comput. Mech.*, 55(6):1211–1225, 2015.

[39] K. Takizawa et al. Space–time fluid mechanics computation of heart valve models. *Comput. Mech.*, 54(4):973–986, 2014.

[40] W. Chen. *A coupled left ventricle and systemic arteries model.* PhD thesis, University of Glasgow, 2015.

[41] N. Westerhof, F. Bosman, C. J. De Vries, and Abraham A. Noordergraaf. Analog studies of the human systemic arterial tree. *J. Biomech.*, 2(2):121–143, 1969.

[42] B. W. Schaaf and P. H. Abbrecht. Digital computer simulation of human systemic arterial pulse wave transmission: a nonlinear model. *J. Biomech.*, 5(4):345–364, 1972.

[43] M. S. Olufsen. Structured tree outflow condition for blood flow in larger systemic arteries. *Am. J. Physiol. Heart. Circ. Physiol.*, 276:257–268, 1999.

[44] M. S. Olufsen. *Modeling the arterial system with reference to an anesthesia simulator.* PhD thesis, Department of Mathematics, Roskilde University and Department of Anaesthesiology, Herlev University Hospital, 1998.

[45] M. S. Olufsen et al. Rarefaction and blood pressure in systemic and pulmonary arteries. *J. Fluid Mech.*, 705:280–305, 2012.

[46] R. B. Clipp and B. N. Steele. An evaluation of dynamic outlet boundary conditions in a 1d fluid dynamics model. *Math. Biosci. Eng.*, 9(1):61–74, 2012.

[47] R. B. Clipp. *Computational Models of the Pulmonary Vasculature Including the Dynamic Effects of Respiration.* PhD thesis, Biomedical Engineering, North Carolina State University, 2014.

[48] Z. Duanmu et al. A patient-specific lumped-parameter model of coronary circulation. *Sci. Rep.*, 8(1):1–10, 2018.

[49] Z. Duanmu et al. A one-dimensional hemodynamic model of the coronary arterial tree. *Front. Physiol.*, 10:853, 2019.

[50] G. A. Holzapfel, T. C. Gasser, and R. W. Ogden. A new constitutive framework for arterial wall mechanics and a comparative study of material models. *J. Elast.*, 61(1):1 – 48, Jul 2000.

[51] W. D. Tucker, Y. Arora, and K. Mahajan. Anatomy, blood vessels. *StatPearls[Internet]*, 2021.

[52] M. Szopos et al. Computational modeling of blood flow in the aorta—insights into eccentric dilatation of the ascending aorta after surgery for coarctation. *J. Thorac. Cardiovasc. Surg.*, 148(4):1572–1582, 2014.

[53] Z. Hashemi. Chapter 22 - the lattice boltzmann modeling: Solving complex flows including biological cells. In M. Cerrolaza, S. J. Shefelbine, and D. Garzón-Alvarado, editors, *Numerical Methods and Advanced Simulation in Biomechanics and Biological Processes*, pages 391–414. Academic Press, 2018.

[54] M. S. Litwin and K. Chapman. Physical factors affecting human blood viscosity. *J. Surg. Res.*, 10(9):433 – 436, 1970.

[55] G. Chen et al. Regulation of blood viscosity in disease prevention and treatment. *Sci. Bull.*, 57(16):1946–1952, 2012.

[56] H. Naghedi-Baghdar et al. Effect of diet on blood viscosity in healthy humans: a systematic review. *Electron. Physician*, 10(3):6563, 2018.

[57] K. S. Sakariassen, L. Orning, and V. T. Turitto. The impact of blood shear rate on arterial thrombus formation. *Future Sci. OA*, 1(4), 2015.

[58] S.M. Daly. 9 - biophotonics for blood analysis. In Igor Meglinski, editor, *Biophotonics for Medical Applications*, Woodhead Publishing Series in Biomaterials, pages 243 – 299. Woodhead Publishing, 2015.

[59] M. U. Qureshi and N. A. Hill. A computational study of pressure wave reflections in the pulmonary arteries. *J. Math. Biol.*, 71(6–7):1525–49, 2015.

[60] R. Fåhræus and T. Lindqvist. The viscosity the blood in narrow capillary tubes. *Am. J. Physiol.*, 96(3):562–568, 1931.

[61] P. Martini. Die stromung des blutes in eigen gefassen. eine abweichung vom poiseuille'schne gesetz. *Dtsch. Arch. Klin. Med.*, 169:212–222, 1930.

[62] A. R. Pries et al. Resistance to blood flow in microvessels in vivo. *Circ. Res.*, 75(5):904–915, 1994.

[63] A. R. Pries, T. W. Secomb, P. Gaehtgens, and J. F. Gross. Blood flow in microvascular networks. experiments and simulation. *Circ. Res.*, 67(4):826–834, 1990.

[64] T. W. Secomb and A. R. Pries. Blood viscosity in microvessels: experiment and theory. *Comptes Rendus Physique*, 14(6):470–478, 2013.

[65] Y. Huo and G. S. Kassab. The scaling of blood flow resistance: from a single vessel to the entire distal tree. *Biophys. J.*, 96(2):339–346, 2009.

[66] J. S. Bell et al. Microstructure and mechanics of human resistance arteries. *Am. J. Physiol. Heart Circ.*, 311(6):H1560–H1568, 2016.

[67] M. S. Olufsen et al. Numerical simulation and experimental validation of blood flow in arteries with structured tree outflow conditions. *J. Am. Coll. Cardiol.*, 28:1281–1299, 2000.

[68] A. Barnard et al. A theory of fluid flow in compliant tubes. *J Biophys*, 6:717–724, 1966.

[69] C. S. Peskin. *Partial differential equations in biology.* Courant Institute of Mathematical Sciences, New York University, New York, NY, first edition, 1976.

[70] M. U. Qureshi et al. Hemodynamic assessment of pulmonary hypertension in mice: a model based analysis of the disease mechanism. *arXiv e-prints*, page arXiv:1712.01699, Dec 2017.

[71] E. M. Pedersen, H.-W. Sung, A. C. Burlson, and A. P. Yoganathan. Two-dimensional velocity measurements in a pulsatile flow model of the normal abdominal aorta simulating different hemodynamic conditions. *J. Biomech.*, 26(10):1237–1247, 1993.

[72] S. E. Maier, D. Meier, P. Boesiger, U. T. Moser, and A. Vieli. Human abdominal aorta: comparative measurements of blood flow with mr imaging and multigated doppler us. *Radiology*, 171(2):487–492, 1989.

[73] Z. Zhong et al. Noninvasive measurements and analysis of blood velocity profiles in human retinal vessels. *Investig. Ophthalmol. Vis. Sci.*, 52(7):4151–4157, 2011.

[74] G. J. Tangelder et al. Velocity profiles of blood platelets and red blood cells flowing in arterioles of the rabbit mesentery. *Circ. Res.*, 59(5):505–514, 1986.

[75] J. Lighthill. *Mathematical Biofluiddynamics*. Society For Industrial and Applied Mathematics, Philadelphia, PA, third edition, 1987.

[76] J. Alastruey et al. Pulse wave propagation in a model human arterial network: Assessment of 1–D visco–elastic simulations against in vitro measurements. *J. Biomech.*, 44:2250–2258, 2011.

[77] S. J. Sherwin et al. One-dimensional modelling of a vascular network in space-time variables. *J. Eng. Math.*, 47(3):217–250, 2003.

[78] K. S. Matthys et al. Pulse wave propagation in a model human arterial network: assessment of 1-d numerical simulations against in vitro measurements. *J. Biomech.*, 40(15):3476–3486, 2007.

[79] W. Cousins and P. A. Gremaud. Boundary conditions for hemodynamics: The structured tree revisited. *J Comput Phys*, 231:6086–6096, 2012.

[80] T. J. Pedley. *The Fluid mechanics of large blood vessels*. Cambridge University Press, 1980.

[81] D. Elad, R. D. Kamm, and A. H. Shapiro. Tube law for the intrapulmonary airway. *Am. J. Physiol.*, 65(1):7–13, 1988.

[82] A. Juel and A. Heap. The reopening of a collapsed fluid-filled elastic tube. *J. Fluid Mech.*, 572:287–310, 2007.

[83] R. J. Whittaker et al. A rational derivation of a tube law from shell theory. *Q. J. Mech. Appl. Math.*, 63(4):465–496, 2010.

[84] M. J. Colebank, M. U. Qureshi, and M. S. Olufsen. Sensitivity analysis and uncertainty quantification of 1D models of the pulmonary circulation. *arXiv e-prints*, page arXiv:1807.02863, Jul 2018.

[85] M. J. Lighthill. *Mathematical Biofluiddynamics*. Society for Industrial and Applied Mathematics, first edition, 1975.

[86] Massimiliano Mercuri. *Tuning of boundary conditions parameters for hemodynamics simulation using patient data*. PhD thesis, University of Sheffield, 2019.

[87] Reference Values for Arterial Stiffness' Collaboration. Determinants of pulse wave velocity in healthy people and in the presence of cardiovascular risk factors:'establishing normal and reference values'. *Eur. Heart J.*, 31(19):2338–2350, 2010.

[88] G. Dattoli and A. Torre. *Theory and applications of generalized Bessel functions*. Aracne Rome, 1996.

[89] P. Libby and P. Theroux. Pathophysiology of coronary artery disease. *Circulation*, 111(25):3481–3488, 2005.

[90] L. A. Latson and L. R. Prieto. Congenital and acquired pulmonary vein stenosis. *Circulation*, 115(1):103–108, 2007.

[91] P. Kosar, E. Ergun, C. Öztürk, and U. Kosar. Anatomic variations and anomalies of the coronary arteries: 64-slice ct angiographic appearance. *Diagn. Interv. Radiol.*, 15(4):275, 2009.

[92] R. Choudhary, A. Batra, V. Malik, and K. Mahajan. All four coronary arteries arising separately from the right aortic sinus of valsalva: rare anomaly. *BMJ Case Rep.*, 12(4), 2019.

[93] Z. Duanmu et al. A patient-specific lumped-parameter model of coronary circulation. *Sci. Rep.*, 8(1):1–10, 2018.

[94] S. Choi et al. 1d network simulations for evaluating regional flow and pressure distributions in healthy and asthmatic human lungs. *J. Appl. Physiol.*, 127(1):122–133, 2019.

[95] C. D. Murray. The physiological principle of minimum work applied to the angle of branching of arteries. *J. Gen. Physiol.*, 9(6):835–841, 1926.

[96] H. B. M. Uylings. Optimization of diameters and bifurcation angles in lung and vascular tree structures. *Bull. Math. Biol.*, 39(5):509–520, 1977.

[97] M. Zamir. Nonsymmetrical bifurcations in arterial branching. *J. Gen. Physiol.*, 72(6):837–845, 1978.

[98] A. C. Cameron, N. N. Lang, and R. M. Touyz. *Chapter 10 - Cardiovascular Complications from Cancer Therapy: Hypertension–Focus on Vascular Endothelial Growth Factor Inhibitors*, pages 185–211. Elsevier, 2016.

[99] D. Kerkhove, I. Paciolla, and G. Arpino. Chapter 3 – classification by mechanisms of cardiotoxicity. In P. Lancellotti, J. L. Zamorano Gómez, and M. Galderisi, editors, *Anti-Cancer Treatments and Cardiotoxicity*, pages 13–34. Academic Press, Boston, 2017.

[100] K.A. Lee and C. M. Nelson. New insights into the regulation of epithelial–mesenchymal transition and tissue fibrosis. *Int. Rev. Cell Mol. Biol.*, 294:171–221, 2012.

[101] Y.-C. B. Fung, editor. *Biomechanics: Circulation.* Springer, second edition, 2010.

[102] S. Singhal, R. Henderson, K. Horsfield, K. Harding, and G. Cumming. Morphometry of the human pulmonary arterial tree. *Circ. Res.*, 33(2):190–197, 1973.

[103] W. Huang, R. T. Yen, M. McLaurine, and G. Bledsoe. Morphometry of the human pulmonary vasculature. *J. Appl. Physiol.*, 81(5):2123–2133, 1996.

[104] R. Avram et al. Real-world heart rate norms in the health eheart study. *NPJ Digit. Med.*, 2(1):1–10, 2019.

[105] A. M. Zahid et al. Quantification of arterial, venous, and cerebrospinal fluid flow dynamics by magnetic resonance imaging under simulated micro-gravity conditions: a prospective cohort study. *Fluids and Barriers of the CNS*, 18(1):1–9, 2021.

[106] M. Zielinska-Krawczyk, R. Krenke, E. M. Grabczak, and Richard W R. W. Light. Pleural manometry–historical background, rationale for use and methods of measurement. *Respir. Med.*, 136:21–28, 2018.

[107] K. Hu, A. Chopra, J. T. Huggins, and R. Nanchal. Pleural manometry: Techniques, applications, and pitfalls. *J. Thorac. Dis.*, 12(5):2759, 2020.

[108] S. A. Sahn and J. E. Heffner. Spontaneous pneumothorax. *N. Engl. J. Med.*, 342(12):868–874, 2000.

[109] W.-I. Choi. Pneumothorax. *Tuberc. Respir. Dis.*, 76(3):99–104, 2014.

[110] K. E. Barrett, S. Boitano, S. M. Barman, and H. L. Brooks. *Ganong's review of medical physiology twenty.* E-Book, 2010.

[111] T. L. Stedman. *Stedman's medical dictionary.* Lippincott Williams & Wilkins, Baltimore, Maryland, USA, 2006.

[112] R. Klabunde. *Cardiovascular physiology concepts.* Lippincott Williams & Wilkins, 2011.

[113] A. L. Goldberger, Z. B. Goldberger, and A. Shvilkin. *Clinical electrocardiography: a simplified approach e-book.* Elsevier Health Sciences, 2017.

[114] K. Toska and M. Eriksen. Respiration-synchronous fluctuations in stroke volume, heart rate and arterial pressure in humans. *J. Physiol.*, 472(1):501–512, 1993.

[115] S. C. Beards and J. Lipman. Decreased cardiac index as an indicator of tension pneumothorax in the ventilated patient. *Anaesthesia*, 49(2):137–141, 1994.

[116] A. N. Hurewitz et al. Cardiovascular and respiratory consequences of tension pneumothorax. *Bull. Eur. Physiopathol. Respir.*, 22(6):545–549, 1986.

[117] A. W. McKibben and S. A. Ravenscraft. Pressure-controlled and volume-cycled mechanical ventilation. *Clin. Chest Med.*, 17(3):395–410, 1996.

[118] A. C. Burton and D. J. Patel. Effect on pulmonary vascular resistance of inflation of the rabbit lungs. *J. Appl. Physiol.*, 12(2):239–246, 1958.

[119] R. A. Walsh, J. C. Fang, and V. Fuster, editors. *Hurst's The Heart: Manual of Cardiology.* McGraw Hill Medical, New York, NY, thirteenth edition, 2013.

[120] J. Lee et al. In silico coronary wave intensity analysis: application of an integrated one-dimensional and poromechanical model of cardiac perfusion. *Biomech. Model. Mechanobiol.*, 15(6):1535–1555, 2016.

[121] J. Lee et al. Multiscale modelling of cardiac perfusion. In *Modeling the heart and the circulatory system*, pages 51–96. Springer, 2015.

[122] A. Goyal et al. Model-based vasculature extraction from optical fluorescence cryomicrotome images. *IEEE Trans. Med. Imag.*, 32(1):56–72, 2012.

[123] P. P. Lelovas et al. A comparative anatomic and physiologic overview of the porcine heart. *J. Am. Assoc. Lab. Anim. Sci.*, 53(5):432–438, 2014.

[124] M. E. Weaver et al. A quantitative study of the anatomy and distribution of coronary arteries in swine in comparison with other animals and man. *Cardiovasc. Res.*, 20(12):907–917, 1986.

[125] J. P. Snyder. The space oblique mercator projection. *Photogramm. Eng. Remote Sens.*, 44(5):585–596, 1978.

[126] A. S. Antonopoulos et al. Chapter 2.1 - functional anatomy. In D. Tousoulis, editor, *Coronary Artery Disease*, pages 121–126. Academic Press, 2018.

[127] B. Kaimovitz, Y. Lanir, and G. S. Kassab. Large-scale 3-d geometric reconstruction of the porcine coronary arterial vasculature based on detailed anatomical data. *Ann. Biomed. Eng.*, 33(11):1517–1535, 2005.

[128] B. Kaimovitz, Y. Lanir, and G. S. Kassab. A full 3-d reconstruction of the entire porcine coronary vasculature. *Am. J. Physiol. Heart Circ.*, 299(4):H1064–H1076, 2010.

[129] Ziad F. Issa, John M. Miller, and Douglas P. Zipes. 27 - epicardial ventricular tachycardia. In Z. F. Issa, J. M. Miller, and D. P. Zipes, editors, *Clinical Arrhythmology and Electrophysiology*, pages 907–924. Elsevier, Philadelphia, third edition, 2019.

[130] M. W. Kassem et al. Cardiac veins, an anatomical review. *Transl. Res. Anat.*, 23:100096, 2021.

[131] A. Habib et al. The anatomy of the coronary sinus venous system for the cardiac electrophysiologist. *Europace*, 11:v15–v21, 2009.

[132] G. J. Schaffler et al. Imaging the coronary venous drainage system using electron-beam ct. *Surg. Radiol. Anat.*, 22(1):35–39, 2000.

[133] S. Y. Ho, D. Sanchez-Quintana, and A. E. Becker. A review of the coronary venous system: A road less travelled. *Heart Rhythm*, 1:107–112, 2004.

[134] Stylianos Kastellanos, Konstantinos Aznaouridis, Charalambos Vlachopoulos, Eleftherios Tsiamis, Evangelos Oikonomou, and Dimitris Tousoulis. Overview of coronary artery variants, aberrations and anomalies. *World J. Cardiol.*, 10(10):127, 2018.

[135] J. S. Shahoud, M. J. Ambalavanan, and V. S. Tivakaran. Cardiac dominance. *StatPearls [Internet]*, 2020.

[136] P. A. Iaizzo. *Handbook of cardiac anatomy, physiology, and devices.* Springer Science & Business Media, 2009.

[137] A. Sirajuddin et al. Coronary venous anatomy and anomalies. *J. Cardiovasc. Comput. Tomogr.*, 14(1):80–86, 2020.

[138] A. J. Pappano and W. G. Wier. 8 - the microcirculation and lymphatics. In A. J. Pappano and W. G. Wier, editors, *Cardiovascular Physiology*, pages 153–170. Elsevier, Philadelphia, tenth edition, 2013.

[139] L. M. van Bortel and J. J. Spek. Influence of aging on arterial compliance. *J. Hum. Hypertens.*, 12(9):583–586, 1998.

[140] S. Farhan et al. Implantation of paclitaxel-eluting stent impairs the vascular compliance of arteries in porcine coronary stenting model. *Atherosclerosis*, 202(1):144–151, 2009.

[141] C. J. van Andel, P. V. Pistecky, and C. Borst. Mechanical properties of porcine and human arteries. *Ann. Thorac. Surg.*, 76:58 – 65, 2003.

[142] S. S. Franklin et al. Blood pressure categories, hypertensive subtypes, and the metabolic syndrome. *J. Hypertens.*, 24(10):2009–2016, 2006.

[143] D. B. Young. Control of cardiac output. *Integrated Systems Physiolo.*, 2(1):1–97, 2010.

[144] T. C. Slesnick, R. Gertler, and W. C. Miller-Hance. Chapter 14 - essentials of cardiology. In C. J. Coté, J. Lerman, and I. D. Todres, editors, *A Practice of Anesthesia for Infants and Children*, pages 293–330. W.B. Saunders, Philadelphia, fourth edition, 2009.

[145] P. H. M. Bovendeerd et al. Dependence of intramyocardial pressure and coronary flow on ventricular loading and contractility: a model study. *Ann. Biomed. Eng.*, 34(12):1833–1845, 2006.

[146] F. W. Heineman and J. Grayson. Transmural distribution of intramyocardial pressure measured by micropipette technique. *Am. J. Physiol. Heart Circ.*, 249(6):H1216–H1223, 1985.

[147] B. A. Borlaug and Y. N. V. Reddy. The role of the pericardium in heart failure: implications for pathophysiology and treatment. *JACC: Heart Failure*, 7(7):574–585, 2019.

[148] D. Ramachandran, C. Luo, T. S. Ma, and J. W. Clark. Using a human cardiovascular-respiratory model to characterize cardiac tamponade and pulsus paradoxus. *Theor. Biol. Med. Model.*, 6(1):15, 2009.

[149] Kim H Parker. An introduction to wave intensity analysis. *Med. Biol. Eng. Comput.*, 47(2):175–188, 2009.

[150] J. P. Mynard et al. Measurement, analysis and interpretation of pressure/flow waves in blood vessels. *Front. Physiol.*, 11:1085, 2020.

[151] A. D. Menno and W. G. Schenk Jr. Dynamics of coronary arterial flow: flow alterations resulting from certain surgical procedures and drugs of surgical importance. *Surgery*, 50:82–90, 1961.

[152] R. E. Mates et al. Fluid dynamics of coronary artery stenosis. *Circ. Res.*, 42(1):152–162, 1978.

[153] R. Pietrabissa et al. A lumped parameter model to evaluate the fluid dynamics of different coronary bypasses. *Med. Eng. Phys.*, 18(6):477–484, 1996.

[154] J. E. Davies et al. Evidence of a dominant backward-propagating "suction" wave responsible for diastolic coronary filling in humans, attenuated in left ventricular hypertrophy. *Circulation*, 113(14):1768–1778, 2006.

[155] C. Thollon and J.-P. Vilaine. If inhibition in cardiovascular diseases. *Adv. Pharmacol.*, 59:53–92, 2010.

[156] S. Mantero, R. Pietrabissa, and R. Fumero. The coronary bed and its role in the cardiovascular system: a review and an introductory single-branch model. *J. Biomed. Eng.*, 14(2):109–116, 1992.

[157] J. Lee et al. *Modeling the Heart and the Circulatory System*, chapter 3: Multiscale modelling of cardiac perfusion, pages 51–96. Springer International Publishing, 2015.

[158] Heng Zeng and Jian-Xiong Chen. Microvascular rarefaction and heart failure with preserved ejection fraction. *Front. Cardiovasc. Med.*, 6:15, 2019.

[159] Y. Huo and G. S. Kassab. A hybrid one-dimensional/womersley model of pulsatile blood flow in the entire coronary arterial tree. *Am. J. Physiol. Heart. Circ. Physiol.*, 292:2623–2633, 2007.

[160] M. A. Heiskanen et al. Different predictors of right and left ventricular metabolism in healthy middle-aged men. *Front. Physiol.*, 6:389, 2015.

[161] A. G. Goodwill, G. M. Dick, A. M. Kiel, and J. D. Tune. Regulation of coronary blood flow. *Compr. Physiol.*, 7(2):321, 2017.

[162] D. K. Molina and V. J. M. DiMaio. Normal organ weights in men: part i—the heart. *Am. J. Forensic Med. Pathol.*, 33(4):362–367, 2012.

[163] N. Townsend et al. *Coronary heart disease statistics 2012*. British Heart Foundation, 2012.

[164] L. M. Paun et al. Assessing model mismatch and model selection in a bayesian uncertainty quantification analysis of a fluid-dynamics model of pulmonary blood circulation. *J. R. Soc. Interface*, 17(173):20200886, 2020.

[165] L. M. Paun and D. Husmeier. Mcmc with gaussian processes for fast parameter estimation and uncertainty quantification in a 1d fluid-dynamics model of the pulmonary circulation. *Int. J. Numer. Methods Biomed. Eng.*, 2020.

[166] L. M. Paun. *Bayesian parameter estimation and uncertainty quantification in fluid-dynamics models of the pulmonary circulation system*. PhD thesis, School of Mathematics and Statistics, University of Glasgow, 2020.

[167] M. Loukas et al. The clinical anatomy of high take-off coronary arteries. *Clin. Anat.*, 29(3):408–419, 2016.

[168] W. W. Chen, H. Gao, X. Y. Luo, and N. A. Hill. Study of cardiovascular function using a coupled left ventricle and systemic circulation model. *J. Biomech.*, 49(12):2445–2454, 2016.

[169] L. Feng et al. Fluid–structure interaction in a fully coupled three-dimensional mitral–atrium–pulmonary model. *Biomech. Model. Mechanobiol.*, pages 1–29, 2021.

[170] J. A. Sirs. The flow of human blood through capillary tubes. *J. Physiol.*, 442(1):569–583, 1991.

[171] S. Rosenkranz and I. R. Preston. Right heart catheterisation: best practice and pitfalls in pulmonary hypertension. *European Respiratory Review*, 24(138):642–652, 2015.